Lake Icepack and Dry Snowpack Thickness Measurement Using Coherent Multipath Interference of Wideband Planck Radiation

by

Seyedmohammad Mousavi

A dissertation submitted in partial fulfillment
of the requirements for the degree of
Doctor of Philosophy
(Electrical Engineering)
in The University of Michigan
2020

Doctoral Committee:

Professor Kamal Sarabandi, Co-Chair
Associate Research Scientist Roger D. De Roo, Co-Chair
Professor Anthony W. England
Associate Professor Mark Flanner
Professor Joel T. Johnson, The Ohio State University
Professor Christopher S. Ruf

Seyedmohammad Mousavi

mousavis@umich.edu

ORCID iD: 0000-0002-8992-516X

To my beloved mother and father

ACKNOWLEDGEMENTS

Firstly, I would like to express my sincere gratitude to my advisers, Professor Kamal Sarabandi and Dr. Roger De Roo, for their encouragement and extreme support throughout my PhD. Their guidance helped me in all the time of my research and writing of this thesis. I would also like to thank the rest of my thesis committee, Professor Anthony England for all the fruitful discussion we had throughout this research work, Professor Joel Johnson and Professor Christopher Ruf for their great comments and questions, and Professor Mark Flanner from the Climate and Space Sciences and Engineering (CLaSP) department for his insightful feedback on this research. I would also like to thank the National Aeronautics and Space Administration (NASA) for funding this project.

I appreciate the Space Physics Research Laboratory (SPRL) staff in the CLaSP department for helping us in design and fabrication. I would also like to thank the University of Michigan Biological Station (UMBS) and the Great Lakes Research Center (GLRC) staff at the Michigan Technological University (MTU) for their assistance during the field campaigns in this research work. I also want to thank Dr. Christopher Crawford from the United States Geological Survey (USGS) for his assistance in part of Winter 2018 field campaign in Minnesota and South Dakota. I would also want to thank all the NASA SnowEx team members for their assistance in the 2017 SnowEx campaign (February 06-25, 2017) in the Grand Mesa National Forest.

I would also want to thank all my teachers from my early stages at school till

my undergraduate and graduate years. I want to specially thank Professor Fawwaz Ulaby, Professor Anthony Grbic, and Professor Amir Mortazawi for offering great courses in the area of applied electromagnetics and RF circuits out of which I have learned a lot.

I want to thank all my former and current fellow lab-mates in the Radiation Laboratory for their great friendship and sharing their views during my PhD.

I am also grateful to have many wonderful friends in Ann Arbor and elsewhere in the United States who have always been a major source of support while I have been miles away from my family. Thank you all for always being there for me.

And finally, last but by no means least, my deepest appreciation goes to my beloved parents, Seyed Javad and Fatemeh and my brother Mehdi for their unconditional love, affection, and support. Wherever I am standing today, I definitely owe it to them.

Mohammad Mousavi
January 2020
Ann Arbor, MI

TABLE OF CONTENTS

LIST OF FIGURES

Figure

LIST OF ABBREVIATIONS

ACF autocorrelation function

ASO Airborne Snow Observatory

ATM Advanced Technical Materials

AWGN added white Gaussian noise

BPF band pass filter

CCIN Canadian Cryospheric Information Network

CLaSP Climate and Space Sciences and Engineering

COTS commercial-off-the-shelf

CRLB Cramer-Rao lower bound

ESAS Earth Science and Applications from Space

FAR False Alarm Rate

FMCW Frequency Modulated Continuous Wave

FSLL first side lobe level

GLRC Great Lakes Research Center

GPR ground penetrating radar

IDFT inverse discrete Fourier transform

IF intermediate frequency

IFFT inverse fast Fourier transform

InSAR Interferometric Synthetic Aperture Radar

LNA low noise amplifier

MTU Michigan Technological University

MVU minimum-variance unbiased

NASA National Aeronautics and Space Administration

PD Probability of Detection

PDF probability density function

RBW resolution bandwidth

RFI radio frequency interference

RMSE root mean squared error

RMSTDE root mean square time delay error

SD standard deviation

SFMR stepped-frequency microwave radiometer

SLF side lobe fall-off

SLL side lobe level

SNR signal to noise ratio

SPRL Space Physics Research Laboratory

SWE snow water equivalent

UMBS University of Michigan Biological Station

USGS United States Geological Survey

VBW video bandwidth

VNA vector network analyzer

WGN white Gaussian noise

WiBAR wideband autocorrelation radiometry

ABSTRACT

The seasonal terrestrial snowpack is an important source of water for many parts of the globe. The global quantification of the amount of water in the snowpack reservoir has been a long term objective of most remote sensing applications. Thus far, the primary means of quantifying the amount of snow on the ground has been via the differential scatter-darkening mechanism, such as 19 and 37 GHz brightness difference. This technique is region specific and depends on the statistics of snow grain sizes. While a time series of more than 35 years of passive microwave data has been made, progress in understanding the scatter-darkening brightness signature of snow continues, especially for forested areas where vegetation scattering confounds the signature.

In addition, monitoring the ice thickness is important in analyzing the pressure exerted to off-shore structures such as wind farms. It is also an essential parameter for the safety of ice fishing and ice skating activities. The current and traditional method of ice thickness measurement is by drilling holes through the ice, which is not only cumbersome but also dangerous. Hence, an accurate remote sensing technique is needed to safely and non-destructively measure the ice and snow thickness.

In this work, a novel microwave radiometric technique, wideband autocorrelation radiometry (WiBAR), is introduced. The radiometer offers a direct method to remotely measure the microwave propagation time difference of multipath microwave emission from low-loss layered surfaces, such as a dry snowpack and a freshwater lake icepack. The microwave propagation time difference through the pack yields a mea-

sure of its vertical extent; thus, this technique provides a direct measurement of depth. It is also a low-power sensing method since there is no transmitter. A simple geophysical forward model for the multipath interference phenomenon is presented, and the system requirements needed to design a WiBAR instrument are derived. Three different versions of WiBAR instruments operating at L-, S-, and X-band are fabricated from commercial-off-the-shelf (COTS) components. To validate the WiBAR method, simulated laboratory measurements are first performed using a microwave scene simulator circuit. Finally, to prove the potential of this technique as an inversion algorithm, many field measurements were conducted in different winter seasons in the Upper Midwest region, Michigan and Minnesota. It is demonstrated that a WiBAR instrument operating in the frequency range of 7-10 GHz (X-band) can directly measure the icepack thicknesses from nadir to 59 degree of incidence angles. The WiBAR was able to measure the lake icepack thicknesses in the range of 22-59 cm with an accuracy of about 2 cm over this range of incidence angles.

CHAPTER I

Introduction

Snow cover plays a vital role in providing the water supplies for domestic, industrial, and agricultural purposes. The extent and duration of snow cover are important factors for studying the global climate [21, 46]. Study of snowpacks is also important in water resource management as well as flood and avalanche events [65, 77, 92]. Another important remote sensing problem is determination of ice layer thickness over open bodies of water. The knowledge of the ice thickness is important in analyzing the pressure exerted to off-shore structures such as wind farms [47]. Ability to map ice layer thickness can be utilized for the safety of ice fishing and ice skating activities. Thus, monitoring snow and ice are two of the most important remote sensing objectives.

With the rapid industrial and human population growth, the demand for accurate remote sensing instruments and techniques for monitoring the environmental changes and management of natural sources is increasing. Environmental changes such as global warming have been imposing rapid changes upon the cryosphere [79]; as a result, the statistics which describe the extent, timing, and snow water equivalent (SWE) of seasonal snowpacks on prairie and alpine terrains are no longer stationary [53]. Effective management of freshwater reservoir in glaciers and mountainous regions requires almost daily monitoring of the spatial and temporal distribution of SWE and

snowpack wetness. Such tasks are appropriate for satellite sensors or sensors on long duration solar powered autonomous airborne vehicles, but the current remote sensors and technologies are not adequate to retrieve the required snow and ice parameters with desired accuracy. Hence, in any forward and inverse model, the icepack and snowpack growth, metamorphism, and melting must be first understood. Then, their microwave proprieties affected by wetness, and finally the effect of terrain, such as slope and vegetation coverage, must be studied.

Due to their all-weather operation capability, both microwave radar and radiometer systems have long been proposed and implemented as powerful remote sensing tools in retrieving the physical parameters of interest. For most remote sensing applications, the gross parameters of the target, such as vertical extent of snowpack/icepack and SWE, are often the parameters of interest. Current microwave remote sensing of dry snowpack is based on frequency-dependent differential scattering by the ice grains that comprise snowpacks. In the case of microwave radiometry, this phenomenon referred to as scatter darkening [14, 13, 8, 42, 18, 70, 94, 71, 10, 23, 39, 12, 81, 44]. It was first recognized by England [14, 13] as contributing to the microwave brightness of snowpacks, sea ice, frozen soils, and planetary regolith. This scatter darkening based technique has been developed as a SWE remote sensing technology over the last three decades [8, 27, 42]. At higher frequencies (shorter wavelengths), upwelling microwave radiation experiences greater scattering; thus, the spectral gradient of microwave brightness temperature becomes significantly more negative as the snow on the ground accumulates. For example, differences between microwave brightness temperatures at two different frequencies, namely 19 and 37 GHz, are used in an empirical algorithm by Environment Canada to estimate the SWE of snowpacks on the Canadian Great Plains reported on Canadian Cryospheric Information Network (CCIN) URL (https://www.ccin.ca/home/ccw/snow/current).

The current microwave remote sensing of dry snowpack, scatter darkening based

technique, is region specific and depends on the statistics of snow grain sizes. In addition, the current and traditional method of ice thickness measurement is by drilling holes through the ice, which is not only cumbersome but also dangerous. An alternative approach is to focus on the layer's macroscopic properties and measure the travel time through the layer. Altimeters and ground penetrating radars (GPRs) have been used to measure the snow and ice thickness [19]. However, active techniques are hungry for power, which can make radar space missions expensive. To address this issue, a passive microwave remote sensing technique that measures the travel time is developed in this work. This technique is first introduced in Chapter II, which is known as wideband autocorrelation radiometry (WiBAR).

1.1 Microwave Radiometry

The term radiometry means the incoherent measurement of electromagnetic radiation, and the term microwave describes a form of electromagnetic radiation with frequencies (wavelengths) between 300 MHz (100 cm) and 300 GHz (0.1 cm). As it will be discussed in the next section, all matter at a finite absolute temperature radiates electromagnetic energy at a level that depends on its electrical property and geometrical features. A material may also absorb and/or reflect the energy incident upon it. By measuring the electromagnetic energy radiated by a material, it is possible to infer some of material's properties, such as its temperature and dielectric properties.

1.1.1 Blackbody Radiation

In general, of the radiation incident upon a material, a portion of it is absorbed, while the other portion is scattered. A blackbody is an ideal opaque material that absorbs all the incident radiation at all frequencies and reflects none. Based on the thermodynamic equilibrium theorem, which states that the emission is equal to the

absorption, a blackbody is also a perfect emitter. According to the Planck's radiation law, a blackbody radiates energy in all direction and all frequencies, as given by (1.1) [89].

$$I_f = \frac{2hf^3}{c^2}\left(\frac{1}{\mathrm{e}^{hf/kT}-1}\right) \tag{1.1}$$

where I_f is the spectral specific intensity in $\mathrm{Wm^{-2}sr^{-1}Hz^{-1}}$, $h = 6.63 \times 10^{-34}$ joules.s is the Planck's constant, f is the frequency in Hz, $c = 3 \times 10^8$ m/s is the speed of light in free space, $k = 1.38 \times 10^{-23}$ joule/K is the Boltzmann's constant, and T is the blackbody's absolute temperature in K. In the microwave frequency range where $hf/kT \ll 1$, (1.1) can be approximated by $I_f \approx \frac{2KTf^2}{c^2}$. This low-frequency approximation is known as the Rayleigh-Jeans law [90, 91, 89]. The fractional deviation of this approximation is less than 1% if $f/T < 3.9 \times 10^8$ Hz $\mathrm{K^{-1}}$ [89]. As an example, at a room temperature 300 K, this inequality will hold if $f < 117$ GHz, which covers most of the useful microwave frequencies.

1.1.2 Brightness Temperature

While a blackbody is a perfect absorber/emitter, real material are referred to as grey bodies, which means that they emit less than a blackbody at the same temperature and do not absorb all the incident energy. The brightness temperature, $T_B(\theta, \phi)$, of an object is the temperature of an equivalent blackbody in thermal equilibrium that has the same observed specific intensity as the object. The emissivity, $e(\theta, \phi)$, is the ratio of the specific intensity of the object to that of a blackbody at the same temperature, T. The angular pair (θ, ϕ) is introduced since emission from an object is direction dependent.

$$e(\theta, \phi) = \frac{T_B(\theta, \phi)}{T} \tag{1.2}$$

Since the observed specific intensity of an object is equal or less than that of a blackbody at the same temperature, it is obvious that the emissivity is in the range $0 \leq e(\theta, \phi) \leq 1$; as a result, the brightness temperature of an object is smaller than or equal to its physical temperature.

1.1.3 Statistics of the Brightness Temperature

Spontaneous emission is due to random oscillatory motion of atomic charges inside a material manifested by its physical temperatures. This can be viewed as the collective radiation of many infinitesimal dipole radiators in the material. One approach to analyze the statistics of the brightness temperature is the fluctuation dissipation theorem [75, 76, 88].

Assuming that the fluctuations are uncorrelated between neighboring volume elements, the thermal radiation is generated by an equivalent current source $\overline{J}(\overline{r}, \omega) = -i\omega\overline{P}(\overline{r}, \omega)$, with expected value of zero and correlation as given by

$$\left\langle \overline{J}(\overline{r}, \omega)\overline{J}^{*}(\overline{r'}, \omega') \right\rangle = \frac{4}{\pi}\omega\epsilon''(\overline{r})KT(\overline{r})\overline{\overline{I}}\delta(\omega - \omega')\delta(\overline{r} - \overline{r'}) \tag{1.3}$$

where $\overline{P}$ is the fluctuating electric dipole moment whose time average is zero, $\epsilon''(\overline{r})$ is the imaginary part of the permittivity. It is noted that in (1.3) only positive frequencies are considered. The detailed derivation of (1.3) is explained in Chapter 2 of [88]. Since there are many independent sources of radiation, according to the central limit theorem [67], the thermal radiation of an isotropic and homogeneous medium has a Gaussian distribution.

1.2 Common Earth Materials

In this section, the electrical properties of some common natural materials are discussed. The focus is on the freshwater, lake ice, dry snow, and soil (wet or dry)

since they will be used in the forward modeling of snow/ice layer over a layer of soil or water.

1.2.1 Fresh Water

Out of all water forms on Earth, only 2.5% is freshwater. Out of this freshwater, only 1.2% is surface water, which supports most of life on land, and the rest is locked up in ice and in the ground. Out of this surface freshwater, 20.9% is in lakes. The distribution of Earth's water is shown in Fig. 1.1 [20].

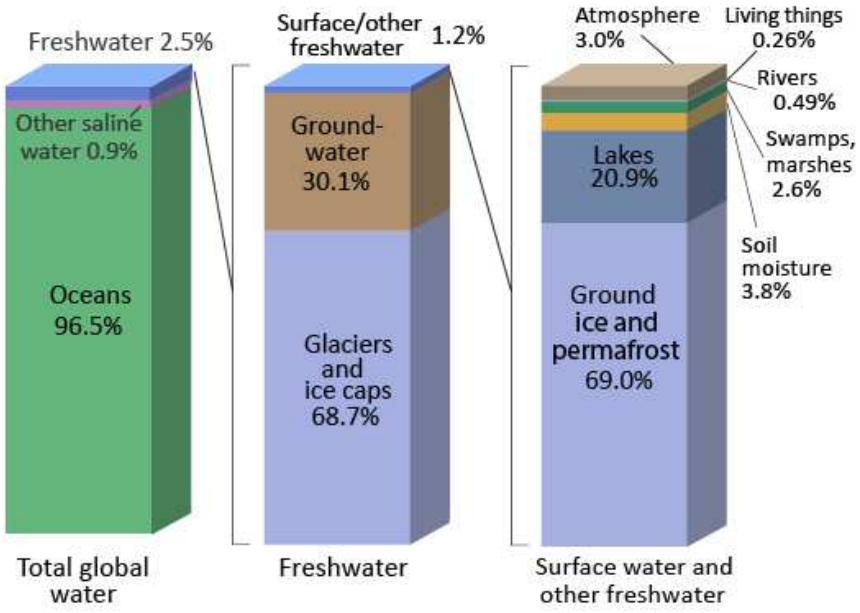

Figure 1.1: Distribution of Earth's water.
Source: Igor Shiklomanov's chapter "World fresh water resources" in Peter H. Gleick (editor), 1993, Water in Crisis: A Guide to the World's Fresh Water Resources.
NOTE: Numbers are rounded, so percent summations may not add to 100.

For pure and fresh (distilled) water with no dissolved salts, the dielectric constant of water obeys the single-relaxation Debye model for polar molecules [31].

$$\epsilon_{\mathrm{w}} = \epsilon_{\mathrm{w}\infty} + \frac{\epsilon_{\mathrm{w}0} - \epsilon_{\mathrm{w}\infty}}{1 + j2\pi f \tau_{\mathrm{w}}} \tag{1.4}$$

$\epsilon_{\mathrm{w}0}$ is the static dielectric constant (at $f = 0$, dimensionless), $\epsilon_{\mathrm{w}\infty}$ is the high frequency

dielectric constant ($f \to \infty$, dimensionless), τ_{w} is the relaxation time constant (s), and f is the frequency in Hz. We can write the dielectric constant with separate real and imaginary parts $\epsilon_{\mathrm{w}} = \epsilon'_{\mathrm{w}} - j\epsilon''_{\mathrm{w}}$.

$$\begin{aligned} \epsilon'_{\mathrm{w}} &= \epsilon_{\mathrm{w}\infty} + \frac{\epsilon_{\mathrm{w}0} - \epsilon_{\mathrm{w}\infty}}{1 + (2\pi f \tau_{\mathrm{w}})^2} \\ \epsilon''_{\mathrm{w}} &= \frac{2\pi f \tau_{\mathrm{w}}(\epsilon_{\mathrm{w}0} - \epsilon_{\mathrm{w}\infty})}{1 + (2\pi f \tau_{\mathrm{w}})^2} \end{aligned} \tag{1.5}$$

In addition to their dependence on frequency, ϵ'_{w} and ϵ''_{w} are also temperature dependent since $\epsilon'_{\mathrm{w}0}$, τ_{w}, and possibly $\epsilon'_{\mathrm{w}\infty}$ are all functions of the water temperature. The magnitude of the high frequency dielectric constant $\epsilon'_{\mathrm{w}\infty}$ was detertmined in [43]. Its dependence on temperature is weak; hence, it is considered to be a constant value of $\epsilon'_{\mathrm{w}\infty} = 4.9$. The relaxation time of pure water was obtained by Stogryn [82] by fitting a polynomial to experimental data.

$$\begin{aligned} 2\pi\tau_{\mathrm{w}}(T) &= 1.1109 \times 10^{-10} - 3.824 \times 10^{-12} T \\ &+ 6.938 \times 10^{-14} T^2 - 5.096 \times 10^{-16} T^3 \end{aligned} \tag{1.6}$$

where T is in °C. The relaxation frequency of pure water lies in the microwave region; $f_0 \approx 8.9$ GHz at $T = 0\ ^\circ C$ and $f_0 \approx 16.7$ GHz at $T = 20\ ^\circ C$. Klein and Swift [41] generated the following regression fit for $\epsilon_{\mathrm{w}0}(T)$.

$$\epsilon_{\mathrm{w}0}(T) = 88.045 - 0.4147T + 6.295 \times 10^{-14} T^2 + 1.075 \times 10^{-5} T^3 \tag{1.7}$$

The dielectric constant of the pure water is shown in Fig. 1.2 from 7 GHz up to 10 GHz, which is the frequency range we used in our measurements. The temperature of the freshwater is chosen as 4 °C. However, there is a weak dependence on the temperature.

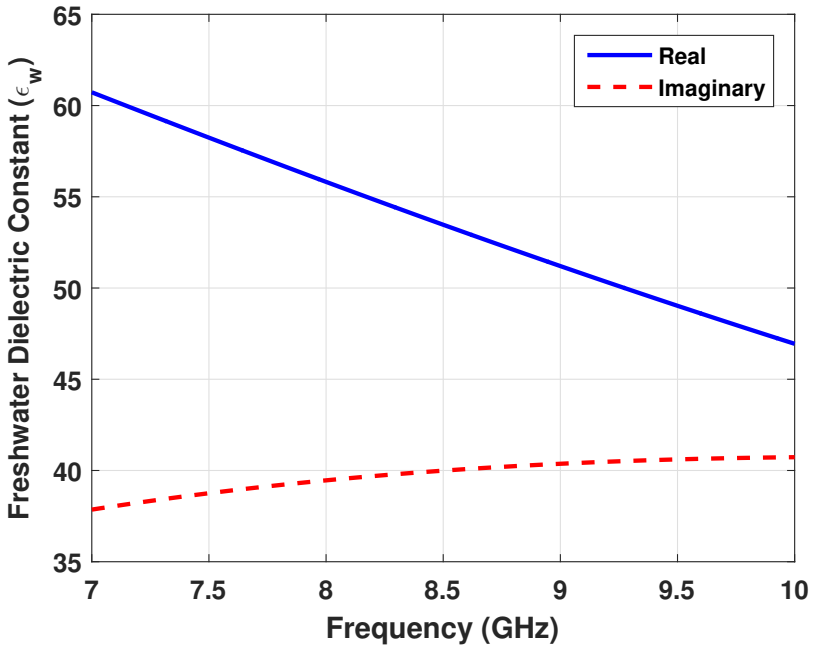

Figure 1.2: Dielectric constant of freshwater at 4 °C as a function of frequency.

1.2.2 Pure Ice

Unlike the liquid water , whose relaxation frequency lies in the microwave region, the relaxation frequency of pure ice f_{i0} occurs in the kilohertz region. Hence in the microwave region (f is in the order of GHz), $2\pi f\tau_i = \frac{f}{f_{i0}} \gg 1$. Therefore the Debye model expression for the ice simplifies as follow.

$$\epsilon_i' \approx \epsilon_{i\infty} \tag{1.8a}$$

$$\epsilon_i'' \approx \frac{\epsilon_{i0} - \epsilon_{i\infty}}{2\pi f\tau_i} = \frac{\alpha_0}{f} \tag{1.8b}$$

where $\alpha_0 = (\epsilon_{i0} - \epsilon_{i\infty})/2\pi\tau_i$. According to Mätzler and Wegmüller [51], ϵ_i' is essentially independent of frequency from 10 MHz to 300 GHz.

$$\epsilon_i' = 3.1884 + 9.1 \times 10^{-4}T \tag{1.9}$$

where $-40°C \leq T \leq 0$. In equation 1.8b, ϵ_i'' varies as $1/f$ and the coefficient α_0 is only function of the temperature T. However, ice exhibits an infrared absorption spectrum that includes a nonresonant term varying as f [89]

$$\epsilon_i'' = \frac{\alpha_0}{f} + \beta_0 f \tag{1.10}$$

α_0 and f are in GHz and β_0 is in $(\text{GHz})^{-1}$. The coefficients α_0 and β_0 are given by [50]

$$\alpha_0 = (0.00504 + 0.0062\theta) \cdot \exp(-22.1\theta) \qquad (\text{GHz}) \tag{1.11}$$

$$\begin{aligned} \beta_0 = & \frac{B_1}{T_k} \frac{\exp(b/T_k)}{[\exp(b/T_k) - 1]^2} + B_2 f^2 \\ & + \exp[-9.963 + 0.0372(T_k - 273.16)] \qquad (\text{GHz})^{-1} \end{aligned} \tag{1.12}$$

T_k is in Kelvin (K), $\theta = \frac{300}{T_k} - 1$, $B_1 = 0.0207$ K/GHz, $B_2 = 1.16 \times 10^{-11}\text{GHz}^{-3}$, and $b = 335$ K. The dielectric constant of pure ice is shown in Fig. 1.3 from 7 GHz up to 10 GHz, which is the frequency range we used in our measurements. The temperature of the pure ice is considered to be -20°C. It can be observed that the imaginary part of the dielectric constant of freshwater ice is very small, while its real part has an almost constant value. Evans [17] has also shown that the dielectric constant of the freshwater lake ice is constant and equals to 3.15 over microwave frequencies.

1.2.3 Dry Snow

Snow is the source of water we drink and use to grow food to eat. Mountains store snow in winter, and by slowly melting during the spring, they feed the streams and reservoirs and supply water to humans and crops. Snow also drives climate processes

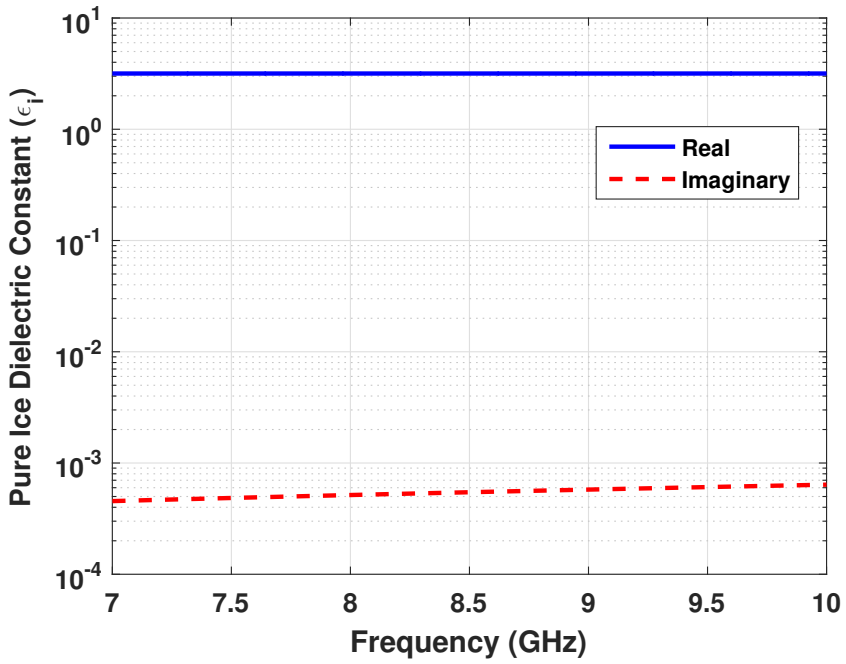

Figure 1.3: Dielectric constant of pure ice as a function of frequency. The temperature of the ice is -20°C.

and cools our planet; thus, understanding and monitoring the snow is essential.

Dry snow is composed of ice and air and contains no liquid water. The real part of the dielectric constant of dry snow, ϵ'_{ds}, may depend on the vertical extent of the snow accumulation, while the imaginary part is $\epsilon''_{ds} \approx 0$. An estimate of ϵ'_{ds} for the dry snow can be obtained by the empirical relationships, such as [91]

$$\epsilon'_{ds} = \begin{cases} 1 + 1.9\rho_s, & \rho_s \leq 0.5 \quad \mathrm{g \cdot cm^{-3}} \\ 0.51 + 2.88\rho_s, & \rho_s \geq 0.5 \quad \mathrm{g \cdot cm^{-3}} \end{cases} \tag{1.13}$$

where ρ_s is the density of dry snowpack. The average density $\langle \rho_s \rangle$ relates the snow depth (d) to the SWE, which is the depth of water that would result from complete melt of the snowpack in the absence of infiltration or runoff, as given by

$$\mathrm{SWE} = \left(\frac{\langle \rho_s \rangle}{\rho_w} \right) d \tag{1.14}$$

where the freezing point density of water is $\rho_w = 1.00$ g/cm^3. It follows from (1.13) that ϵ'_{ds} is not strongly dependent on frequency or temperature.

1.2.4 Soil

Soil is the underlying medium beneath the snowpack; hence, its dielectric properties is required in the forward modeling of snowpack. The dielectric constant of soil is investigated in more detail in [89].

1.2.4.1 Dry Soil

The dielectric constant of dry soil is essentially independent of both temperature and frequency. Dobson *et al.* [11], based on experiments on several soil types, determined that ϵ_{soil} for soils having extremely low moisture contents can be modeled as

$$\epsilon_{soil} \approx (1 + 0.44\rho_b)^2 - 0.062 \tag{1.15}$$

where ρ_b is the soil bulk density.

1.2.4.2 Wet Soil

The presence of liquid water in soil can make the dielectric constant of soil dependent on frequency and temperature. The dielectric constant of wet soil is investigated in detail in [89, 93, 11, 28, 74, 68]. Above 0°C, the real and imaginary parts of the dielectric constant of soil are weakly dependent on temperature, while they decrease drastically as temperature crosses below the freezing temperature of water [25]. In addition, Hallikainen *et al.* [28] illustrated for one of the measured soil types that ϵ'_{soil} decreases with increasing frequency between 1.4 and 18 GHz, whereas ϵ''_{soil} increases with increasing frequency.

1.3 Structure of the Thesis

The thesis introduces a novel microwave radiometric technique, known as wide-band autocorrelation radiometry (WiBAR), to measure the lake ice and dry snow packs. In Chapter II, the autocorrelation radiometry background as well as WiBAR's physics of operation are fully discussed. The rest of Chapter II presents the forward modeling of a single layer of snow/ice over soil/water, an icepack with a top snow layer, and a low-loss layer with variable thickness.

The implemented first and second generations of WiBAR X-band and first generation of WiBAR L- and S-band are discussed in Chapter III. The measurement approach and the system requirements needed to design a WiBAR instrument are also fully explained. The rest of Chapter III presents snow/ice pack simulated measurement as well as field measurements using WiBAR instruments.

The error analysis of the measured time delay by WiBAR for a single and multi layer media are discussed in Chapter IV. Finally, Chapter V concludes the thesis, and the future directions are also explained in this chapter.

CHAPTER II

Wideband Autocorrelation Radiometry

2.1 Introduction

More than one-sixth of the world's population (1.2 billion people) relies on seasonal snowpack and glaciers for their water source [5]. The changes in snow quantity and snowmelt timing are underway and have serious consequences (https://snow.nasa.gov/), so monitoring these changes would be beneficial and is needed. Current microwave remote sensing of snow is based on the scatter darkening method [14, 13, 12, 81]. Estimating the snow thickness and SWE via microwave scatter darkening is not robust since the scattering theory yields only the form of the frequency-dependent scatter darkening but not a reliable amplitude estimation. It is highly dependent on the microscopic properties of the snowpack (e.g. grain size), which varies considerably from place to place and time to time. Thus, the algorithm should be empirically tuned to a region's typical snowpack [26]. However, non-seasonably warm weather and early and late season diurnal heating cause metamorphic growth of the ice grains in the snowpacks, which turns into a greater scatter darkening [48], and the snowpack looks deeper when in fact it is compressing. In addition, tuning algorithms become very complicated or even unworkable for terrains that are more complex than the Canadian Great Plains.

Nonetheless, microwave remote sensing is ideal for spaceborne observations of

snow packs because it is independent of daylight and can penetrate the atmosphere regardless of weather. To change the focus from the microscopic properties of the snow to the macroscopic properties, there have been a number of investigations of techniques that measure the travel time through the snow pack. At the plot scale, Frequency Modulated Continuous Wave (FMCW) radar has been used both looking down from above [49] and up from below [64]. Repeat pass Interferometric Synthetic Aperture Radar (InSAR) uses phase differences to measure the propagation time from space [22, 45]. While radar has the potential for very high spatial resolution, it is hungry for power, which can make radar space missions expensive. To address this issue, we are initiating an exploration of a passive microwave technique, known as wideband autocorrelation radiometry (WiBAR), that measures the travel time. To demonstrate the concepts developed here, we directly measure the vertical extent of a lake ice pack at different observation angles away from nadir by passively sensing the microwave propagation time through the pack. We expect that the technique and principles presented here will also be applicable for quantifying the accumulation of dry snowpack as an ultimate objective of this research.

2.2 Autocorrelation Radiometry Background

Passive microwave remote sensing of icepack and snowpack parameters, such as vertical extent of the pack, have been investigated by researchers using various microwave sensors [29, 85, 24]. Swift *et al.* [85] discussed the microwave radiometer measurements of the emission from saline ice as a function of ice thickness. They used a C-band stepped-frequency microwave radiometer (SFMR) with tunable center frequency between 4 and 8 GHz with a bandwidth of 100 MHz. They derived the

emissivity for an ice layer over water, as given by

$$e = \frac{(1 - |R_{01}|^2)(1 - L_v |R_{12}|^2)}{1 + L_v |R_{01}|^2 |R_{12}|^2 + 2\sqrt{L_v} R_{01} R_{12} \cos(2k_{1z} d_{ice})} \tag{2.1}$$

where R_{01} is the Fresnel reflection coefficient of air to ice, R_{12} is the Fresnel reflection coefficient of ice to water, k_{1z} is the vertical component of the phase constant for ice, d_{ice} is the ice thickness, and L_v is an attenuation factor due to volume scattering. The term L_v depends on the nature of the scatterers and on d_{ice}, but the rest of the terms have no variation with respect to d_{ice}. If the ice layer has negligible loss, $L_v = 1$ and a radiometer would observe a maximum and a minimum in brightness temperature at every quarter wavelength in thickness. However, they were rarely able to observe the quarter-wave resonance from the experimental results. They concluded that all quarter-wave resonances are suppressed as a result of surface roughness destroying the coherence of the slab if the rms surface roughness is of the order of an electromagnetic wavelength [2]. Swift *et al.* [86] applied (2.1) to the emissivity of ice on Lake Erie, and attributed their inability to observe the interference fringes in the measurements to surface roughness caused by ship traffic. On the other hand, Harrington *et al.* [29] reported various observations of the interference fringes using SFMR, such as on a flight flown over smooth ice on Claytor Lake in Virginia on March 7, 1978 and for a sea ice observation in an area north of Prudhoe Bay in the Beaufort Sea on March 20, 1979. Some narrowband observations of this coherent emissivity include those of lake ice by England and Johnson [16] and in soil by Jackson *et al.* [33]. Jackson *et al.* reported an oscillatory behavior of the brightness temperature of smooth, bare soil after irrigation, which they modeled as the downward propagation of a wetting front. Johnson *et al.* [37] also reported the oscillatory behavior in brightness temperature of dry soil with respect to frequency in the presence of buried objects.

Although the measurement of the coherent effect from snow and ice packs has

been abandoned for decades, we feel it is worth investigating given the technological advancements since the development of SFMR. Our initial measurements use a process similar to that of SFMR: we measure the emissivity as a function of frequency, and extract the coherent effect from the spectrum. England [15] has shown that a time-domain approach is superior in terms of reduced integration times, but commercial-off-the-shelf (COTS) hardware is not as readily available for that approach.

2.3 Wideband Autocorrelation Radiometry (WiBAR): Physics of Operation

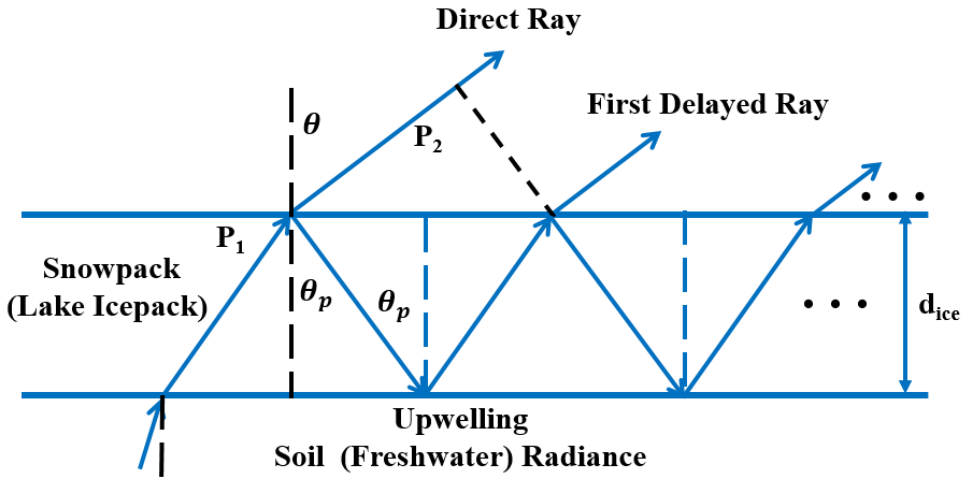

Figure 2.1: Remote sensing of microwave travel time through the pack with thickness d_{ice}. The first delayed ray is delayed by $\tau_{delay} = 2\tau_p - \tau_{air}$ relative to the direct ray.

Wideband autocorrelation radiometry (WiBAR) of dry snowpacks and lake icepacks was proposed by England in [15, 16]. It is a remote sensing method that can directly measure the microwave propagation time τ_{delay} through low loss terrain covers and other layered surfaces. Terrestrial examples are snow packs and lake ice packs. Presuming these geophysical features are accurately described by (2.1), the thermal radiation emitted from below the pack traverses the pack and is split at the upper interface into two rays that travel towards the radiometer's antenna, as shown in

Fig. 2.1. The portion of power that is transmitted across the upper interface towards the radiometer's antenna constitutes the direct ray. The portion of power that is reflected from the upper interface is the delayed ray. It traverses the pack twice upon reflection from the lower interface before traveling to the radiometer's antenna, with a one-way transit time in the pack of τ_p. Thus, there are two rays received by the radiometer, the direct ray and a delayed copy of it. The delayed ray arrives at the radiometer with the time delay τ_{delay}, relative to the direct ray, where [15, 60]

$$\begin{aligned} \tau_{delay} &= 2\tau_p - \tau_{air} \\ \tau_{air} &= \frac{2d \tan\theta_p \sin\theta}{c} \\ \tau_p &= \left(\frac{d}{\cos\theta_p}\right)\left(\frac{n_p}{c}\right) \end{aligned} \tag{2.2}$$

τ_{air} is the travel time in the air between points P_1 and P_2, θ is the incidence angle, n_p is the refractive index of the pack, and c is the speed of light in free space. The microwave propagation time τ_{delay} through the pack yields a measure of its vertical extent, d, since the argument of the cosine in (2.1) is $2k_{z1}d = 2\pi f \tau_{delay}$. The incidence angle θ and the angle θ_p are related by Snell's law.

$$n_p \sin\theta_p = \sin\theta \tag{2.3}$$

In case of homogeneous and isotropic pack, (2.2) can be simplified using (2.3).

$$\tau_{delay} = \frac{2d}{c}\sqrt{n_p^2 - \sin^2\theta} \tag{2.4}$$

This expression is valid for freshwater lake icepack, which has an almost constant refractive index, $n_p = n_{ice} = \sqrt{3.15}$, over microwave frequencies [17].

On the other hand, the refractive index of the dry snowpack ($n_p(z) = n_{snow}(z)$)

may depend on the vertical extent of the pack [59].

$$\tau_{delay} = \frac{2}{c} \int_0^d \sqrt{n_p(z)^2 - \sin^2\theta} dz \tag{2.5}$$

However, the refractive index of snow can be estimated using the result obtained in Section 1.2.3 for its dielectric constant , as given by

$$\begin{aligned} n_{snow} &= \sqrt{1.0 + 1.9\rho_s}, && \text{for} \quad \rho_s \leq 0.5 \quad \text{g} \cdot \text{cm}^{-3} \\ &= \sqrt{0.51 + 2.88\rho_s}, && \text{for} \quad \rho_s \geq 0.5 \quad \text{g} \cdot \text{cm}^{-3} \end{aligned} \tag{2.6}$$

Painter *et al.* [66] have shown with their Airborne Snow Observatory (ASO) that measurements of snow depth (via lidar) coupled with snow density provided by a model are sufficient for retrieving SWE. We expect a similar approach will be necessary for applying WiBAR to snow. It should be noted that wetness in the pack will introduce an attenuation in the wave propagating through the pack, which will reduce the amplitude of the autocorrelation peak.

2.4 Forward Modeling of Dry Snowpack or Lake Icepack

A layered medium with boundaries at $z = -d_0, -d_1, ..., -d_N$ with $d_0 = 0$ is shown in Figure 2.2. It is assumed that the top (region 0) and the bottom (region $N + 1$) layers are semi-infinite. It is assumed that the temperature profile of the layers is uniform, the layers are homogeneous, and the interfaces between the layers are electrically smooth. Hence, the Fresnel reflection coefficients can be used in order to obtain the reflectivity and emissivity of the layered medium. The plane of incidence is determined by the z-axis and the incident $\overline{k}$ vector. The horizontally polarized (TE) configuration is discussed in this section since the outdoor measurements were conducted with horizontally polarized (TE) configuration. However, the solutions for

the vertically polarized (TM) configuration can be readily obtained using the duality relationship $\overline{E} \rightarrow \overline{H}$, $\overline{H} \rightarrow -\overline{E}$, and $\mu \leftrightarrow \epsilon$.

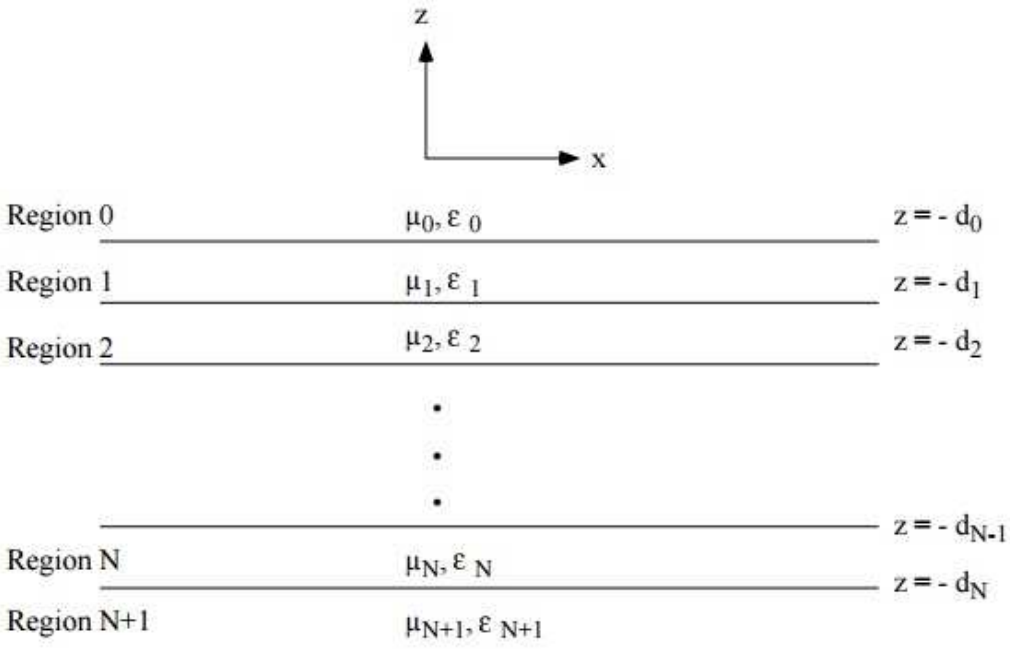

Figure 2.2: Configuration of N+1 layered medium.

For a horizontally polarized (TE) incident wave, the reflection coefficient in region l at the interface separating regions l and $l+1$ is given by

$$R_{l(l+1)} = \frac{\mu_{l+1} k_{lz} - \mu_l k_{(l+1)z}}{\mu_{l+1} k_{lz} + \mu_l k_{(l+1)z}} \tag{2.7}$$

where A_l and B_l are the coefficients of the upward and downward going wave in region l, respectively. In addition, k_{lz} is the propagation constant along the z-axis in each region l. By forcing the boundary condition at each interface, it can be shown that [87]

$$\frac{A_l}{B_l} e^{-i2k_{lz}d_l} = \frac{\frac{A_{l+1}}{B_{l+1}} e^{-i2k_{(l+1)z}d_{l+1}} e^{i2k_{(l+1)z}(d_{l+1}-d_l)} + R_{l(l+1)}}{\frac{A_{l+1}}{B_{l+1}} e^{-i2k_{(l+1)z}d_{l+1}} R_{l(l+1)} e^{i2k_{(l+1)z}(d_{l+1}-d_l)} + 1} \tag{2.8}$$

This is a recurrence relation which can be used to find $R_h = A_0/B_0$ starting from

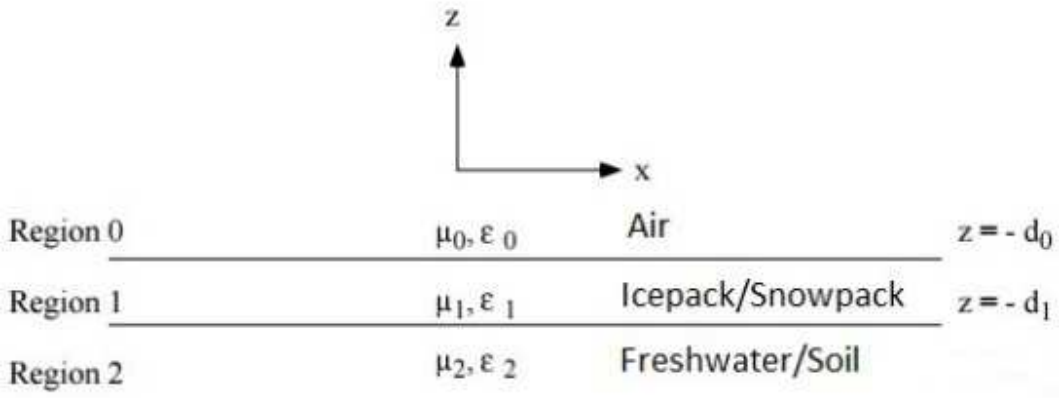

Figure 2.3: Configuration of the lake icepack without a snowpack on top over freshwater or a snowpack over soil.

$A_{N+1}/B_{N+1} = 0$, since there is no upward going wave ($A_{N+1} = 0$) in the semi-infinite region $N + 1$. The emissivity e can now be obtained from the reflectivity r by

$$e = 1 - r \tag{2.9}$$

and the reflectivity is given by

$$r = |R|^2 \tag{2.10}$$

where R is the reflection coefficient of the layered medium in either horizontally (TE) or vertically (TM) polarized configuration.

2.4.1 Forward Modeling of a Single Layer of Snow/Ice over Soil/Water

For the case of a lake icepack without a snowpack on top over freshwater or a snowpack over soil, the configuration is shown in Figure 2.3, which is similar to Figure 2.1. Using the recurrence relation (2.8), the reflection coefficient of this medium is

given by

$$R = \frac{R_{01} + R_{12}e^{i2k_{1z}d_1}}{1 + R_{01}R_{12}e^{i2k_{1z}d_1}} \tag{2.11}$$

R_{01} and R_{12} are the Fresnel reflection coefficients at the air-snow/ice and snow/ice-soil/freshwater interfaces, respectively, and is given by the equation (2.7). Using the equation (2.9), the emissivity can be obtained as follow

$$e = \frac{(1 - |R_{01}|^2)(1 - |R_{12}|^2)}{1 + (|R_{01}|\,|R_{12}|)^2 + 2R_{01}R_{12}\cos(2k_{1z}d_1)} \tag{2.12}$$

The system design parameters are discussed in Chapter III.

2.4.2 Forward Modeling of an Icepack with a Top Snow Layer

The presence of a snowpack on the icepack adds another multipath. The configuration is as shown in Figure 2.4. The first delayed ray of icepack and snowpack arrives at the radiometer with the time delays τ_{ice} and τ_{snow}, respectively, relative to the direct ray. These time delays are given by (2.4) and (2.5). Using the recurrence relation (2.8), the reflection of this medium is given by

$$R = \frac{R_{01} + \left[\frac{R_{23}e^{i2k_{2z}(d_2-d_1)}+R_{12}}{R_{23}R_{12}e^{i2k_{2z}(d_2-d_1)}+1}\right]e^{i2k_{1z}d_1}}{\left[\frac{R_{23}e^{i2k_{2z}(d_2-d_1)}+R_{12}}{R_{23}R_{12}e^{i2k_{2z}(d_2-d_1)}+1}\right]R_{01}e^{i2k_{1z}d_1} + 1} \tag{2.13}$$

In this equation, R_{12} and R_{23} are the reflection coefficients at the snow-ice and ice-freshwater interfaces, respectively. In addition, R_{01} is the reflection coefficient at the

air-snow interface. Similarly, the emissivity of this medium is given by [87, 61, 54]

$$e(f) = \frac{\bar{e}}{\left\{ 1 + 2\Big[A_i \cos(\omega\tau_{ice}) + A_s \cos(\omega\tau_{snow}) + A_\Sigma \cos\Big(\omega\big(\tau_{snow} + \tau_{ice}\big)\Big) + A_\Delta \cos\Big(\omega\big(\tau_{snow} - \tau_{ice}\big)\Big)\Big] \right\}} \tag{2.14}$$

where $2k_{1z}d_{snow}$ and $2k_{2z}d_{ice}$ are substituted with $\omega\tau_{snow}$ and $\omega\tau_{ice}$, respectively, $\omega = 2\pi f$, $\bar{e}$ is the mean emissivity over frequency, A_i, A_s, A_Σ, and A_Δ are one half of the amplitudes of the ripple due to icepack time delay, snowpack time delay, sum of the time delays, and difference of the time delays, respectively, in the emissivity as a function of frequency. They are given by

$$\bar{e} = (1 - |R_{01}|^2)(1 - |R_{12}|^2)(1 - |R_{23}|^2) \ / C_0 \tag{2.15a}$$

$$A_i = R_{12}R_{23}(1 + |R_{01}|^2) \ / C_0 \tag{2.15b}$$

$$A_s = R_{01}R_{12}(1 + |R_{23}|^2) \ / C_0 \tag{2.15c}$$

$$A_\Sigma = R_{01}R_{23} \ / C_0 \tag{2.15d}$$

$$A_\Delta = R_{01}R_{23}\,|R_{12}|^2 \ / C_0 \tag{2.15e}$$

where $C_0 = 1 + |R_{01}|^2\,|R_{12}|^2 + |R_{01}|^2\,|R_{23}|^2 + |R_{12}|^2\,|R_{23}|^2$.

It can be observed from equation (2.14) that time delays proportional to the summation and difference of the layer thicknesses have also been introduced. The presence of a snowpack on the icepack adds another multi-path interference, which can effect the lake icepack thickness measurement.

2.4.3 Forward Modeling of a Low Loss Layer with Variable Thickness

The presence of variable layer thicknesses in a footprint of the radiometer's antenna will add different microwave propagation times through the layer under investi-

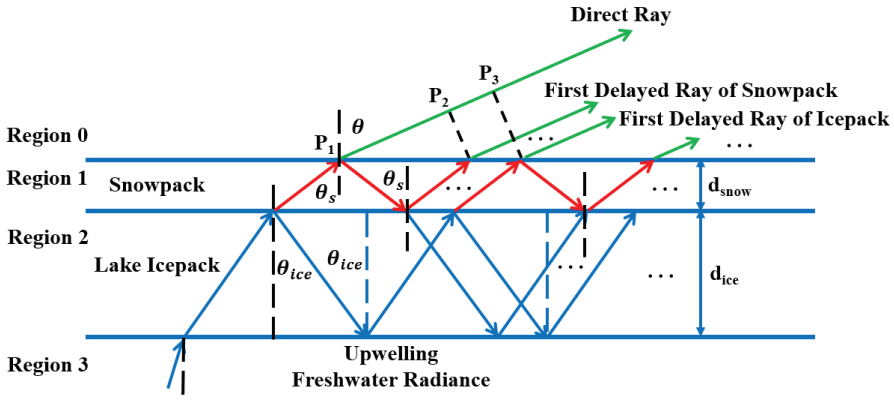

Figure 2.4: Configuration of the lake icepack with thickness d_{ice} in the presence of a snow cover with thickness d_{snow}.

gation. This scenario becomes more likely the higher the WiBAR instrument is above the surface of the layer. If this variable thickness takes the form of a finite number of distinct thicknesses, we can divide the footprint observed by the antenna to $m \times n$ sub-pixels each with different but uniform thicknesses, as shown in Figure 2.5. Then, we can use the model described in [57] to find the emissivity of each sub-pixel, as given by [56]

$$e_{ij}(f, \theta_0) = \frac{(1 - |R_{01}|^2)(1 - |R_{12}|^2)}{1 + (|R_{01}|\,|R_{12}|)^2 + 2R_{01}R_{12}\cos(2k_{1z}d_{ij})} \tag{2.16}$$

where R_{01} is the Fresnel reflection coefficient of air to ice (snow), R_{12} is the Fresnel reflection coefficient of ice (snow) to water (soil), k_{1z} is the vertical component of the wavenumber in ice (snow), d_{ij} is the thickness of each sub-pixel, and $i = 1, ..., m$ and $j = 1, ..., n$ are the indices for each sub-pixel in the x or y directions.

As a first step towards understanding the signature of a single layer with continuously varying thickness within the field of view, this thesis shows the ability of WiBAR in measuring a layer having distinct thickness values within the antenna's footprint. This can be distinguished from the multi-layer medium scenario [54] by the fact that the multi-layer contains time lags corresponding not only to the individual layers, but also to the linear combinations of those time lags (eg. sums and

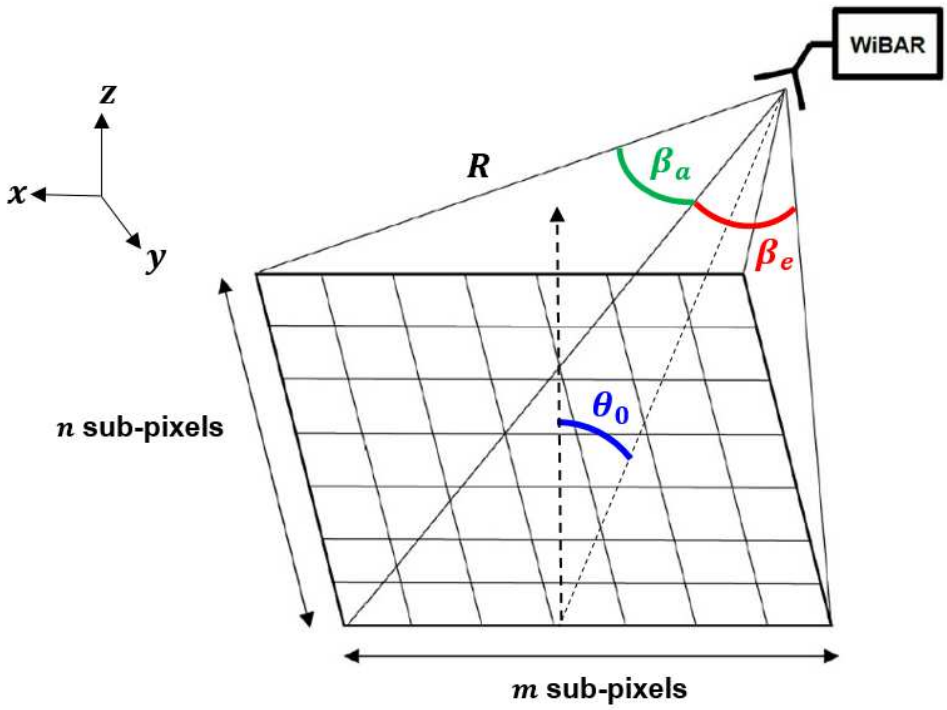

Figure 2.5: The observed footprint of the radiometer's antenna. The footprint area is divided to $m \times n$ sub-pixels. The pack's thickness is different but uniform in each sub-pixel.

differences), while the case under consideration has distinct time lags but no linear combination of them.

Each sub-pixel can have a different contribution to the received power by the radiometer, $P(f, \theta_0)$, due to non-uniformity of the antenna's gain pattern, $g(\theta, \phi)$. Hence, we can define a constant $0 < a_{ij} \leq 1$, which is ratio of the antenna's gain pattern integrated over the solid angle confined by each sub-pixel to that integrated over all solid angles, as given by

$$a_{ij} = \frac{\int_{\theta_i}^{\theta_{i+1}} \int_{\phi_j}^{\phi_{j+1}} g(\theta - \theta_0 + \frac{\beta_e}{2}, \phi + \frac{\beta_a}{2}) d\Omega}{\iint_{4\pi} g(\theta, \phi) d\Omega} \tag{2.17}$$

where β_e and β_a are the half-power beamwidths in elevation and azimuth planes, respectively, $\theta_i = \frac{(x_{i-1} - x_0)}{R}$, $\phi_j = \frac{(y_{j-1} - y_0)}{R}$, x_i and y_j are the locations of the borders of each sub-pixel in x and y directions, respectively, and R is the slant range. Because

the delayed path is horizontally displaced from the direct path, we assume that the extent of each sub-pixel in either x or y directions is such that at least the first delayed path from each sub-pixel can be observed; otherwise, the thickness of that sub-pixel cannot be detected with (2.4).

The total received power, P, by the WiBAR is given by

$$P(f,\theta_0) = K\Big[\left(\Sigma_{i=1}^{m}\Sigma_{j=1}^{n} a_{ij}e_{ij}(f)\right)T_0 + T_{REC}(f)\Big]BG(f) \tag{2.18}$$

where K is Boltzmann's constant, $T_{REC}(f)$ is the receiver noise temperature, T_0 is the physical temperature of the target, B is the noise bandwidth, and $G(f)$ is the radiometer's gain. To remove the frequency dependencies of the gain and receiver temperature and extract the total emissivity, we use the calibration procedure explained in [57]. Using the Wiener-Khinchin theorem, the autocorrelation function (ACF) of the received power spectrum is the inverse fast Fourier transform (IFFT) of the emissivity spectrum [57]. Because the IFFT is a linear operation, the arithmetic averaging in (2.18) applies also to the ACFs that can be attributed to the sub-pixels. As a result, for each sufficiently distinct d_{ij} in (2.12), the ACF will have a distinct peak corresponding to it. Nonetheless, while it is at least theoretically possible to extract the sub-pixel thicknesses from the observed ACF, it is not possible from a single measurement to locate those sub-pixel thicknesses except to say that they are somewhere within the footprint.

CHAPTER III

Design and Implementation of WiBAR Instruments

3.1 Introduction

In the search for an alternative way to traditional scatter darkening techniques for microwave remote sensing of snowpack or icepack, we developed a new and low-cost passive microwave remote sensing technique, known as wideband autocorrelation radiometry (WiBAR) [57, 15, 58, 59, 60], as explained in Chapter II. This technique offers a direct method to remotely measure the microwave propagation time difference of multipath microwave emission from low-loss layered surfaces, such as a dry snowpack and a freshwater lake icepack. The microwave propagation time difference through the pack yields a measure of its vertical extent; thus, this technique provides a direct measurement of depth. In this chapter we are discussing the design of a WiBAR instrument in frequency domain approach. We also show the measurement results that we have done so far for lake icepack.

3.2 Frequency Domain Wideband Autocorrelation Radiometer (FD-WiBAR)

Our WiBAR instrument is designed for observing the coherent effect in lake icepack or dry snowpack. We introduce the radiometer design to measure the ice and snow thicknesses in different scenarios of a single layer of snow/ice, two layer of ice with snow cover, and a single layer of snow/ice with variable thicknesses. We introduce the radiometer design to measure the pack thickness using frequency domain approach.

3.2.1 FD-WiBAR Instruments for Ice Thickness Measurement

3.2.1.1 First Version

The operating frequency is chosen to be 7-10 GHZ for measuring the lake icepack. This bandwidth is high enough to permit 3 GHz bandwidth operation with an Advanced Technical Materials (ATM) standard gain X-band horn antenna with 24 dBi gain (ATM Microwave 112-443-6) yet low enough to avoid much extinction in the ice. This antenna has an E-plane aperture of $a_v = 19.1$ cm and an H-plane aperture of $a_H = 27.9$ cm. The receiver is a field-portable spectrum analyzer (Agilent N9344C), which produces a fixed number of frequency samples in the spectrum ($N_f = 461$), much greater than that of SFMR. The antenna and the spectrum analyzer are joined with isolators, low noise amplifiers (LNAs), and a band pass filter (BPF), which provide appropriate low-noise amplification and filtering of the Planck power to levels that can be measured by the spectrum analyzer. The noise figure of the LNA is 2 dB, and the receiver's noise figure, F, is estimated at 2.38 dB. The receiver's return loss is also about 17 dB. The schematic of the receiver gain chain of the first version of X-band WiBAR is shown in Fig. 3.1. The X-band WiBAR system is also shown is Fig. 3.2. This instrument was used at the Keweenaw Waterway South Entry Light in

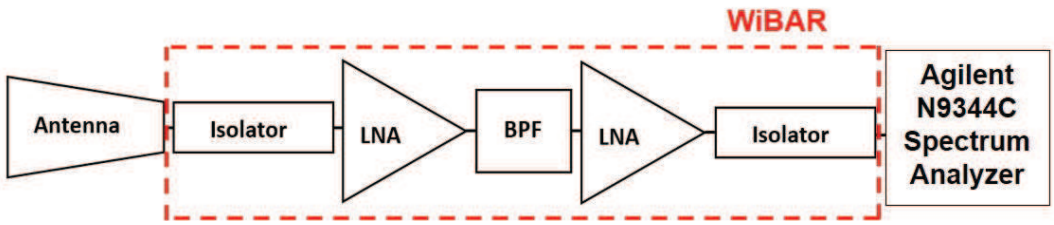

Figure 3.1: The schematic of the receiver gain chain of the first version of X-band WiBAR radiometer. The antenna is an ATM (112-443-6) standard gain horn with aperture dimension of 19.1 cm by 27.9 cm, and an elevation beamwidth of 8.7°. The isolators are UTE (CT-5155-OT). The LNAs are WanTcom (WBA80180B) with 35.0 dB gain and 2.0 dB noise figure. The filter is a custom 7 - 10 GHz bandpass filter made by K&L Microwave.

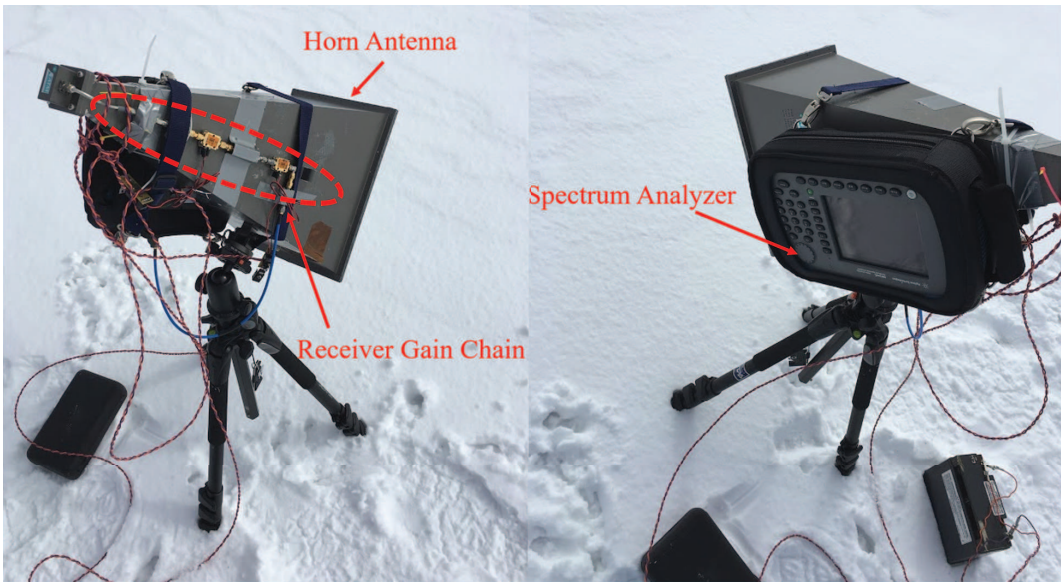

Figure 3.2: The first version of the X-band WiBAR system in frequency domain approach. The spectrum analyzer is strapped to one side of the antenna, and the receiver is attached to the other side. This system was used for lake icepack measurement only in Winter 2016.

Winter 2014 [63] and the University of Michigan Biological Station in Winter 2016.

3.2.1.2 Second Version

The first version of X-band WiBAR suffers from the heavy weight of the spectrum analyzer on one side of the antenna. It also has a fixed number of frequency points, which limits us from investigating the effect of the number of frequency points in

Figure 3.3: The Signal Hound USB-SA44B spectrum analyzer. The frequency operation range is from 1 Hz to 4.4 GHz. The resolution bandwidth (RBW) can be any value from 0.1 Hz up to 250 kHz (https://www.signalhound.com).

the spectrum. To address these issues and make the system more robust and easy to use, we have used the USB-SA44B spectrum analyzer from Signal Hound, which weighs much less and gives us the ability to control the number of frequency points. This spectrum analyzer is shown in Fig. 3.3. Since this spectrum analyzer goes up only to 4.4 GHz, we have used a fixed frequency synthesizer (Z-Comm RFS5900A-LF) operating at 5900 MHz with a mixer to down convert the received signal before it was fed to the spectrum analyzer. The typical phase noise of the frequency synthesizer is -80 dBc/Hz, -85 dBc/Hz, and -103 dBc/Hz at the 1 kHz, 10 kHz, and 100 kHz offsets, respectively. The receiver's noise figure and return loss are the same as the first version of X-band WiBAR since the RF front-end stage has not been changed. A Raspberry Pi was used to control the WiBAR data acquisition. The schematic of the receiver gain chain of the second version of X-band WiBAR is shown in Fig. 3.4. The X-band WiBAR system is also shown is Fig. 3.2. This instrument has been operational since Winter 2018.

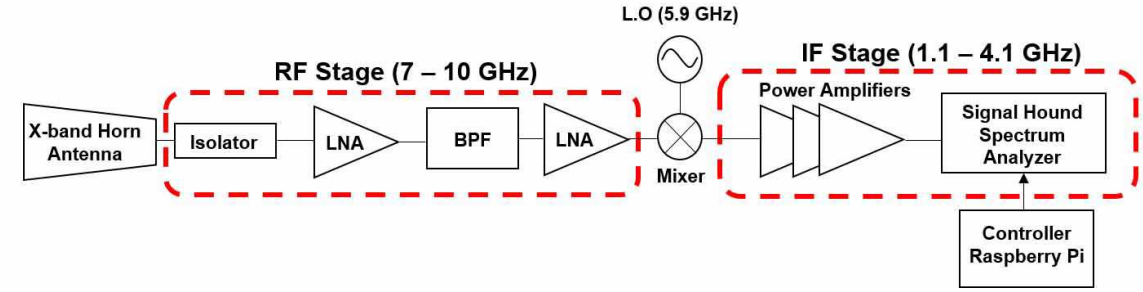

Figure 3.4: The schematic of the receiver gain chain of the second version of the X-band WiBAR radiometer. The antenna is an ATM (112-443-6) standard gain horn with aperture dimension of 19.1 cm by 27.9 cm, and an elevation beamwidth of 8.7°. The isolator is UTE (CT-5155-OT). The LNAs are WanTcom (WBA80180B) with 35.0 dB gain and 2.0 dB noise figure. The filter is a custom 7 - 10 GHz bandpass filter made by K&L Microwave. The frequency synthesizer is Z-comm (RFS5900A-LF) operating at 5900 MHz. A Raspberry Pi is used to control the data acquisition.

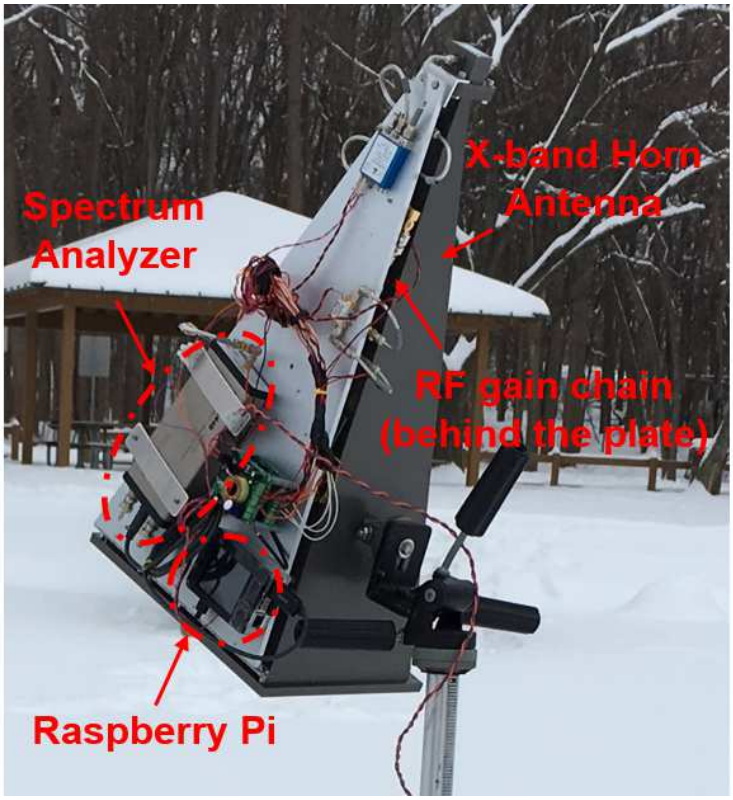

Figure 3.5: The second version of the X-band WiBAR system in frequency domain approach. The Signal Hound spectrum analyzer as well as the receiver gain chain is attached to the plate on one side of the antenna. This system was used for lake icepack measurement and has been operational since Winter 2018.

3.2.2 FD-WiBAR Instruments for Snow Thickness Measurement

The WiBAR instrument to measure the travel time in a dry snowpack operates in the frequency range 1-2 GHz (L-band). This bandwidth is high enough to permit the operation of a wide-band antenna and low enough to avoid much extinction in the snowpack. The schematic of this receiver gain chain is shown in Fig. 3.6. It can be observed that there is no mixer and IF stage in this receiver compared to the second version of the X-band WiBAR receiver, as shown in Fig. 3.5, since the received signal is in the frequency range of the Signal Hound spectrum analyzer. The noise figure of the LNA is 0.38 dB, and the receiver's noise figure, F, is estimated at 1.87 dB. The receiver's return loss is also about 12 dB. The L-band WiBAR is also shown in Fig. 3.7. This system has been operational since Winter 2018. In order to increase the bandwidth of operation, we also designed and built a S-band WiBAR. This system is similar to the L-band WiBAR except the instruments are operating in S-band, and its schematic is similar to Fig. 3.6. The antenna is an ATM gain horn antenna (340-442-2) with aperture dimension of 29.99 cm by 47.72 cm, and an elevation beamwidth of about 16.3°. The isolator is MCLI (IS-9). The LNAs are WanTcom (WZA305) with 27 dB gain and 1.2 dB noise figure. The receiver's noise figure is estimated at 1.7 dB, and its return loss is about 16 dB. The S-band WiBAR is also shown in Fig. 3.8. This system has been operational since Winter 2019.

3.2.3 Measurement Approach

In the frequency domain approach, the data are collected in frequency domain similar to SFMR. The received power, P, at the spectrum analyzer is given by

$$P(f) = KT_{SYS}(f)B\ G(f) \tag{3.1}$$

$$= K\left(e(f)T_0 + T_{REC}(f)\right) B\ G(f) \tag{3.2}$$

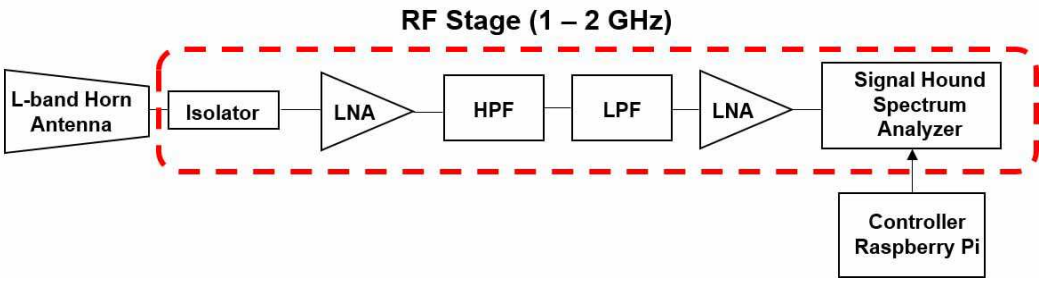

Figure 3.6: The schematic of the receiver gain chain of the L-band WiBAR radiometer. The antenna is a Seavey horn antenna (9804-800) with aperture dimension of 73.66 cm by 78.74 cm, and an elevation beamwidth of about 23°. The isolator is MCLI (IS-1-1). The LNAs are MiniCircuits (ZX60-P33ULN+) with 17.3 dB gain and 0.38 dB noise figure. The filters are 910-3000 MHz high-pass (SHP-900+) and DC-2000 MHz low-pass (VLP-24) filters made by Mini-Circuits. A Raspberry Pi is used to control the data acquisition.

where K is Boltzmann's constant, $T_{SYS}(f)$ is the radiometer system temperature, B is the noise bandwidth, and $G(f)$ is the radiometer's gain. The system temperature itself is composed of the sum of the receiver noise temperature, $T_{REC}(f)$, and the product of the target emissivity, $e(f)$, and the physical temperature of the target, T_0. Those terms which are expected to have variations with frequency are indicated as being functions of frequency.

To remove the frequency dependencies of the gain and receiver temperature, spectra are calibrated to emissivity with beam-filling measurements of absorber and the sky, as given by (3.3), which approximate emissivities of unity and zero, respectively.

$$\hat{e}(f) = \frac{P_{pack}(f) - P_{sky}(f)}{P_{abs}(f) - P_{sky}(f)} \tag{3.3}$$

where P_{pack} is the power received from the pack, P_{sky} is the power received from sky, and P_{abs} is the power received from microwave absorber. This emissivity spectrum demonstrates a periodic interference pattern in frequency domain, which corresponds to a peak in the autocorrelation domain [15]. Using the Wiener Khinchin theorem, the autocorrelation response, $\Phi(\tau)$, of the power spectrum is equal to the inverse

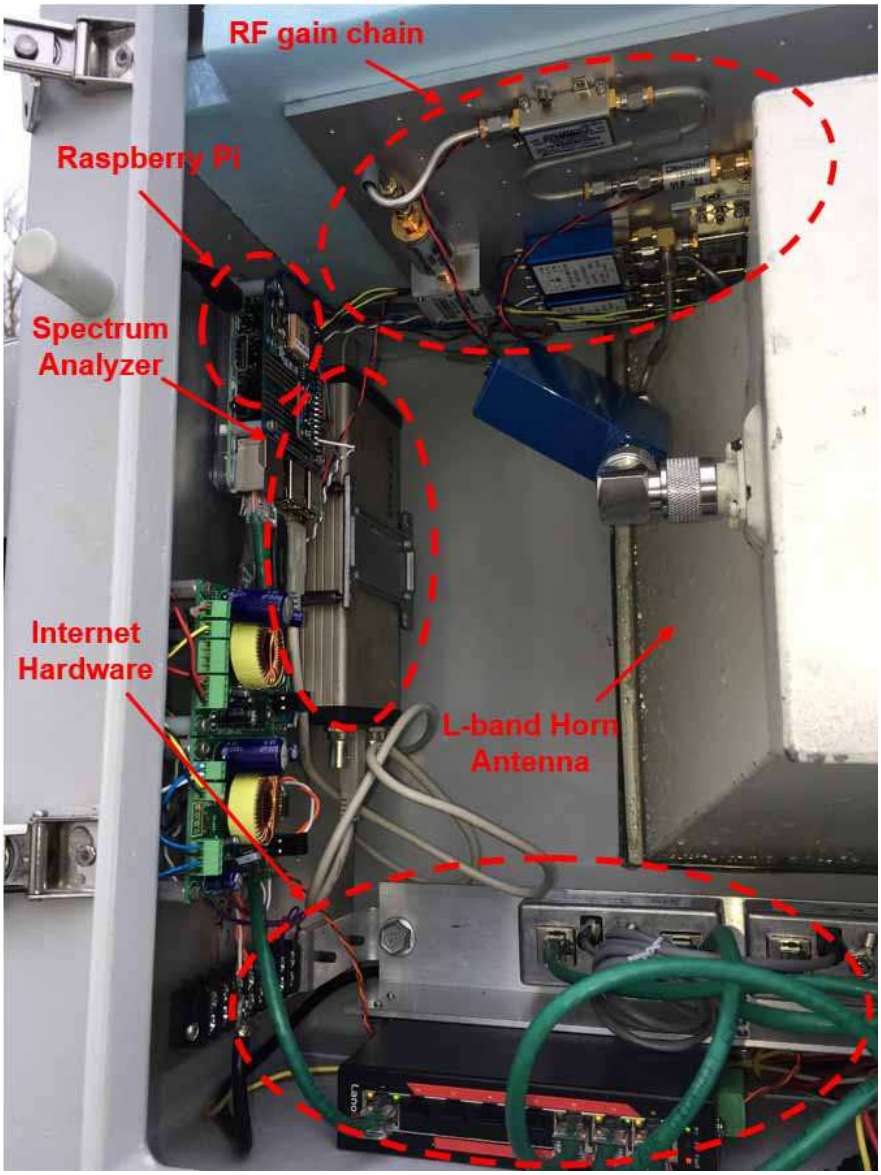

Figure 3.7: The L-band WiBAR system in frequency domain approach. The Signal Hound spectrum analyzer as well as the receiver gain chain is attached to a plate inside a box enclosure, and the throat of the antenna in the box is also shown. This system was used for snowpack measurement and has been operational since Winter 2019.

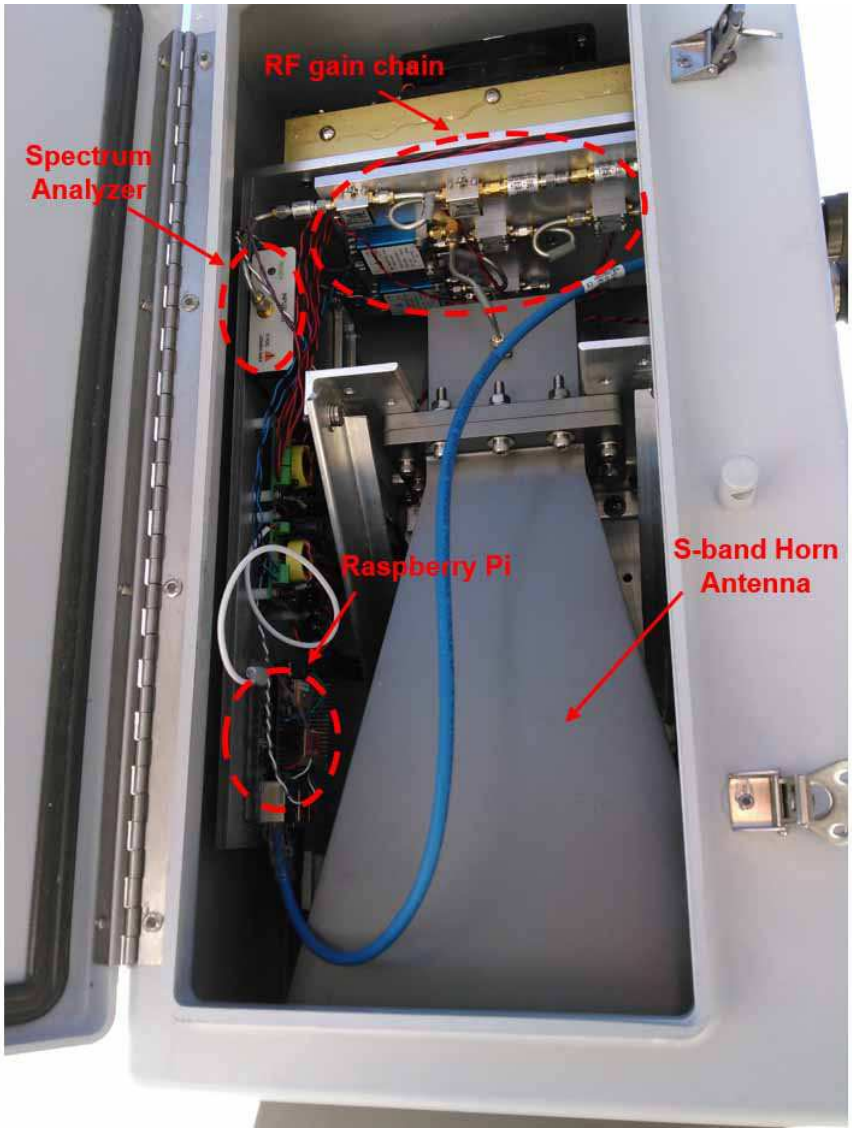

Figure 3.8: The S-band WiBAR system in frequency domain approach. The Signal Hound spectrum analyzer as well as the receiver gain chain is attached to a plate inside a box enclosure, and one side of the antenna in the box is also shown. This system was used for snowpack measurement and has been operational since Winter 2019.

Fourier transform of the power spectrum:

$$\Phi(\tau) = \int \hat{e}(f) w(f) \mathrm{e}^{-j2\pi f\tau} df \tag{3.4}$$

where $w(f)$ is an appropriate window function.

The autocorrelation function (ACF) separates the coherent effect, at $\tau = \tau_{delay}$, from the incoherent signal, at $\tau = 0$. Because our main measurement objective is to passively measure a time delay, and not a brightness amplitude, a number of traditional radiometry techniques have not been employed. In particular, we did not implement a thermal control system to stabilize the radiometer gain, despite the minutes-long integration times in total power mode. As such, our amplitude measurements contain additional noise that appears as incoherent signals at $\tau = 0$ and an increased noise floor at non-zero delays. We expect our measured delays to be quite accurate, however, because the spectrum analyzer maintains a stabilized frequency source.

The spectrum analyzer used in our measurements is a super-heterodyne receiver, in which the intermediate frequency (IF) filter is swept over the entire bandwidth. This filter is also called the resolution bandwidth (RBW) filter. The filtered signal then enters a square-law envelope detector. The output of the envelope detector is then fed to a low-pass filter with a bandwidth known as the video bandwidth (VBW). This filter provides a smoothed version of the detected signal. The ratio of the RBW to the VBW determines the noise floor in the measurements [6]. There are some parameters that should be set in the spectrum analyzer prior to data collection. These parameters are the center frequency, f_c, frequency span, F_s, number of frequencies, N_f, sweep time, T_s, resolution bandwidth, RBW, and video bandwidth, VBW. By employing a COTS spectrum analyzer, the selection of some of these parameters is limited by the hardware. For example, using the Agilent Spectrum Analyzer, our

maximum RBW is 3 MHz, and the number of frequencies is fixed at $N_f = 461$.

3.2.4 Single Layered Media

A single layer of ice or snow is shown in Fig. 2.1, and its emissivity was derived as given by (2.12). The coherent interference of rays traversing the slab different number of times gives rise to an emissivity spectrum that oscillates around a mean value, with local maxima at wavelengths of constructive interference, and minima at wavelengths of destructive interference.

3.2.4.1 Minimum and Maximum Detectable Time Delay

The lower limit of the sensed time delay depends on the WiBAR ability to distinguish an autocorrelation peak at τ_{delay} from the peak at $\tau = 0$. This lower limit depends on the requirement that $\tau_{delay} > \tau_c$, where τ_c is the radiometer correlation time, and is the half power width of the autocorrelation peak at $\tau = 0$, ie. $\Phi(\tau_c) = \frac{1}{2}\Phi(0)$. τ_c is inversely related to the WiBAR bandwidth F_s as given by [15]

$$\tau_c = \frac{\zeta}{F_s} \tag{3.5}$$

where ζ is a factor depending on the Fourier window $w(f)$ since the autocorrelation peak shape depends on the window function. For instance, ζ is equal to one for the rectangular window, while it is equal to 2 for the Hamming window, as the width of the main lobe of the Fourier transform of the Hamming window function is about twice that of the rectangular window function. As a case in point, the microwave propagation time delay τ_{delay} using equation (2.4) at an incidence angles of $\theta = 0°$, 15°, 30°, 45°, 60°, and 75° as function of icepack thickness $0 < d_{ice} < 2$m and index of refraction $n_{ice} = \sqrt{3.15}$ is shown in Fig. 3.9. Detecting minimum icepack thicknesses approaching 10 cm presents a challenge in that it requires resolving τ_{delay}

at autocorrelation lag times of around 1 ns from the spread of the peak at $\tau = 0$ due to τ_c. Thus, for this objective, the system's bandwidth from (3.5) should be greater than 1 GHz for the rectangular and 2 GHz for the Hamming window functions. This effect is shown in Fig. 3.10, where the 1 GHz ACF does not show the simulated delay at 1.18 ns at all, while the 2 GHz ACF does show a peak corresponding to this delay, albeit contaminated with the sidelobes of the peak at zero delay. Thus, the lower limit of the detectable time delay is approximately given by

$$\frac{\zeta}{F_s} < \tau_{delay} \tag{3.6}$$

Conversely, (3.6) determines the minimum WiBAR frequency span needed to measure a desired minimum pack thickness.

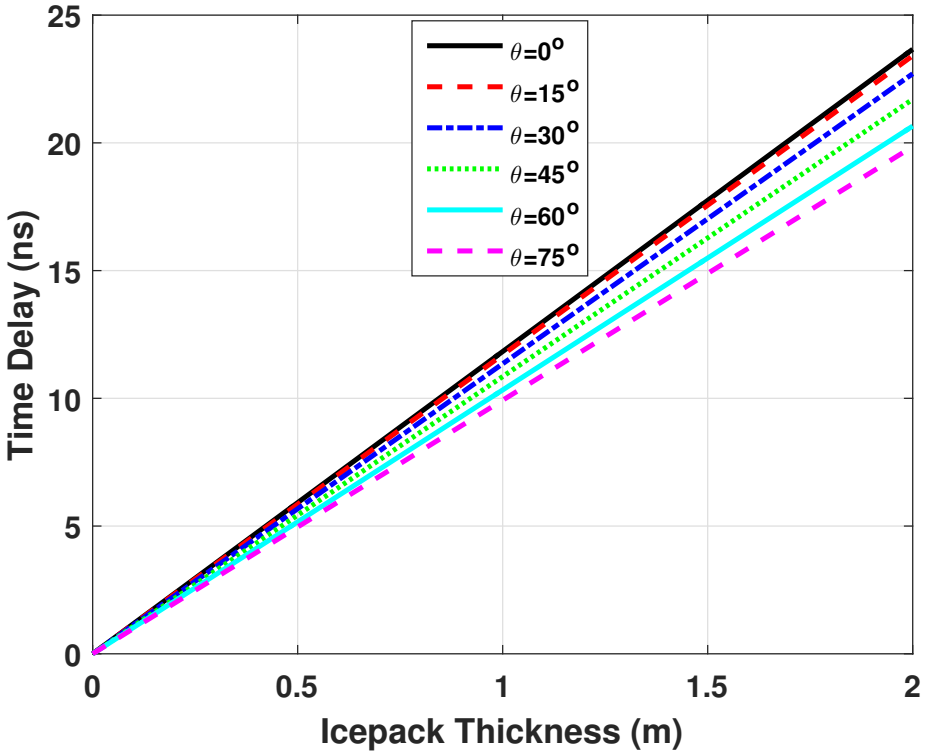

Figure 3.9: Simulated τ_{delay} as a function of icepack thickness with refractive index of $n_{ice} = \sqrt{3.15}$ over fresh water for six different incidence angles ($\theta = 0°$, 15°, 30°, 45°, 60°, and 75°).

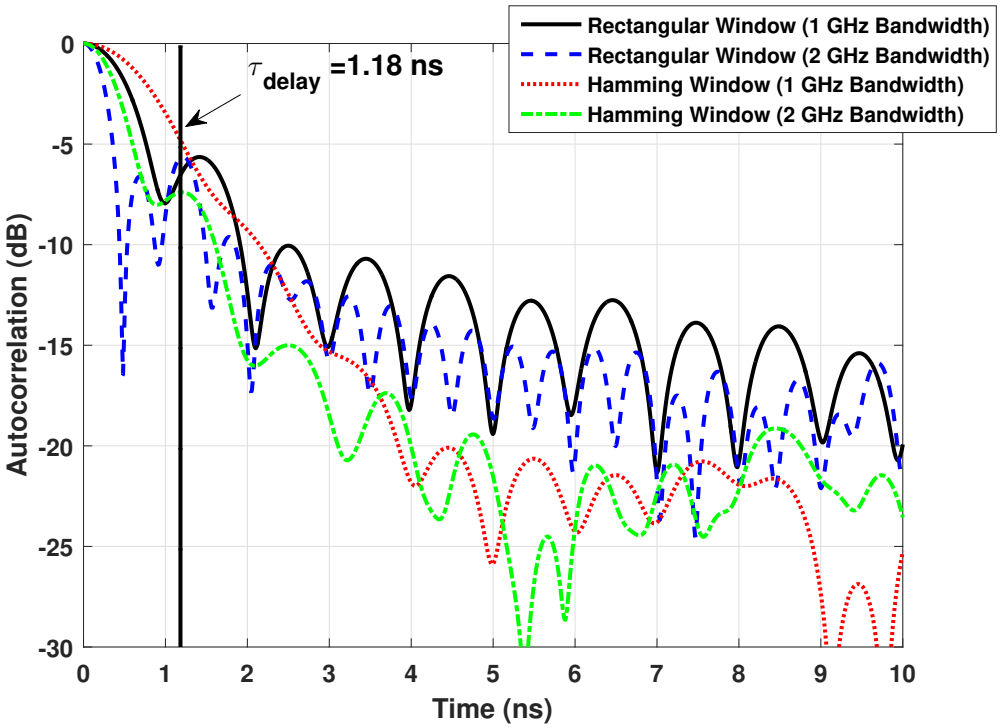

Figure 3.10: Simulated autocorrelation response of a 10 cm icepack using rectangular and Hamming window functions. The system's bandwidth should be greater than about 2 GHz in order to detect a 10 cm icepack using a Hamming window function, while a bandwidth greater than about 1 GHz should be used with a rectangular window function ($\theta = 0°$ and $\tau_{delay} = 1.18$ ns).

The upper limit of the sensed time delay is contingent upon rays that traverse the pack be not significantly absorbed or scattered. For example, it has been shown by experiment that 10 GHz rays would not be excessively absorbed or scattered by a 2 meter dry snowpack which had not undergone significant stratification or metamorphism [91]. A theoretical upper limit to the maximum detectable time delay is determined by the resolution bandwidth (RBW) of the spectrum analyzer and the number of frequency bins as given by equation (3.7). For instance, one can increase the upper limit by either increasing the number of frequency bins while the frequency span is fixed, or by decreasing the resolution bandwidth.

$$\tau_{delay} < \frac{1}{2}\min\left\{\frac{N_f}{F_s}, \frac{1}{\text{RBW}}\right\} \tag{3.7}$$

where N_f is the number of frequency bins. The transition between the two conditions occurs when adjacent frequency bins touch each other. For a custom WiBAR receiver, (3.7) can be used to determine the requirements for the instantaneous bandwidth and the number of frequency bins. When using a spectrum analyzer as a receiver, however, N_f is sufficiently high and RBW sufficiently small that the upper limit is dictated by the extinction in the pack.

Within these limits, the measurement of τ_{delay} can be made arbitrarily precise in post processing. While the resolution of the ACF created from N_f spectral points over F_s frequency span is $\frac{1}{F_s}$, the creation of the ACF from the emissivity spectrum can be performed with zero-padding of the spectrum, increasing the precision of the ACF in the time-domain to $\cdot\frac{N_f}{F_s\ (N_f+N_z)}$, where N_z is the number of zeros added to the spectrum prior to its inverse Fourier transform. The radiometer correlation time does, however, limit the ability of the WiBAR technique to resolve multiple interfaces. This topic, however, is further discussed in Section 3.2.5.1.

3.2.4.2 Autocorrelation Function Expectation

In this section, we first look at the emissivity of a single layer of snow or ice pack, and the case of a presence of another layer, such as presence of a snow layer on an icepack, will be further discussed in final thesis. By considering the typical values for the reflection coefficients of ice and dry snow layers, the denominator in (2.12) is very close to unity and can be approximated by its Taylor expansion around one:

$$e(f) \approx \overline{e}\big(1 - 2A_e \cos(2\pi f \tau_{delay})\big) \tag{3.8}$$

where $\overline{e}$ is the mean emissivity over frequency, A_e is one half of the amplitude of the ripple in the emissivity as a function of frequency, and $2k_{1z}d$ is substituted with $2\pi f \tau_{delay}$ to emphasize the frequency dependence. It is assumed that the calibration

(3.3) produces an emissivity with features faithful to (2.1). The n th order term of the Taylor expansion captures the delay of $n\tau_{delay}$, and so as long as $\tau_{delay} > \tau_c$, (3.8) is sufficient for unambiguous measurement of the delay. Explicitly, the mean emissivity and the ripple amplitude are given by

$$\overline{e} = \frac{(1-|R_{01}|^2)(1-|R_{12}|^2)}{1+(|R_{01}|\,|R_{12}|)^2} \tag{3.9a}$$

$$A_e = \frac{R_{01}R_{12}}{1+(|R_{01}|\,|R_{12}|)^2} \tag{3.9b}$$

where the volume extinction has been assumed negligible. As an example, for ice over water and $\theta = 0°$, $\overline{e} = 0.490$ and $A_e = 0.181$. When absorption and scattering are included, the form of (3.8) will be still applicable, but (3.9) will need to be modified to incorporate such effects. Thus, we will continue the analysis with $\bar{e}$ and A_e rather than with reflection coefficients. In the presence of multiple layers, the Taylor expansion (3.8) will become more complicated in a way that there will be more cosine terms due to the coherent interference introduced by the new boundaries.

With the simplification (3.8), the expected value of the ACF is

$$E\left[\Phi(\tau)\right] = \overline{e}\int_{f_c-F_s/2}^{f_c+F_s/2} w(f)\mathrm{e}^{-j2\pi f\tau}\Big(1-2A_e\cos(2\pi f\tau_{delay})\Big)df \tag{3.10}$$

The only dependency on the frequency, f, will be through the $\cos(2\pi f\tau_{delay})$ and $w(f)$ terms since R_{01} and R_{12} are approximately constant with respect to frequency. Therefore, the expected value is given by

$$E\left[\Phi(\tau)\right] = \overline{e}F_s\mathrm{e}^{-j2\pi f_c\tau}\Bigg\{W_1(\tau) - A_e\Big[\mathrm{e}^{j2\pi f_c\tau_{delay}}W_1(\tau-\tau_{delay}) + \mathrm{e}^{-j2\pi f_c\tau_{delay}}W_1(\tau+\tau_{delay})\Big]\Bigg\} \tag{3.11}$$

where $W_n(\tau)$ is the impulse response of the nth power of the window function, and is given by

$$W_n(\tau) = \frac{1}{F_s} \int_{f_c - F_s/2}^{f_c + F_s/2} w^n(f) \mathrm{e}^{-j2\pi(f-f_c)\tau} df \tag{3.12}$$

Considering only the positive time delays, it can be observed from (3.11) that the local maxima of the expected value of autocorrelation response are at specific values of $\tau = 0$ and $\tau = \tau_{delay}$. For a rectangular window, $w(f)$ will be constant and equal to one in the frequency range of operation, and its impulse response is given by

$$W_1(\tau) = \mathrm{sinc}(F_s\tau) \tag{3.13}$$

where $\mathrm{sinc}(x) = \sin(\pi x)/\pi x$.

As a typical alternative, a cosine window can be used instead of a rectangular window. In this case, the frequency response, $w(f)$, and the impulse response, $W_1(\tau)$, of the window function are given by

$$w(f) = \begin{cases} \alpha + (1-\alpha)\cos(\frac{2\pi}{F_s}(f - f_c)), & f_c - \frac{F_s}{2} \leq f \leq f_c + \frac{F_s}{2} \\ 0, & \text{otherwise} \end{cases} \tag{3.14}$$

$$W_1(\tau) = \left\{ \alpha\ \mathrm{sinc}(F_s\tau) + \left(\frac{1-\alpha}{2}\right) \left[\mathrm{sinc}(1 - F_s\tau) + \mathrm{sinc}(1 + F_s\tau)\right] \right\} \tag{3.15}$$

where $\alpha = 0.54$ is for the Hamming window, $\alpha = 0.5$ is for the Hann window, and $\alpha = 1$ is for the rectangular window. The benefit of this cosine tapered window function is lower side-lobes; in fact, the first side lobe level (SLL) of the Hamming window is about 21 dB down from the main lobe peak while it is only 6.5 dB down from the main lobe peak in the rectangular window. The price for this benefit is that

the main lobe is roughly twice as wide as the rectangular window. These effects can be observed in Fig. 3.11, where the expected value of the autocorrelation response of 36.8 cm lake icepack over freshwater is shown using the rectangular and Hamming window functions.

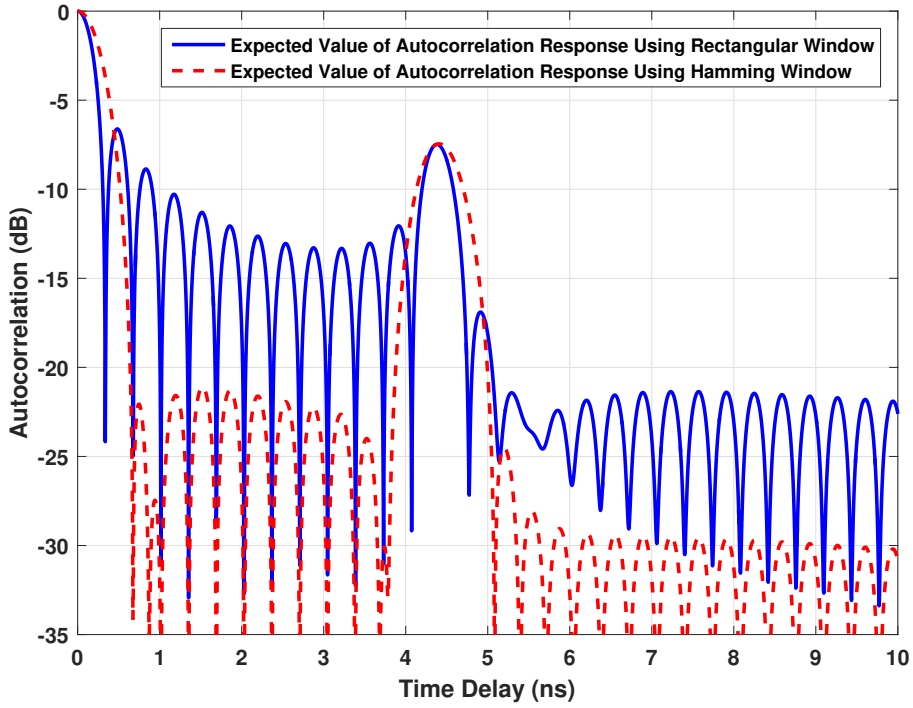

Figure 3.11: The expected value of the autocorrelation response using rectangular (solid blue line) and Hamming (dashed red line) window function as a function of time delay ($\theta = 0°$, $d_{ice} = 36.8$ cm, and $\tau_{delay} = 4.35$ ns).

3.2.4.3 Measurement Uncertainty

This instrument resembles a total power radiometer, for which the noise level can be given by [90]

$$\left(\frac{\Delta P}{P}\right)^2 = \left(\frac{\Delta T}{T_{SYS}}\right)^2 = \frac{1}{B\tau'} + \left(\frac{\Delta G}{G}\right)^2 \tag{3.16}$$

where ΔG, ΔP and ΔT are the standard deviations of the radiometer's gain, power and brightness temperature, and τ' is the integration time. While WiBAR does not measure brightness, but rather a time delay, this noise impacts the ability to observe the delay, which is explained in this and the next two subsections.

In the WiBAR, we use a spectrum analyzer for the receiver back-end, and do not use thermal control on the RF electronics. The lack of thermal control makes the gain variations typically slow relative to the spectrum analyzer sweep time. As a result, ΔG is a minimal contribution to random errors of the calibrated emissivity, while it does contribute substantially to the systematic errors that apply to the entire spectrum. Indeed, we have sometimes seen calibrated emissivities exceeding unity, but the random variations, manifest as noise in adjacent frequencies in the emissivity spectra, are dominated by the time-bandwidth product. We now look at the time-bandwidth product applied to WiBAR.

The spectrum analyzer resolution bandwidth is the 3dB bandwidth of the spectrum analyzer's IF bandpass filter, and determines the noise bandwidth, B. As the spectrum analyzer employs a Gaussian filter for the resolution bandwidth, $B = \frac{1}{2}\sqrt{\frac{\pi}{\ln 2}}$ RBW ≈ 1.06 RBW. The time that the spectrum analyzer spends in each RBW is τ'. Hence, τ' would be equal to $\frac{T_s \text{RBW}}{F_s}$. In a spectrum analyzer, the sweep time, T_s, is determined by the RBW, VBW, and the frequency span, F_s, as given by

$$T_s = \frac{\kappa F_s}{\text{RBW} \times \text{VBW}} \tag{3.17}$$

where κ is a dimensionless proportionality constant, and it is in the 2 to 3 range for the synchronously-tuned, and near-Gaussian filters [1]. Equation (3.17) is valid when VBW $<$ RBW.

Therefore, neglecting the systematic errors that only impact $\bar{e}$ and focusing on

the random errors that will impact A_e, (3.16) is simplified to (3.18).

$$\frac{\Delta P}{P} = \frac{\Delta T}{T_{SYS}} = \frac{1}{\sqrt{1.06\kappa \frac{\text{RBW}}{\text{VBW}}}} \tag{3.18}$$

In our measurements which we have done in Winter 2016, RBW = 3 MHz, VBW = 1 kHz, $F_s = 3$ GHz, and the resulting sweep time was $T_s = 2.9641$ s. Therefore, using (3.17), κ is 2.96, and using (3.18), the sensitivity of a single sweep of the radiometer is -19.88 dB (1.03%). Sometimes, one sweep of the spectrum analyzer is not enough to keep the measurement uncertainty sufficiently small. In situations where we employ N_{trace} sweeps of a single target averaged together, the total number of effective samples, N_{ind}, at each frequency is given by the product of the number of sweeps and the time-bandwidth product: $N_{ind} = \kappa N_{trace}\text{RBW/VBW}$.

3.2.4.4 Autocorrelation Function (ACF) Variance

The variance of the autocorrelation response is needed to determine the likelihood of measuring the delay associated with the snow or ice pack.

$$Var[\Phi(\tau)] = \int_{f_c - F_s/2}^{f_c + F_s/2} \int_{f_c - F_s/2}^{f_c + F_s/2} Cov[e(f), e(f')] w(f) w(f') \exp\left(-j2\pi(f - f')\tau\right) df df' \tag{3.19}$$

Since we measured the emissivity at each frequency by sweeping over each RBW in time, $e(f)$ and $e(f')$ are independent and uncorrelated. Therefore, $Cov[e(f), e(f')]$ would be zero unless $f = f'$, where it is equal to the $Var[e(f)]$. Therefore, (3.19) can be simplified to (3.20).

$$Var[\Phi(\tau)] = \text{RBW} \int_{f_c - F_s/2}^{f_c + F_s/2} Var[e(f)] w^2(f) df \approx \text{RBW}\ F_s\ Var[e(f)]\ W_2(0) \tag{3.20}$$

The approximation is because $A_e \ll \overline{e}$, ie. the variance of the emissivity is approximately independent of the frequency. As a consequence, the variance of the ACF is also independent of τ and τ_{delay} in the case of a slab target. For the cosine windows considered here, $W_2(0) = (\alpha^2 + (1-\alpha)^2/2)$. Specifically, $W_2(0) = 1$ for the rectangular window, 0.3972 for the Hamming window, and 0.375 for the Hann window.

However, the variance of the emissivity depends on the number of samples measured, and how these measurements are used. Using a standard error analysis [7] on the calibration equation (3.3), it can be shown that the variance of the emissivity ($Var[e]$) is related to its expected value ($E[e]$) as given by (3.21).

$$Var[e(f)] = \frac{(E[e])^2}{N_{ind}} \left[\frac{\begin{array}{r}(T_{Bp}+T_{REC})^2(T_{Ba}-T_{Bs})^2 + (T_{Ba}+T_{REC})^2(T_{Bp}-T_{Bs})^2 \\ + (T_{Bs}+T_{REC})^2(T_{Ba}-T_{Bp})^2\end{array}}{(T_{Bp}-T_{Bs})^2(T_{Ba}-T_{Bs})^2} \right] \tag{3.21}$$

where T_{Bp}, T_{Bs}, and T_{Ba} are the brightness temperature of the ice/snow pack, sky, and the microwave absorber, respectively. Since the microwave absorber, the pack, and the radiometer have been in the same environment for enough time to be at an equilibrium temperature, T_0, we will simplify (3.21) with $T_{REC} \approx T_0(F-1)$, $T_{Bs} \approx 0$, $T_{Bp} \approx eT_0$, and $T_{Ba} \approx T_0$, where F is the noise figure of the radiometer. Hence,

$$Var[e(f)] \approx \frac{(\overline{e}+F-1)^2 + (\overline{e}-1)^2(F-1)^2 + \overline{e}^2F^2}{N_{ind}} \tag{3.22}$$

For an icepack or snowpack with some surface roughness, the emissivity is quite high, approaching 1. When $\overline{e} \approx 1$, $Var[e(f)]$ is maximized over $\overline{e}$, and thus $\overline{e} = 1$ corresponds to a worst case variance. For these reasons, we will assume $\overline{e} = 1$, and

(3.22) and (3.20) are simplified to

$$Var[e(f)] \approx \frac{2F^2}{N_{ind}} \tag{3.23}$$

$$Var[\Phi(\tau)] = \frac{2W_2\,(0)\,F^2\ \text{RBW}\ F_s}{N_{ind}} \tag{3.24}$$

On the other hand, in the absence of an icepack, the mean of the emissivity of freshwater would be quite low, but roughness is very likely; therefore, we can also use the worst case scenario of the $Var[e(f)]$ in this case, and the variance of the emissivity and its autocorrelation response are the same as (3.23) and (3.24), respectively. Moreover, in the absence of a snowpack, the mean of the emissivity of land would be quite high, $e \approx 1$, and the variance of the emissivity and its autocorrelation response, using the worst case of the $Var[e(f)]$, are again the same as equations (3.23) and (3.24), respectively. Thus, because it is representative and a worst-case, we will use (3.24) regardless of the target in the following analyses.

3.2.4.5 Limits of Detection

Provided that the number of independent samples N_{ind} is sufficiently high, the central limit theorem will apply and the distribution of $\Phi(\tau)$ will be Gaussian. Under these conditions, if the absolute value of the expected value plus a constant (Z_{FA}) times the standard deviation of the autocorrelation response in the absence of a pack is less than the absolute value of the expected value minus a constant (Z_{PD}) times the standard deviation of the autocorrelation response in the presence of a pack, as given by (3.25), the technique will be able to detect a delay peak.

$$|E[\Phi_{absence}(\tau)]| + Z_{FA}\sqrt{Var[\Phi_{absence}(\tau)]} < |E[\Phi_{presence}(\tau)]| - Z_{PD}\sqrt{Var[\Phi_{presence}(\tau)]} \tag{3.25}$$

The Z parameters determine the False Alarm Rate (FAR) and Probability of Detection (PD) as given by [9].

$$\text{FAR} = \frac{1}{2}\Big(1 - \text{erf}(Z_{FA}/\sqrt{2})\Big) \tag{3.26a}$$

$$\text{PD} = \frac{1}{2}\Big(1 + \text{erf}(Z_{PD}/\sqrt{2})\Big) \tag{3.26b}$$

where erf(Z) is the error function encountered in integrating the normal distribution, as given by

$$\text{erf}(Z) = \frac{2}{\sqrt{\pi}} \int_0^Z \text{e}^{-t^2} dt \tag{3.27}$$

For example, the FAR will be about 2.2% and 15.8% for $Z_{FA} = 2$ and $Z_{FA} = 1$, respectively. Higher Z_{FA} or Z_{PD} will result in better performance, and the system parameters need to be designed so as to provide sufficient number of independent samples. Below, the effect of the number of independent samples with fixed Z parameters in time delay detection is shown. In addition, using the expected value and variance of the autocorrelation function derived in Sections 3.2.4.2 and 3.2.4.4, respectively, along with (3.25), the minimum number of required independent samples N_{ind} for lake icepack and dry snowpack detection is derived.

The FAR in (3.26a) is that of detecting a single peak at a single delay time, but we need to keep the FAR down throughout the autocorrelation response in a region from τ_{min} to τ_{max}, where these are the minimum and maximum detectable time delays of interest bounded by (3.6) and (3.7), respectively. Without zero-padding the spectrum for enhanced resolution, the number of time bins in which a peak could occur is given by $n_\tau = F_s\ (\tau_{max} - \tau_{min})$. This result is not affected by zero padding: while the temporal precision is improved, there is no additional information. Since the FAR for detecting a peak at each time bin is independent of other time bins, the FAR for all

τ in (τ_{min}, τ_{max}) are related to the FAR for a single τ, as given by (3.28).

$$1 - \text{FAR(for all } \tau \text{ in } (\tau_{min}, \tau_{max})) = \Big(1 - \text{FAR(for one } \tau)\Big)^{n_\tau} \tag{3.28}$$

Since we want to keep the FAR small, we can assume Z_{FA} will be selected such that FAR $\ll 1$. Hence, (3.28) can be simplified to (3.29).

$$\begin{aligned} &\text{FAR(for all } \tau \text{ in } (\tau_{min}, \tau_{max})) = n_\tau \text{FAR(for one } \tau) \\ &= \frac{F_s(\tau_{max} - \tau_{min})}{2}\Big(1 - \text{erf}(Z_{FA}/\sqrt{2})\Big) \end{aligned} \tag{3.29}$$

For example, if we have $F_s = 1$ GHz, and we expect τ_{delay} to be in the range of 1 ns to 11 ns, then $n_\tau = 10$, and with $Z_{FA} = 4$, FAR(for one τ)=0.0032%, and FAR(for all τ in (1 ns,10 ns))=0.032%.

In the presence of a pack, where $\tau_{delay} > \tau_c$, the magnitude of the expected value of the peak of the autocorrelation response is given by

$$|E[\Phi_{presence}(\tau)]| = |A_e|\,\overline{e}\; F_s\; W_1(0) \tag{3.30}$$

where we assume that the peak rises above the level of the surrounding noise floor.

A number of situations constitute the absence of the pack. In all of these situations, the expected value of the autocorrelation function is determined by the noise floor of the ACF. We will denote this ACF noise floor, relative to the peak at $\tau = 0$, as SNR_Φ. Especially for small pack thicknesses, this floor may be the sidelobes of the window function applied to the incoherent emissivity of the scene, so that $\text{SNR}_\Phi \geq \text{SLL}$. In any event, the expected value in the absence of the pack is

$$|E[\Phi_{absence}(\tau)]| = \text{SNR}_\Phi\; e_{absence}\; F_s\; W_1(0) \tag{3.31}$$

For example, if the pack is not present and the underlying surface is smooth, $e_{absence} = 1 - |R_{02}|^2$, where R_{02} is the Fresnel reflection coefficient between air and water, or air and land. For the purpose of unambiguous measurement of the delay, however, the most relevant absence is the case where the pack is present, but $|\tau - \tau_{delay}| > \tau_c$. In other words, to detect the pack time delay, the delayed peak must rise above the surrounding floor of the autocorrelation function. In this case, $e_{absence} = \overline{e}$. The autocorrelation response of the lake icepack with thickness $d_{ice} = 36.8$ cm, the expected value ($E[\Phi_{absence}(\tau)]$), the expected value plus one standard deviation ($|E[\Phi_{absence}(\tau)]| + \sqrt{Var[\Phi_{absence}(\tau)]}$), and the expected value plus two standard deviations ($|E[\Phi_{absence}(\tau)]| + 2 \times \sqrt{Var[\Phi_{absence}(\tau)]}$) of the autocorrelation response in the absence of the pack using rectangular and Hamming window functions are shown in Figs. 3.12 and 3.13, respectively. The number of independent samples, N_{ind}, in these figures is 100. It can be observed that there is one peak after the zero delay peak. This peak, which is higher than the summation of the expected value and the standard deviation at any single point of time, is considered a detected peak, and it corresponds to the microwave propagation time within the icepack. It can also be observed that the side lobe levels have been decreased in Fig. 3.13 due to the Hamming window function. On other hand, if we decrease N_{ind} to 5, it will get harder to detect a peak, as it can be observed in Fig. 3.14. The Hamming window function is used in Fig. 3.14.

Using equations (3.24), (3.30), and (3.31), equation (3.25) for lake icepack and dry snowpack can be written to show the dependence of the minimum number of independent samples N_{ind} on the receiver operating characteristics, noise figure, and detection scenario as

$$N_{ind} = \frac{\kappa N_{trace} \mathrm{RBW}}{\mathrm{VBW}} > 2 \frac{(Z_{FA} + Z_{PD})^2}{N_f} \cdot D^2(\theta) \cdot F^2 \tag{3.32}$$

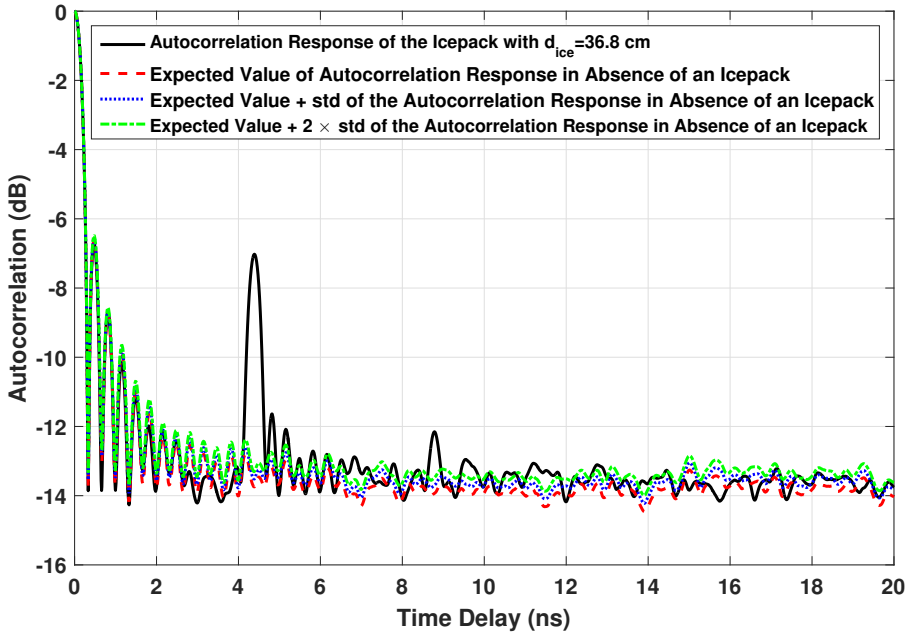

Figure 3.12: Simulation of the autocorrelation response of a lake icepack over freshwater ($\theta = 0°$ and $d_{ice} = 36.8$ cm). The expected value, the expected value plus one standard deviation, and the expected value plus two standard deviations of the autocorrelation response in the absence of an icepack are also simulated. $F_s = 3$ GHz, and the number of independent samples, N_{ind} is 100. The rectangular window was used.

where $D(\theta)$ is a discrimination function which depends only on the detection scenario (lake icepack or snowpack), the window function, and the incidence angle, as given by

$$D\left(\theta\right) = \left(\frac{\sqrt{W_2(0)}}{W_1(0)}\right) \Big/ \left(\left|A_e\right| \overline{e} - \mathrm{SNR}_{\Phi} e_{absence} \right) \tag{3.33}$$

Neither (3.32) nor (3.33) depends on the pack depth or τ_{delay} due to our assumption that $A_e \ll \overline{e}$.

Equation (3.32) is valid only when $D(\theta) > 0$, i.e., when the delayed peak rises above the autocorrelation noise floor. The square of the positive values of this discrimination function for lake icepack and dry snowpack is shown in Fig. 3.15(a) and Fig. 3.15(b), respectively, assuming that $\mathrm{SNR}_{\Phi} = \mathrm{SLL}$. In both figures, $D^2(\theta)$ is

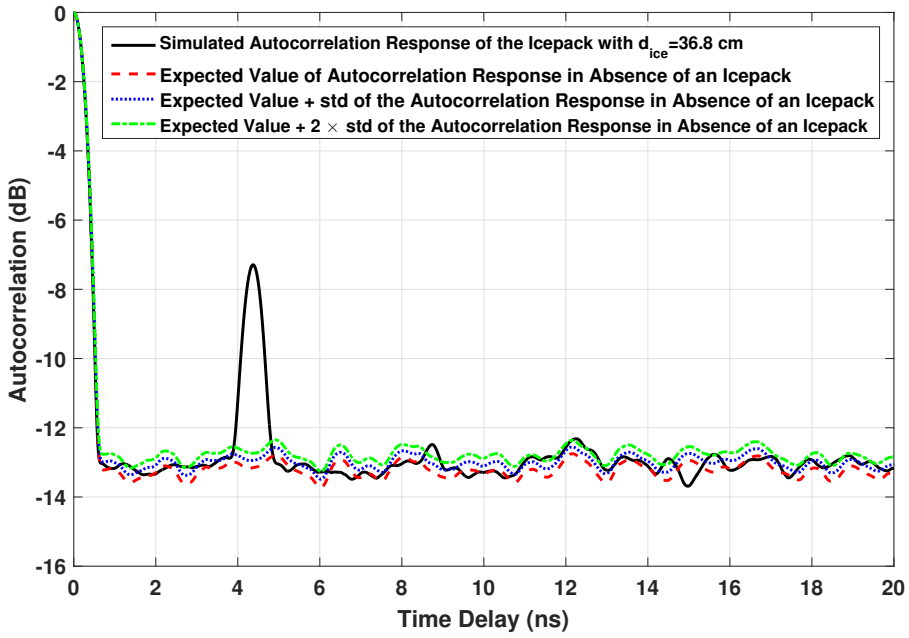

Figure 3.13: Simulation of the autocorrelation response of a lake icepack freshwater ($\theta = 0°$, $d_{ice} = 36.8$ cm, and $\tau_{delay} = 4.35$ ns). The expected value, the expected value plus one standard deviation, and the expected value plus two standard deviations of the autocorrelation response in the absence of an icepack are also simulated. $F_s = 3$ GHz, and the number of independent samples, N_{ind} is 100. The Hamming window was used.

shown in both H and V polarization and for both rectangular and Hamming windows. For the snowpack we used $\rho_s = 0.3$ g/cm^3; hence, the refractive index of the snowpack is $n_{snow} = 1.253$, using (2.6). The typical value of frozen soil is $n_{soil} = 2 - j0.05$.

It can be observed from these figures that the number of independent samples, N_{ind}, needed to detect τ_{delay} for both lake icepack and dry snowpack is lower in H-pol configuration compared to the V-pol configuration regardless of the window function. Moreover, we are only able to detect the time delay at few angles in V-pol configuration due to the Brewster angle between the air and icepack while we can detect the time delay at nearly all incidence angles in H-pol regardless of the window function. The choice of the Hamming window function in post processing is also superior to the rectangular window with respect to N_{ind} for both lake icepack and dry snowpack regardless of the polarization. Finally, Fig. 3.15 predicts that the

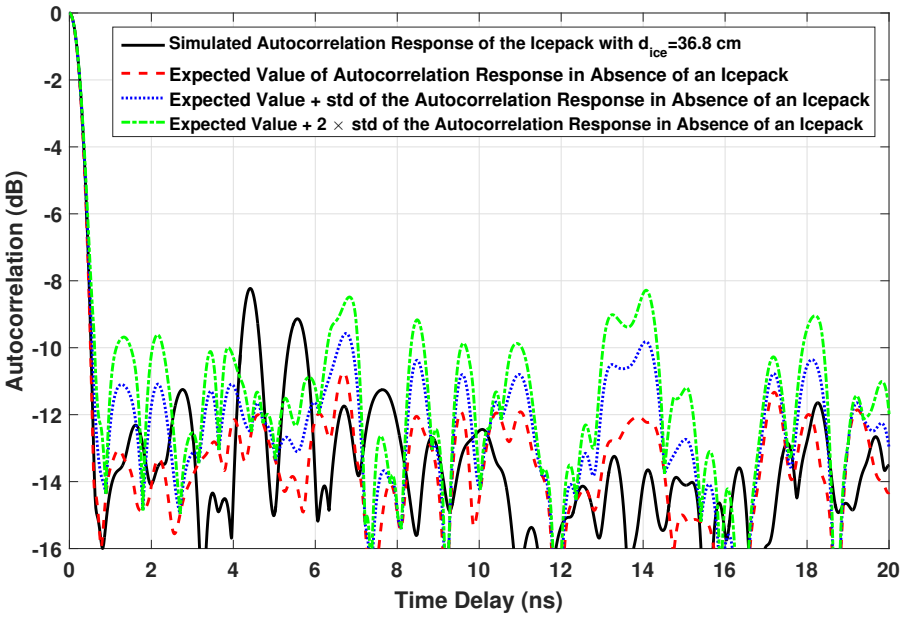

Figure 3.14: Simulation of the autocorrelation response of a lake icepack ($\theta = 0°$, $d_{ice} = 36.8$ cm, and $\tau_{delay} = 4.35$ ns). The expected value, the expected value plus one standard deviation, and the expected value plus two standard deviations of the autocorrelation response in the absence of an icepack are also simulated. $F_s = 3$ GHz, and the number of independent samples, N_{ind} is 5. The Hamming window was used.

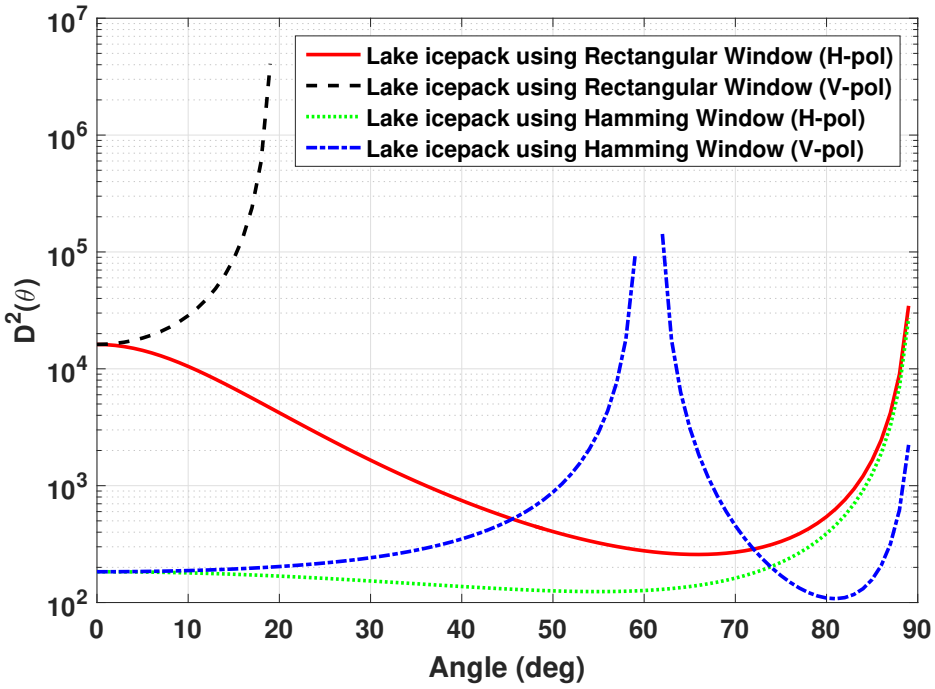

(a)

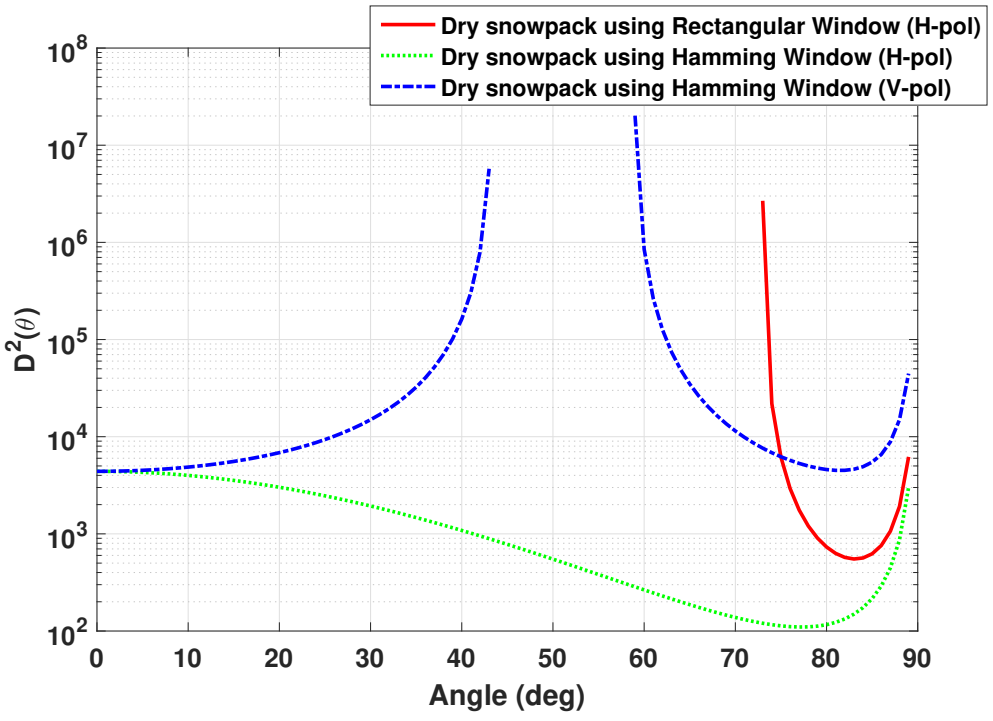

(b)

Figure 3.15: The square of the positive values of the discrimination function $D(\theta)$ given by (3.33) for (a) lake icepack and (b) dry snowpack as a function of incidence angle.

microwave propagation times in both lake icepack and dry snowpack are detectable at angles away from nadir to close to grazing with the appropriate choice of polarization and window function.

As an example, for a lake icepack, $N_{ind} = 3 \times 10^5$ satisfies (3.32) with $(\tau_{max} - \tau_{min})$ = 10 ns, F_s = 3 GHz, $Z = 3$ (FAR(for all τ) = 4.05%), RBW = 3 MHz, VBW = 1 KHz, $N_f = 461$, $N_{trace} = 100$, and $F = 10$ dB using both rectangular and Hamming window functions at 10° incidence angle for both H- and V-pol configurations.

3.2.4.6 Effect of Antenna Elevation Beamwidth

Thus far we have assumed a pencil-beam antenna (ie. a hypothetical antenna with infinitesimal beamwidth) is used to observe the delay. However, the delay as given by (2.4) has an incidence angle dependence, and thus any real antenna with elevation beamwidth will smear the delay in the time domain via a process akin to frequency dispersion. For simplicity, we will assume a 2D problem (the plane of incidence) and that the overall gain pattern for the antenna can be modelled as a product of an elevation pattern and an azimuth pattern. This assumption about the gain pattern is often used for the analysis of standard gain horns (eg. [90]). Also, since we assume that the calibration targets used to implement (3.3) will be beamfilling, the measured emissivity spectra at boresight angle θ_0 will be equivalent to

$$e_m(f, \theta_0) = \frac{1}{\beta_e} \int e(f, \theta) g(\theta; \theta_0) d\theta \tag{3.34}$$

where $\beta_e = \int g(\theta; \theta_0) d\theta$ is the elevation beamwidth and $g(\theta; \theta_0)$ is the elevation antenna gain in the direction θ when the antenna boresight is θ_0. Presuming that the elevation gain pattern is symmetric around boresight, the mean emissivity, $\overline{e}$, is unchanged, but the amplitude of the ripples in the observed emissivity spectra are reduced.

If we can assume the beam pattern is approximately independent of frequency, and since the inverse Fourier transform is a linear operation, we can further say that

$$\Phi_m(\tau) = \frac{1}{\beta_e} \int \Phi(\tau)\, g(\theta;\theta_0) d\theta \tag{3.35}$$

where the dependence of Φ on the local incidence angle θ is through τ_{delay}.

In the previous section we have shown that H-pol (TE) is preferred over V-pol (TM) because the reflection coefficients that create the delayed ray are larger, resulting in fewer samples needed to extract the delayed peak in the autocorrelation function from the noise floor. As our system utilizes a standard gain horn for the measurements, we can model the elevation gain pattern as done in [90]:

$$g_{e,H} = \left| \frac{\cos u_H}{1 - \left(\frac{2}{\pi} u_H\right)^2} \right|^2 \tag{3.36}$$

$$g_{e,V} = \left|\text{sinc } u_V\right|^2 \tag{3.37}$$

where $u_q = (\pi a_q/\lambda)\sin(\theta - \theta_0)$, λ is the wavelength, and a_q is the standard gain horn aperture dimension for the H-plane ($q = H$) and E-plane ($q = V$), respectively. The half-power beamwidths for these gain patterns are $\beta_H = 1.20\lambda/a_H$ and $\beta_V = 0.88\lambda/a_V$.

The effects of these beamwidths on the magnitude of the delayed peak are shown in Fig. 3.16 by directly convolving these antenna patterns with the autocorrlation function per (3.35). The reduction is most severe near $\theta_0 = 45°$ because that is where the magnitude of $d\tau_{delay}/d\theta$ is the largest, while it approaches zero at both nadir and grazing. Thus, downward looking WiBAR and possibly side-looking WiBAR may be more practical than one that looks at more traditional radiometer angles around 40°. A beamwidth of $\beta_e = 8.7°$ was chosen for Fig. 3.16 because it corresponds to measurements that will be discussed in the next section.

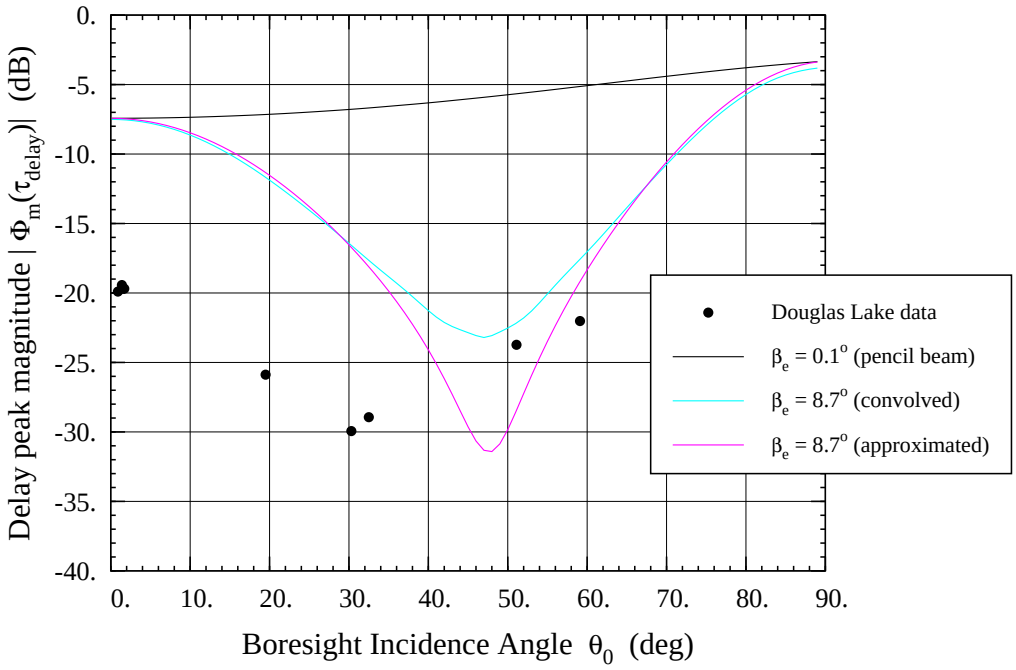

Figure 3.16: The effect of the antenna elevation beamwidth on the magnitude of the delayed peak, relative to the peak at zero lag, for H-pol and as a function of incidence angle for freshwater ice 36.8 cm thick. The curves for the pencil beam is from equation (3.30), convolved employs a numerical analysis of (3.35), and the approximation employs (3.39).

To see the effect of the frequency dependence of the antenna pattern, Fig. 3.16 also includes an approximate analytical expression that can be derived by expanding the square root in (2.4) in a Taylor series around θ_0, retaining zeroth order everywhere except in the complex exponential in (3.11), where it is retained to first order, approximating the gain pattern with

$$g_e\left(\theta;\theta_0\right) \approx \cos^2\left(\frac{\pi}{2\beta_e}\left(\theta-\theta_0\right)\right) \tag{3.38}$$

and integrating between the first nulls on either side of the main lobe. The result is that the ACF delayed peak is reduced by a factor of

$$L_\beta = \frac{\operatorname{sinc}\,\chi}{1-\chi^2} \tag{3.39}$$

where

$$\chi = -2\beta_e \; f \; \frac{d\tau_{delay}}{d\theta} \tag{3.40}$$

Since β_e is proportional to the ratio of wavelength to aperture size, χ is approximately constant across the spectrum, and proportional to the ratio of pack thickness to antenna elevation aperture. Thus, the discrimination function (3.33) becomes

$$D\left(\theta_0\right) = \left(\frac{\sqrt{W_2(0)}}{W_1(0)}\right) \Big/ \left(|A_e| \, \overline{e} L_\beta - \mathrm{SNR}_\Phi e_{absence} \right) \tag{3.41}$$

and now also includes dependence on the pack thickness and the antenna. As seen in Fig. 3.16, the analytical approximation using L_β underestimates the peak magnitude where the magnitude is reduced the most, relative to the more complete integral expression given by (3.35). Thus, the results using (3.39) are a conservative approximation for the beamwidth effects.

We can derive a requirement on the antenna aperture size by inserting the H-pol beamwidth $\beta_{e,H} = 1.20\lambda/a_H$ into χ, expanding the sinc function, and maintaining the requirement that $D(\theta) > 0$:

$$a_H > 1.20 \; d \; \sin 2\theta_0 \sqrt{\frac{|A_e| \, \overline{e}}{|A_e| \, \overline{e} - \mathrm{SNR}_\Phi e_{absence}} \cdot \frac{2\left(\pi^2/6 - 1\right)}{n_p^2 - \sin^2 \theta_0}} \tag{3.42}$$

For strong signals ($A_e \overline{e} > \mathrm{SNR}_\Phi e_{absence}$) from an ice pack ($n_{ice}^2 = 3.15$), the radical evaluates to close to unity. For 0.3 g/cm^3 snow pack, it is about 50% larger. Due to the $\sin 2\theta_0$ term, measurements at $\theta_0 = 45°$ appear to require the largest aperture, approximately the size of the pack thickness, with less stringent requirements at incidence angles both larger and smaller. Fortunately, much smaller antennas will suffice for measurements closer to nadir or to grazing than 45°. These conclusions about the antenna apply regardless of the center frequency, f_c, and the frequency

span, F_s, chosen for observation since the frequency dependent angular dispersion for τ_{delay} is corrected by the frequency dependence of the gain pattern of the antenna. Of course, the choice of F_s impacts the minimum measurable depth, and the choice of f_c will affect the amount of scattering seen.

3.2.5 Two Layered Media

Wideband autocorrelation radiometry (WiBAR) of single layer of ice over water has been previously discussed and investigated in Section 3.2.4 [57]. In this section, we want to investigate the ability of the WiBAR instrument in detecting the snow and ice layers in a two layered media of lake icepack with dry snow cover, which introduces another multipath interference. The measurement uncertainty and the effect of the antenna elevation beamwidth are the same as Sections 3.2.4.3 and 3.2.4.6. The variance of the ACF is the same as (3.24). The mean of the ACF is also similar to Section 3.2.4.2 since both the IFFT and expected value expressions are linear.

3.2.5.1 Resolving the Time Delays of the Snow and Ice Layers

For two equal amplitude delay peaks in time, τ_1 and τ_2, the classic criterion for the resolution is the width of the window at the half power points, as explained in [57],[30]. However, since the amplitudes of the two delay peaks of ice and snow are not equal, this criteria to resolve two equal amplitude peaks is not accurate. An alternative criteria is to resolve two unequal amplitude delay peaks with an amplitude difference, $|\Delta A|$. If the weak amplitude delay peak resides after the first side lobe level of the strong amplitude delay peak, in order to resolve the two peaks, the time difference between the two delay peaks $|\Delta\tau|$ should satisfy

$$|\Delta\tau| > \max\left\{\frac{\tau_{\text{main lobe}}}{2}, \left(\tau_{\text{FSLL}} \times 2^{\left(\frac{|\Delta A|-|\text{FSLL}|}{|\text{SLF}|}\right)}\right)\right\}, \tag{3.43}$$

where SLF (dB/Octave) is the side lobe fall-off (SLF) of the window function,FSLL (dB) is the first side lobe level of the window function, and $\tau_{\text{FSLL}} = \frac{1}{2}\left(\tau_{\text{main lobe}} + \tau_{\text{side lobe}}\right)$ is the location of the FSLL peak, where $\tau_{\text{main lobe}} = \frac{2\zeta_{\text{main lobe}}}{F_s}$ is the main lobe width between the first zero crossings, $\zeta_{\text{main lobe}}$ is a factor depending on the window function, F_s is the frequency bandwidth, and $\tau_{\text{side lobe}}$ is the width of the first side lobe. For instance, SLF = -3 dB/Octave, FSLL = -6.5 dB, and $\zeta_{\text{main lobe}} = 1$ for the rectangular window, while SLF = -3 dB/Octave, FSLL = -21.5 dB, and $\zeta_{\text{main lobe}} = 2$ for the Hamming window. The width of the first side lobe in both the Hamming and the rectangular window is the same and equal to $\frac{1}{F_s}$. As a case in point, to detect a delay peak 1 ns away from the zero delay peak with $F_s = 3$ GHz, $|\Delta A| < 9.5$ dB and $|\Delta A| < 22.2$ dB are required for the rectangular and the Hamming window functions, respectively. This effect is shown in Fig. 3.17 for which the stronger delay peak is that at $\tau = 0$ ns.

On the other hand, if the weak amplitude delay peak resides between the $\frac{1}{2}\tau_{\text{main lobe}}$ and τ_{FSLL} of the strong amplitude delay peak, the two peaks can be resolved if $|\Delta A| <$ |FSLL|. As an example, to detect a delay peak at 0.4 ns using the rectangular window, $|\Delta A|$ should be less than 6.5 dB, while to detect a delay peak at 0.8 ns using the Hamming window, $|\Delta A|$ should be less than 21.5 dB, as shown in Fig. 3.18. In the case of multiple delay peaks, (3.43) still holds for any two closely spaced peaks in time, but the sidelobe parameters are set by the peak with the highest sidelobes at the two close peaks, which is often the zero delay peak in the ACF.

If the autocorrelation delay peaks can be resolved, their amplitudes and positions could be biased due to the side lobe leakage of both the zero delay and other peaks. The bias from the zero delay peak is visible in both Figures 3.17 and 3.18. To reduce the effects of this bias on amplitude and time delay detection, the window function should exhibit low-amplitude sidelobes far from the main lobe, and the transition to the low sidelobes should be very rapid [30]. On the other hand, if the autocorrelation

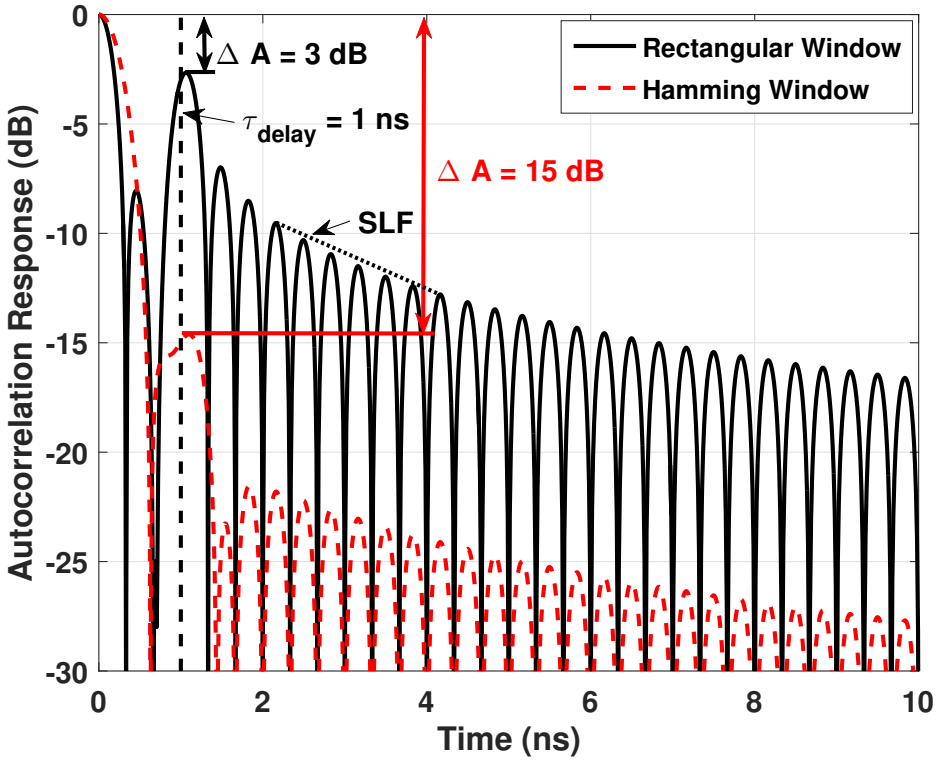

Figure 3.17: Simulated autocorrelation response with a delay peak at 1 ns. The bandwidth is 3 GHz. The delay peak has an amplitude of -3 dB for the rectangular window (black solid line) and -15 dB for the Hamming window (dashed red line).

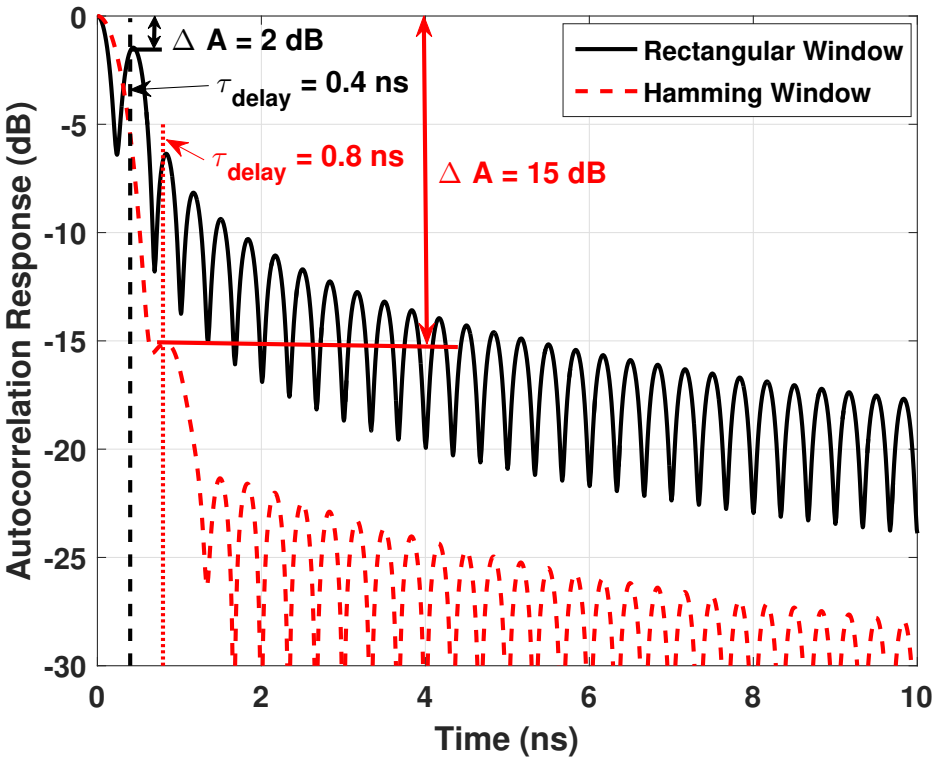

Figure 3.18: Simulated autocorrelation response with delay peaks at 0.4 ns with -2 dB amplitude for the rectangular window (black solid line) and at 0.8 ns with -15 dB amplitude for the Hamming window (red dashed line). The bandwidth is 3 GHz.

delay peaks cannot be resolved, we can only detect one of the two adjacent peaks with biased amplitude and position. The position of the detected peak would be biased to the crossover point (half-way between the two peaks) for two equal amplitude peaks or to a point between the crossover point and the strong delay peak for two unequal amplitude peaks, and it would get closer to the stronger peak as the $|\Delta A|$ becomes larger. For example, in the case of using a Hamming window with $F_s = 3$ GHz, the time delay of a 35.5 cm icepack is shifted from 4.2 ns to 4.3 ns in the presence of a thin 3 cm dry snowpack, as shown in Fig. 3.19.

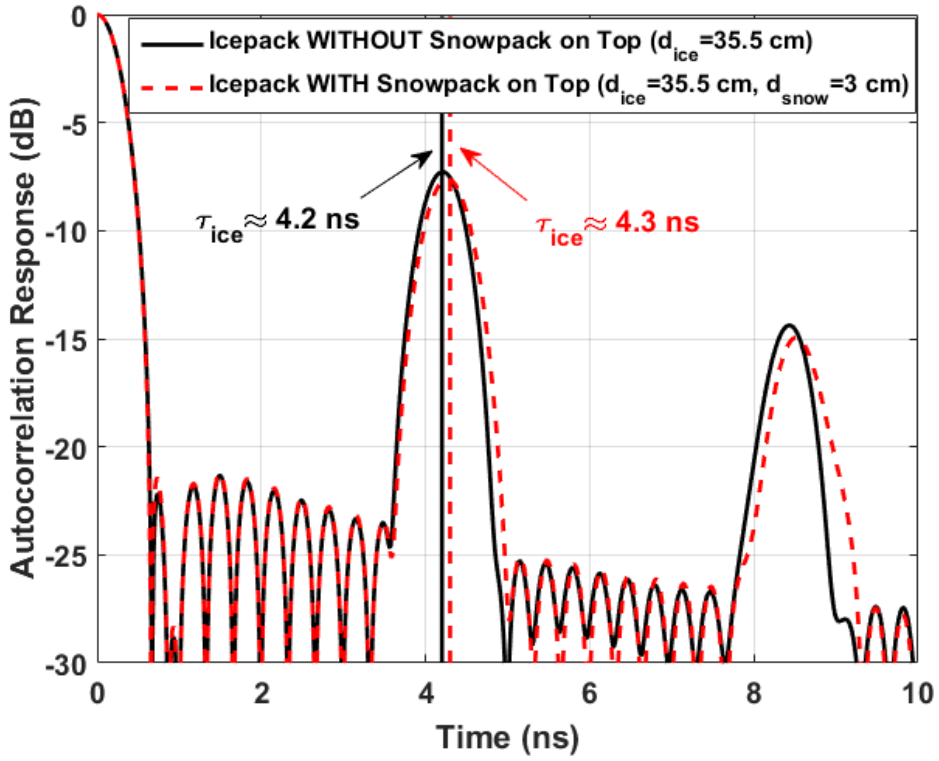

Figure 3.19: Simulated autocorrelation response of a 35.5 cm icepack ($n_{ice} = \sqrt{3.15}$) without (red dashed line) and with (solid black line) a 3 cm snowpack ($\rho_s = 210\ \mathrm{kg/m^3}$, $n_{snow} = 1.18$) on top. The Hamming window was used, and the bandwidth was 3 GHz ($\theta = 0°$, $\tau_{ice} = 4.2$ ns, $\tau_{snow} = 0.2$ ns, and $|\Delta A| \approx 1.4$ dB).

3.2.5.2 Limits of Detection

The emissivity can be approximated with a Taylor expansion [57], for which the zeroth and first order terms are

$$e(f) \approx \overline{e}\Bigg(1 - 2\Big[A_i \cos(\omega\tau_{ice}) + A_s \cos(\omega\tau_{snow}) + A_\Sigma \cos\Big(\omega\big(\tau_{snow} + \tau_{ice}\big)\Big) + A_\Delta \cos\Big(\omega\big(\tau_{snow} - \tau_{ice}\big)\Big)\Big]\Bigg) \tag{3.44}$$

The absolute value of the ripple amplitudes are plotted with respect to the incident angle in Fig. 3.20. In H-pol configuration, it can be observed that A_Δ has the lowest value at all the angles while A_i has the largest value from nadir up to 75°. After $\theta = 75°$, A_Σ becomes dominant. All the ripple amplitudes in each detection scenario are lower in V-pol configuration compared to H-pol configuration. Moreover, the amplitude values become close to zero at some angles in V-pol configuration due to the Brewster angles between the air and snow and between the snow and ice.

As in [57], the minimum N_{ind} is dependent on the receiver operating characteristics, noise figure, and the discrimination function, $D(\theta)$.

$$N_{ind} > 2\frac{(Z_{FA} + Z_{PD})^2}{N_f} \cdot D^2(\theta) \ \cdot F^2 \tag{3.45}$$

where the F is the receiver noise figure, N_f is the number of frequency points, and Z_{FA} and Z_{PD} are the number of standard deviations from the magnitude of the expectation of the ACF in the absence and presence of a slab. They determine the false alarm rate and probability of detection, respectively [57].

The discrimination function depends only on the detection scenario, the window function, and the incidence angle, as given by [57]

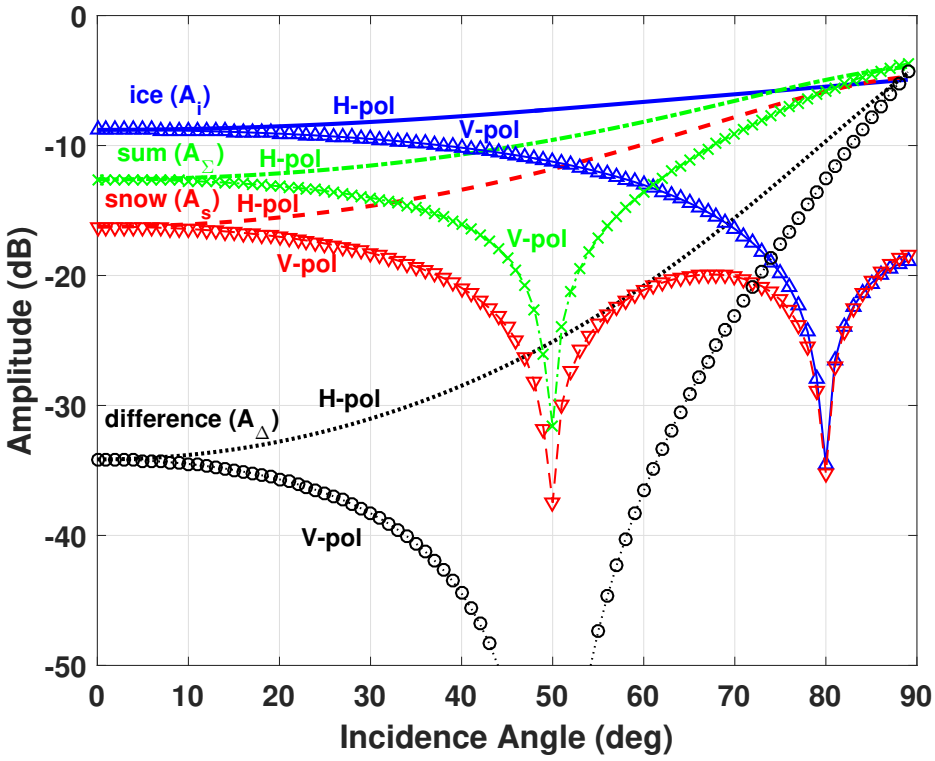

Figure 3.20: The half amplitude of the ripples with respect to the incidence angle ($\rho_s = 210$ kg/m^3). The Brewster angle between air and snow is at about $\theta = 50°$, and the Brewster angle between snow and ice is at about $\theta = 80°$.

$$D_\ell(\theta) = \left(\frac{\sqrt{W_2(0)}}{W_1(0)} \right) \Big/ \left(|A_\ell| \ \overline{e} - \mathrm{SNR}_\Phi e_{absence} \ \right) \tag{3.46}$$

where $\ell = i, s, \Sigma, \Delta$. As explained in [57], $D(\theta)$ must be positive, so that the delayed peak rises above the autocorrelation noise floor. The square of the positive values of this discrimination function for lake icepack with top dry snowpack at τ_{ice}, τ_{snow}, $\tau_{ice}+\tau_{snow}$, and $\tau_{ice}-\tau_{snow}$ are shown in Figures 3.21(a), 3.21(b), 3.21(c), and 3.21(d), respectively. For the snowpack, we used $\rho_s = 210$ kg/m^3. It can be observed that the N_{ind} needed to detect the time delay for any of the four peaks is lower in H-pol configuration compared to the V-pol configuration regardless of the window function at most of the incidence angles. Moreover, similar to Fig. 3.20, we are only able to detect the time delay at few angles in V-pol configuration due to the Brewster angle between the air and snow and between the snow and ice while we can detect the time delay at nearly all incidence angles in H-pol regardless of the window function. The choice of the Kaiser-Bessel ($\alpha_k = 3.02$, FSLL = -35 dB, and $\zeta_{mainlobe} = 2.39$) window function in post processing could be helpful due to its lower sidelobes at the expense of coarser resolution. The minimum N_{ind} is inversely proportional to the ripple amplitudes shown in Fig. 3.20, indicating that τ_{ice} is the easiest lag to measure, and $\tau_{ice} - \tau_{snow}$ is the most difficult. Finally, Fig. 3.21 predicts that the microwave propagation times in both lake icepack and the top dry snowpack are detectable at angles away from nadir to close to grazing with appropriate choice of polarization and window function, similar to the results from Fig. 3.20.

3.2.6 Singled Layered Media with Variable Thicknesses

The presence of variable pack thickness within a footprint of the radiometer's antenna will add complexity to the retrieved time delay. This issue is more severe

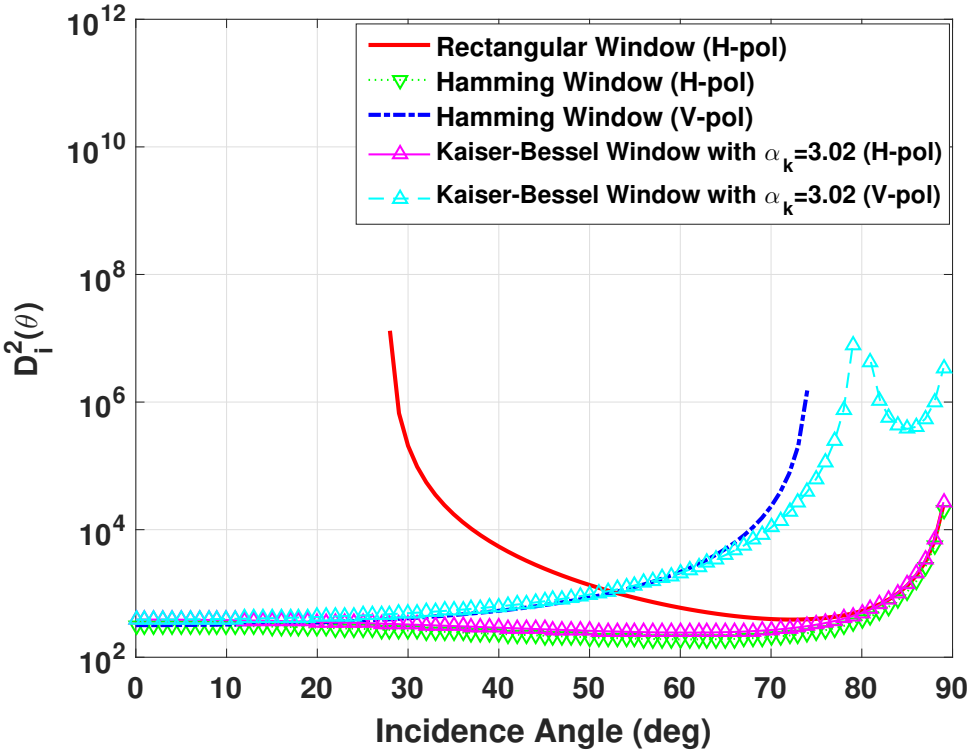
Rectangular Window (H-pol)
Hamming Window (H-pol)
Hamming Window (V-pol)
Kaiser-Bessel Window with α_k=3.02 (H-pol)
Kaiser-Bessel Window with α_k=3.02 (V-pol)
$D_i^2(\theta)$
10^{12}
10^{10}
10^{8}
10^{6}
10^{4}
10^{2}
0
10
20
30
40
50
60
70
80
90
Incidence Angle (deg)

(a)

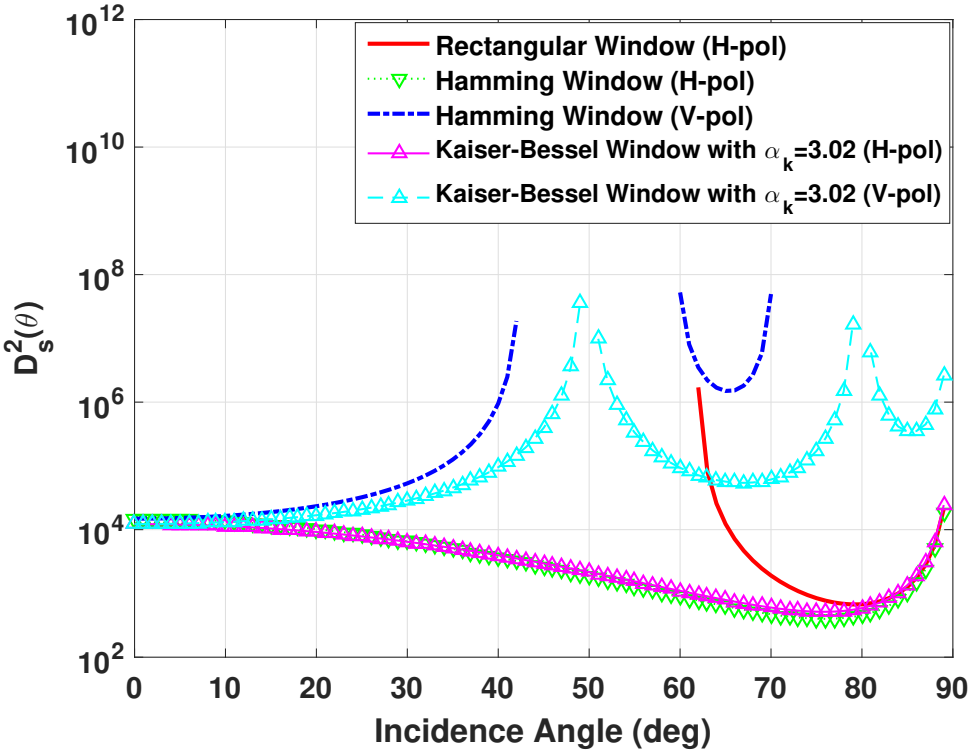
Rectangular Window (H-pol)
Hamming Window (H-pol)
Hamming Window (V-pol)
Kaiser-Bessel Window with α_k=3.02 (H-pol)
Kaiser-Bessel Window with α_k=3.02 (V-pol)
$D_s^2(\theta)$
10^{12}
10^{10}
10^{8}
10^{6}
10^{4}
10^{2}
0
10
20
30
40
50
60
70
80
90
Incidence Angle (deg)

(b)

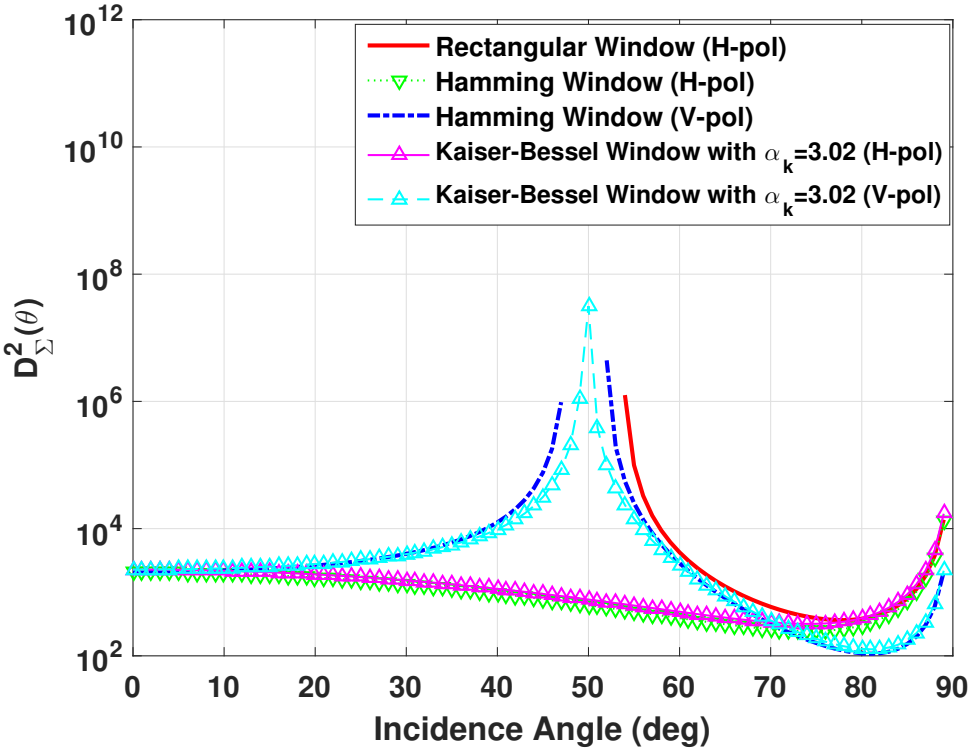

(c)

for WiBAR on airborne and space-borne platforms than WiBAR on ground-based platforms since the footprint for a given radiometer antenna is larger. In the following section, using a simple forward model for a layer having distinct thickness values within one footprint (pixel), the system requirements for resolving these distinct thickness values are derived. The statistics of the ACF, measurement uncertainty, and the effect of the antenna elevation beamwidth is similar to the single layered media as discussed in Section 3.2.4.

3.2.6.1 Minimum and Maximum Resolvable Sub-Pixel's Thickness

The ability of the WiBAR to detect multiple distinct time delays within a single footprint depends on its ability to resolve two autocorrelation peaks in the time domain. This situation was discussed in [54] for the case of snow over ice, and can be readily adapted to a single layer with different thicknesses. The criteria for resolution

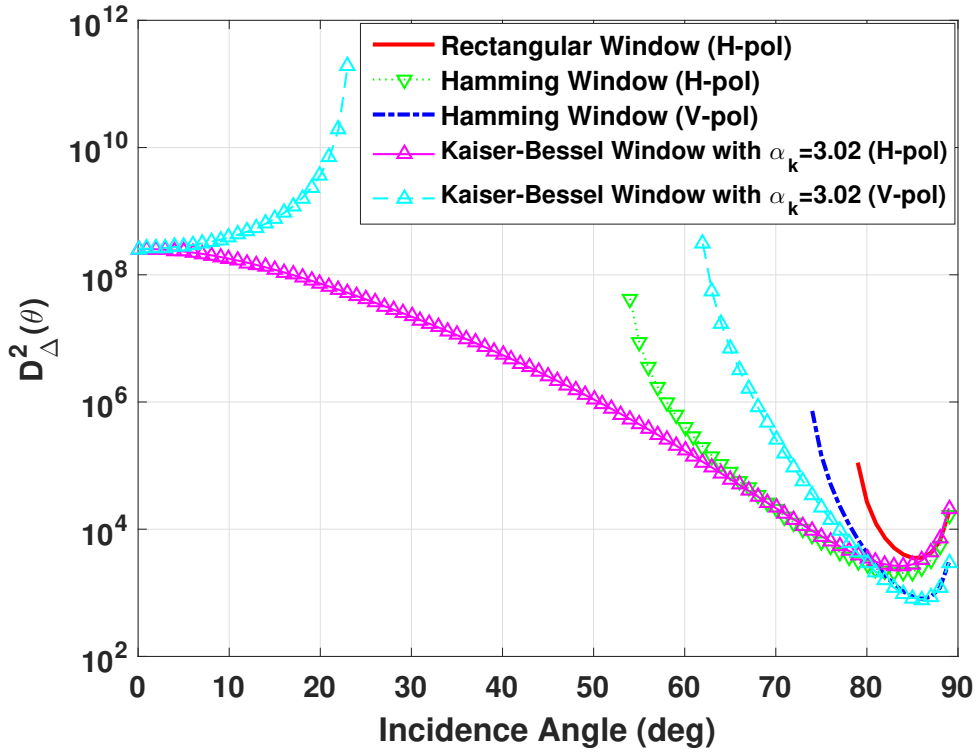

(d)

Figure 3.21: The square of the positive values of the discrimination function $D(\theta)$ for the delay peak at (a) τ_{ice} (b) τ_{snow} (c) $\tau_{ice} + \tau_{snow}$ (d) $\tau_{ice} - \tau_{snow}$ as a function of incidence angle. The snowpack density is $\rho_s = 210$ kg/m^3 ($n_{snow} = 1.18$).

depends on the magnitude of $\Delta\tau$, the difference between the ACF peaks, relative to $1/F_s$, where F_s is the WiBAR frequency span, and on the window function used in the IFFT. Different window functions reveal different features of the ACF, typically trading temporal resolution for sidelobe level. The choice of window function does not need to be made prior to the measurements. Multiple window functions can be used to discover the properties of the target.

The first criteria is when $|\Delta\tau| > \tau_{\text{FSLL}}$, where $\tau_{\text{FSLL}} = \frac{1}{2}\left(\tau_{\text{main lobe}} + \tau_{\text{side lobe}}\right)$ is the location of the first sidelobe peak, $\tau_{\text{side lobe}} = 1/F_s$ is the null-to-null width of the window function sidelobe, $\tau_{\text{main lobe}} = 2\zeta/F_s$ is the null-to-null width of the window function main lobe, and ζ is one plus the order of the cosine-sum window function ($\zeta_{\text{rectangular}} = 1$, $\zeta_{\text{Hamming}} = 2$, etc.). Under this circumstance, the maximum difference between the sub-pixel solid angles (a_{ij}) for two distinct thicknesses is given by

$$\begin{aligned} |\Delta A| &= \left| 10\log_{10}\left(\min\left\{\frac{a_{ij}}{a_{mn}}, \text{for } mn \neq ij\right\}\right)\right| \\ &< |\text{FSLL}| + \left[|\text{SLF}| \times \log_2\left(\frac{|\Delta\tau|}{\tau_{\text{FSLL}}}\right)\right] \end{aligned} \tag{3.47}$$

where FSLL (dB) is the first sidelobe level of the window function, SLF (dB/Octave) is the side lobe fall-off of the window function, and $|\Delta A|$ is the difference in the amplitude of the delay peaks. As an example, to detect a 10 cm ($|\Delta\tau| = 1$ ns at $\theta_0 = 75°$) sub-pixel thickness distinction with $F_s = 3$ GHz, the difference between the delay peaks should be $|\Delta A| < 9.5$ dB and $|\Delta A| < 22.3$ dB for the rectangular and the Hamming window functions, respectively. This effect is shown in Fig. 3.22, where it is assumed there are two sub-pixels with $a_{11} = 0.1$ and $a_{12} = 0.9$, or, equivalently, $|\Delta A| = 9.5$ dB. The delay peak at 40 cm (the weak amplitude) is shifted from 4.0 ns to 3.9 ns, which is due to the side lobe leakage of the strong delay peak at 50 cm [54]. Nonetheless, resolution of the two thicknesses is very clear because $|\Delta\tau| > \tau_{\text{FSLL}}$.

On the other hand, if the sub-pixel thickness distinction is small such that the

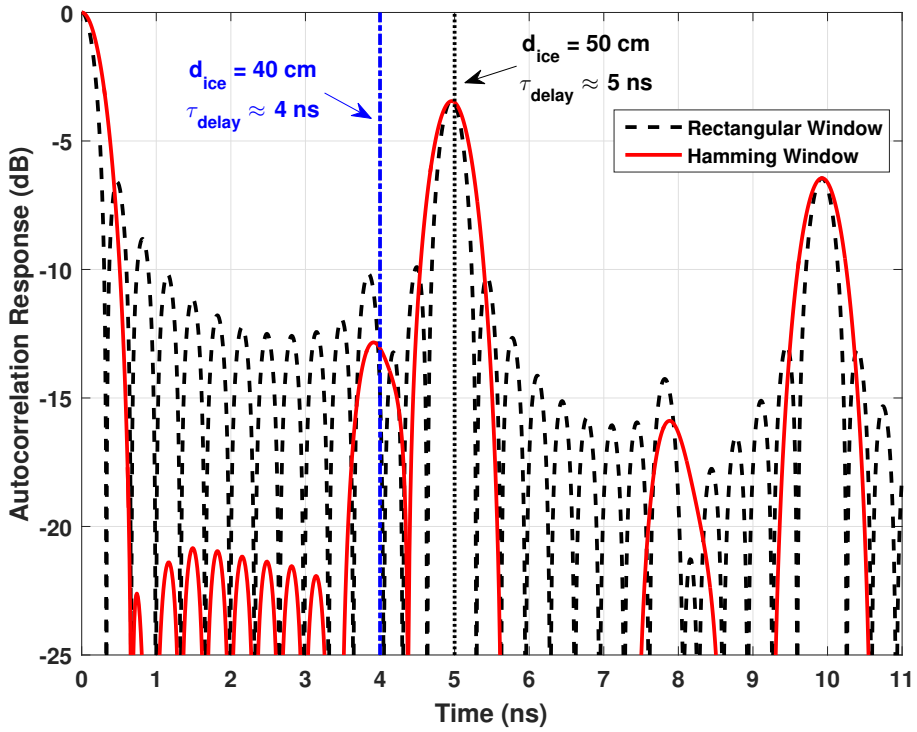

Figure 3.22: Simulated autocorrelation response of an icepack with two thicknesses of 40 cm and 50 cm with different area size using rectangular and Hamming window functions. The delay peaks are about 1 ns away from each other. The system's bandwidth is 3 GHz. The antenna's gain pattern coefficients in each sub-pixel are $a_{11} = 0.1$ and $a_{12} = 0.9$ ($|\Delta A| = 9.5$ dB). The sub-pixel difference can be resolved using the Hamming window function, while it cannot be resolved using the rectangular window function ($\theta_0 = 75°$).

weak delay peak is between the $\frac{1}{2}\tau_{\text{main lobe}}$ and τ_{FSLL} of the strong delay peak, the sub-pixel variability can be resolved if $|\Delta A| < |\text{FSLL}|$ [54]. For instance, to detect a sub-pixel thickness distinction of 4 cm (0.4 ns) using the rectangular window, $|\Delta A|$ should be less than 6.5 dB, while to detect a sub-pixel thickness distinction of 8 cm (0.8 ns) using the Hamming window, $|\Delta A|$ should be less than 21.5 dB. Figure 3.23 demonstrates this effect for the rectangular window, and Fig. 3.24 shows it for the Hamming window.

If the sub-pixel thickness distinction is less than $\frac{1}{2}\tau_{\text{main lobe}}$, the minimum detectable thickness by WiBAR, there would be one delay peak in ACF. This one peak

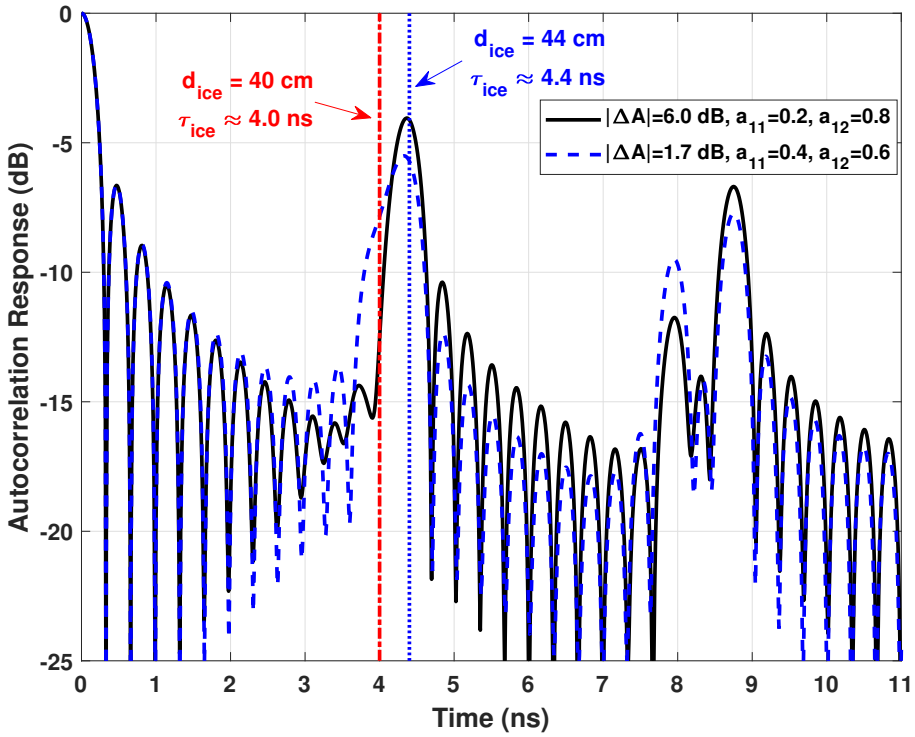

Figure 3.23: Simulated autocorrelation response of an icepack with two variable thicknesses of 40 cm and 44 cm using a rectangular window. The delay peaks are about 0.4 ns away from each other. The amplitude difference between the delay peaks should be less than about 6.5 dB to be resolved ($\theta_0 = 75°$).

will be wider in time and lower in amplitude than it would be for a single thickness. This effect can be observed in Fig. 3.23 for the peak at 4.4 ns.

The upper limit to the maximum detectable time delay is similar to [57] and determined by the resolution bandwidth (RBW) of the spectrum analyzer and the number of frequency bins. Finally, limits of detection and the minimum number of independent samples required to detect the time delays is explained in detail above and in [57].

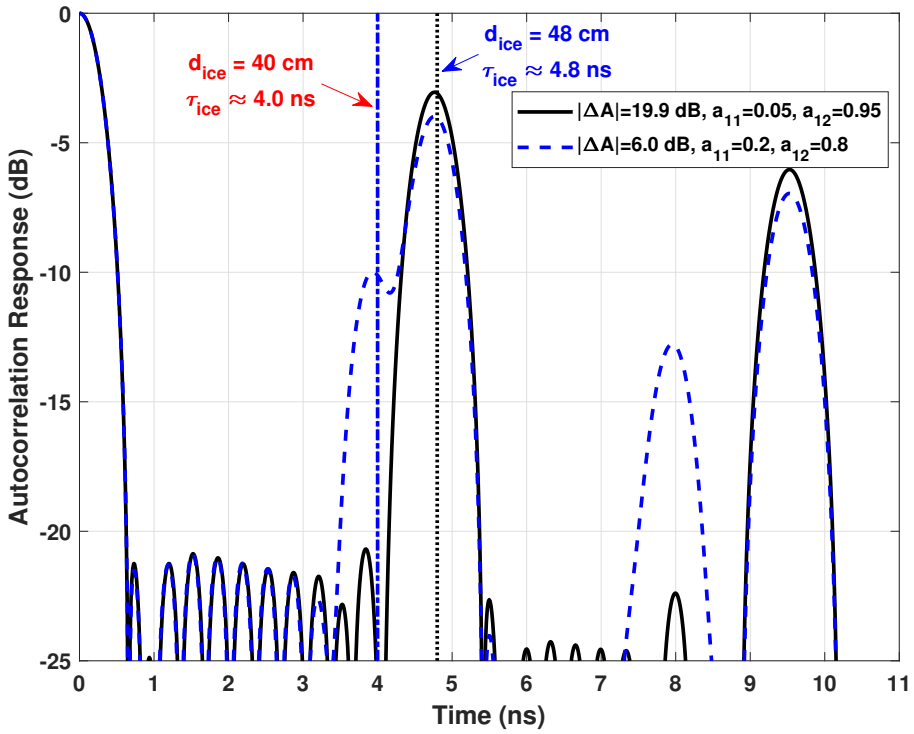

Figure 3.24: Simulated autocorrelation response of an icepack with two variable thicknesses of 40 cm and 48 cm using a Hamming window. The delay peaks are about 0.8 ns away from each other. The amplitude difference between the delay peaks should be less than about 21.5 dB to be detected ($\theta_0 = 75°$).

3.3 Non-Destructive Dielectric Constant Measurement of Low-Loss Dielectric Slabs using WiBAR

The knowledge of the interaction of electromagnetic waves with natural and man-made materials is of great importance in today's engineering and manufacturing applications. The behavior of electromagnetic waves in homogeneous media is mainly dependent on medium's macroscopic parameter, the relative dielectric constant. The relative dielectric constant, or relative permittivity, of a material is an electrical property of the material which changes the magnitude, phase, and direction of an applied electric field. The dielectric constant is a complex quantity. The real part is related to the dipole moment per unit volume of the material, while the imaginary part is

related to the dissipated heat. For a low-loss material, where there is no significant absorption or heat dissipation, the dielectric constant would be nearly a real quantity. There are many techniques and procedures reported in the literature for the measurement of the dielectric constant of materials, such as the resonant techqnique and the transmission line method [36, 34, 35, 4]. However, these methods require direct sampling of a material, which is mostly destructive and sometimes impossible to perform for some materials, such as snowpacks on high altitude mountains. To address these issues, we developed a new and non-destructive measurement technique of the dielectric constant of a low-loss dielectric slab, such as dry snowpack or freshwater lake icepack, using the wideband autocorrelation radiometry (WiBAR) [57, 15, 59]. This section shows the ability of the WiBAR in directly and non-destructively measuring the dielectric constant and thickness of a loss-less slab. Here, we assume that the environment provides ideal properties for our retrieval, and there is no radio frequency interference (RFI) and target imperfections of absorption, volume scattering, and surface scattering.

The measured time delay by WiBAR, τ_{delay}, for a homogeneous and isotropic pack is given by (2.4). If a delay peak can satisfy the detection criteria, as discussed above and in [57], at two distinct incidence angles, ϵ_p and d_p can be found using (2.4) at the two incidence angles, as given by [55]

$$\epsilon_p = \frac{\tau_1^2 \sin^2\theta_2 - \tau_2^2 \sin^2\theta_1}{\tau_1^2 - \tau_2^2} \tag{3.48a}$$

$$d_p = \frac{c\tau_i}{2\sqrt{\epsilon_p - \sin^2\theta_i}} \tag{3.48b}$$

where i =1 or 2, and τ_1 and τ_2 are the measured time delay by WiBAR at incidence angles θ_1 and θ_2, respectively. Assuming a pencil beam antenna, the error in the measured ϵ_p and d_p is mainly due to the error in the measured time delay by WiBAR,

and it can be calculated using the error propagation rule, as given by

$$\delta\epsilon_p = \sqrt{\left(\frac{\partial\epsilon_p}{\partial\tau_1}\cdot\delta\tau_1\right)^2 + \left(\frac{\partial\epsilon_p}{\partial\tau_2}\cdot\delta\tau_2\right)^2} \tag{3.49a}$$

$$\delta d_p = \sqrt{\left(\frac{\partial d_p}{\partial\tau_i}\cdot\delta\tau_i\right)^2 + \left(\frac{\partial d_p}{\partial\epsilon_p}\cdot\delta\epsilon_p\right)^2} \tag{3.49b}$$

where i =1 or 2, and $\delta\tau_1 = \delta\tau_2 = \delta\tau$, where $\delta\tau$ is the error in the measured time delay by WiBAR, as discussed in Chapter IV. Using (3.48), (3.49) can be further expanded, as given by

$$\delta\epsilon_p = \frac{2\delta\tau\left|\sin^2\theta_2 - \sin^2\theta_1\right|\tau_1\tau_2}{\left(\tau_1^2 - \tau_2^2\right)^2}\cdot\sqrt{\tau_1^2+\tau_2^2} \tag{3.50a}$$

$$\delta d = d_m\cdot\sqrt{\left(\frac{\delta\tau_i}{\tau_i}\right)^2 + \left(\frac{\delta\epsilon_p}{\epsilon_p - \sin^2\theta_i}\right)^2} \tag{3.50b}$$

3.4 Simulated Laboratory Measurements

Before using the WiBAR instruments in the field measurements, we performed simulated laboratory measurements to prove the concept of the WiBAR and test our instruments. The block diagram of the microwave scene simulator is shown in Figure 3.25 [60]. The loops consisting of two 180 degree hybrid couplers, plays the role of multiple reflection inside the pack. The upper hybrid coupler resembles snow-terrain or ice-water interface, and the lower one models the snow-air or ice-air interface. The length of the coaxial cables are equal the thickness of the pack, and the attenuators account for attenuation in the pack as the microwave travels through it. The noise source followed by the amplifiers accounts for the thermal radiation from the semi-infinite medium beneath the pack. The receiver is the spectrum analyzer. The laboratory setup is also shown in Figure 3.26.

The measured power spectrum is shown in Figure 3.27. Using (3.4), the ACF

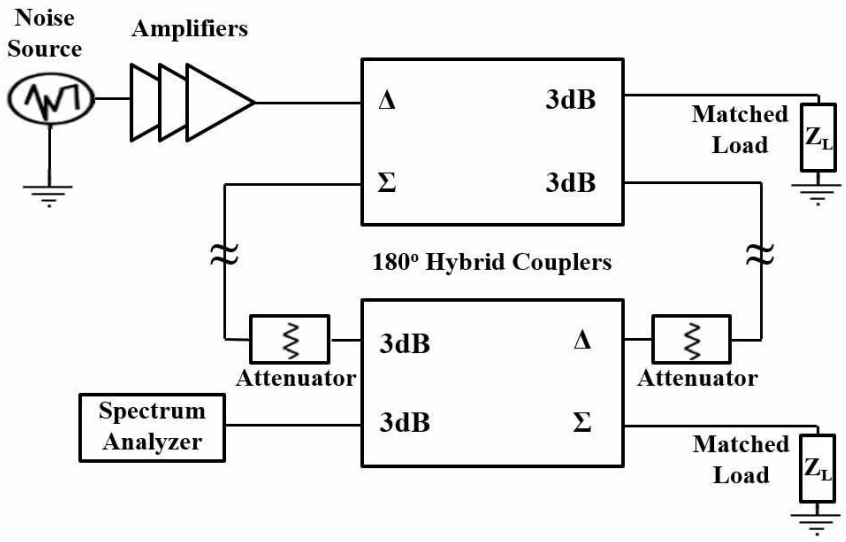

Figure 3.25: The schematic of the microwave scene simulator. Two coaxial cables are used to connect the upper and lower 180 degree hybrid couplers representing the roundtrip withing the pack.

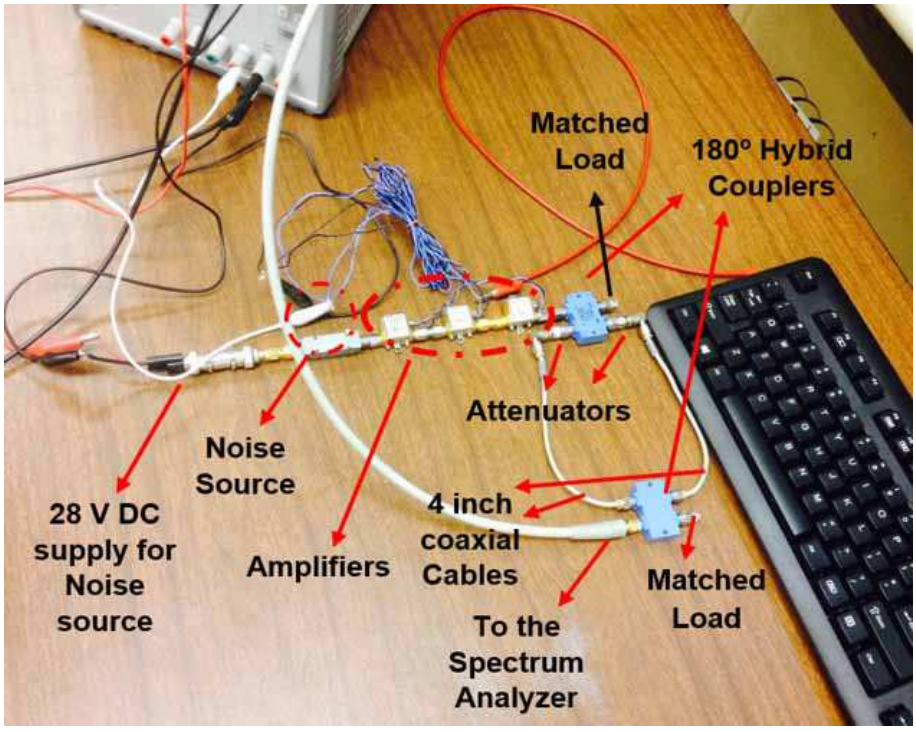

Figure 3.26: The laboratory setup of the microwave scene simulator. The coaxial cables' length are 4 inches (10.16 cm).

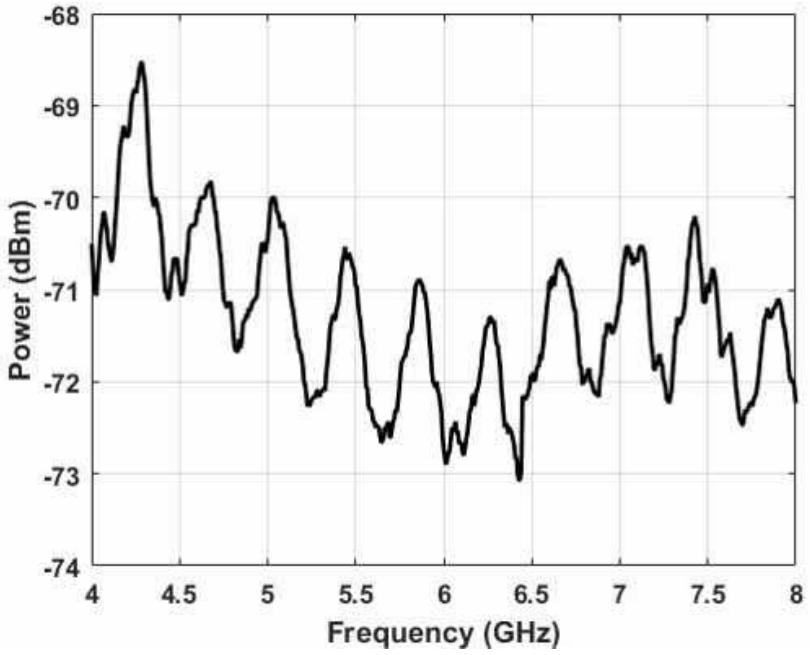

Figure 3.27: The measured power spectrum of the microwave scene simulator model with 4 inches (10.16 cm) coaxial cables.

of the measured power spectrum can be found, as shown in Figure 3.28. Different window functions, such as Kaiser, Blackman, and Hanning (Hann) were used. It can be observed from Figure 3.28 that the measured timed delay by WiBAR for 4 inches (10.16 cm) coaxial cables is 2.47 ns. The measured time delay by a vector network analyzer (VNA) is 2.48 ns. This proves the ability of this technique in measuring the microwave propagation time through the pack.

3.5 Field Measurements and Results

In this section, the potential of this technique as an inversion algorithm is demonstrated using a limited set of field measurements of lake icepack. These measurements are divided into different categories based on the target characteristics, such as single layer of ice/snow, two layer media of ice with snow cover, and single layer media with thickness variation within a footprint of the radiometer's antenna.

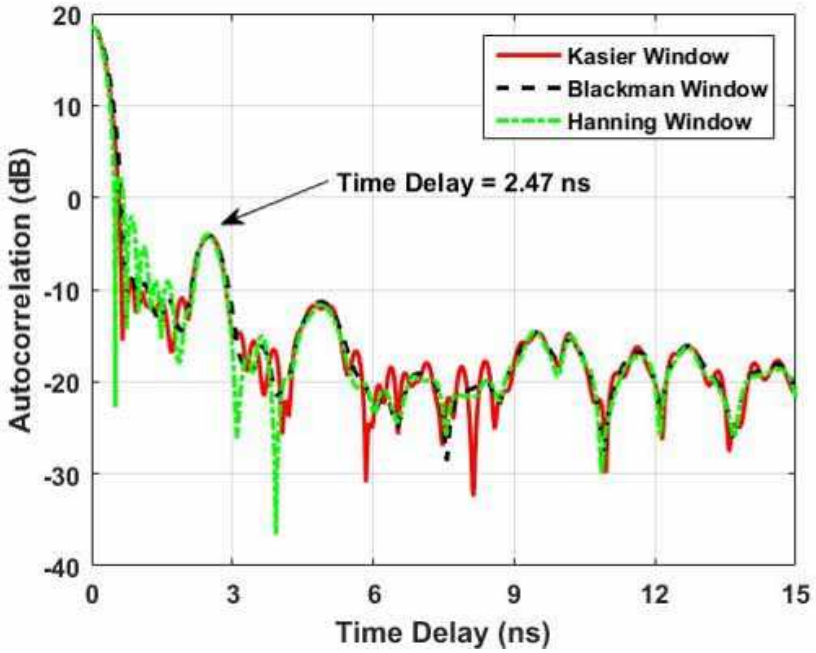

Figure 3.28: The ACF of the measured power spectrum of the microwave scene simulator model with 4 inches (10.16 cm) coaxial cables. The measured time delay by WiBAR is 2.47 ns.

3.5.1 Single Layer Media of Ice/Snow

The lake icepack measurements were conducted on Douglas Lake at the University of Michigan Biological Station (UMBS) on March 02, 2016. The first fabricated X-band WiBAR instrument using the portable spectrum analyzer (Agilent N9344C) was used (first version of X-band WiBAR). This instrument was explained in Section 3.2.1.1. The lake ice was solid black ice (no air bubbles or frozen snow), and the thin snow cover was removed prior to the measurements. The measurements were conducted in H-pol, with an antenna with $a_H = 27.9$ cm. The incidence angles ranged from 0.9° to 59.1°. At each angle, 461 frequency points were collected on a portable spectrum analyzer, which was swept from 7 GHz to 10 GHz with $N_{trace} = 100$. The measurement setup is shown in Fig. 3.29(a). The icepack thickness was measured with a tape measure after hand-coring the ice at the conclusion of the WiBAR measurements, as shown in Fig. 3.29(b). The measurements reported here were conducted

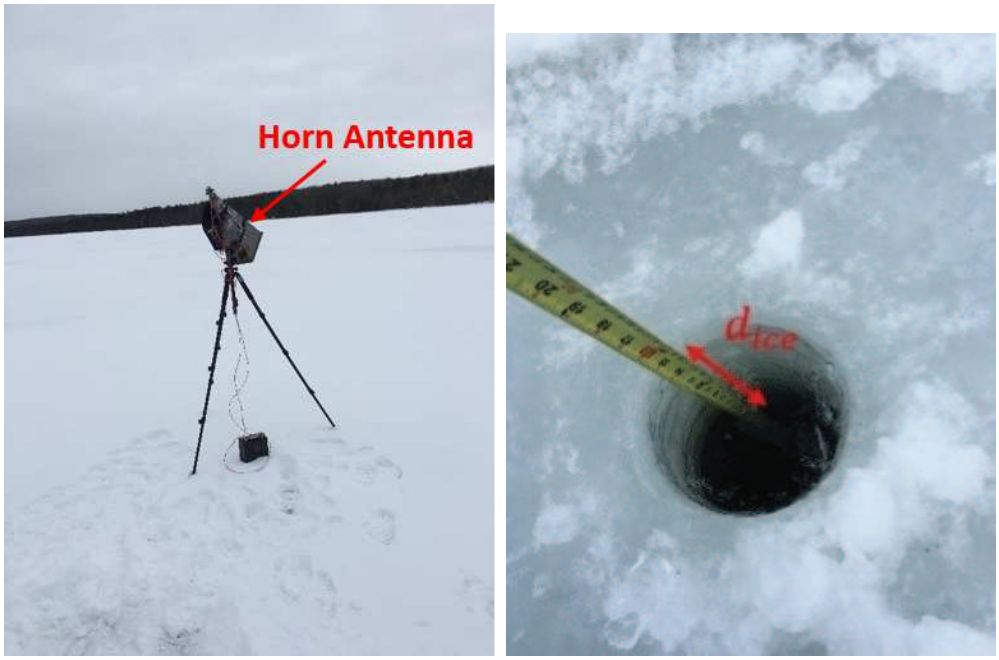

(a) (b)

Figure 3.29: (a) Measurement setup of the lake icepack measurement using a wide-band autocorrelation radiometer (WiBAR) on a tripod (a motorcycle battery was used as a power source) and (b) ground truth measurement of the lake icepack.

at one location and during one day.

Measurements of sky and microwave absorber were also conducted to obtain spectra for targets whose emissivity approximated 0 and 1, respectively. These were then used to correct the averaged power spectra of the target to yield spectra of emissivity. As an example, one of the power spectra of the sky, absorber, and lake ice observations is shown in Fig. 3.30. The lake ice observations were made from about noon until around 5:00 pm on March 02, 2016, and the sky and microwave absorber measurements were made after all the measurements at around 5:15 pm on the same day. The physical temperature of the absorber was not measured, but is affected by the air temperature, which was about -5^{o}C and -6^{o}C at noon and 5:00 pm, respectively. However, since our main measurement objective is to passively measure a time delay and not a brightness amplitude, the time difference between the lake ice and calibration targets (sky and microwave absorber) measurements should not impact

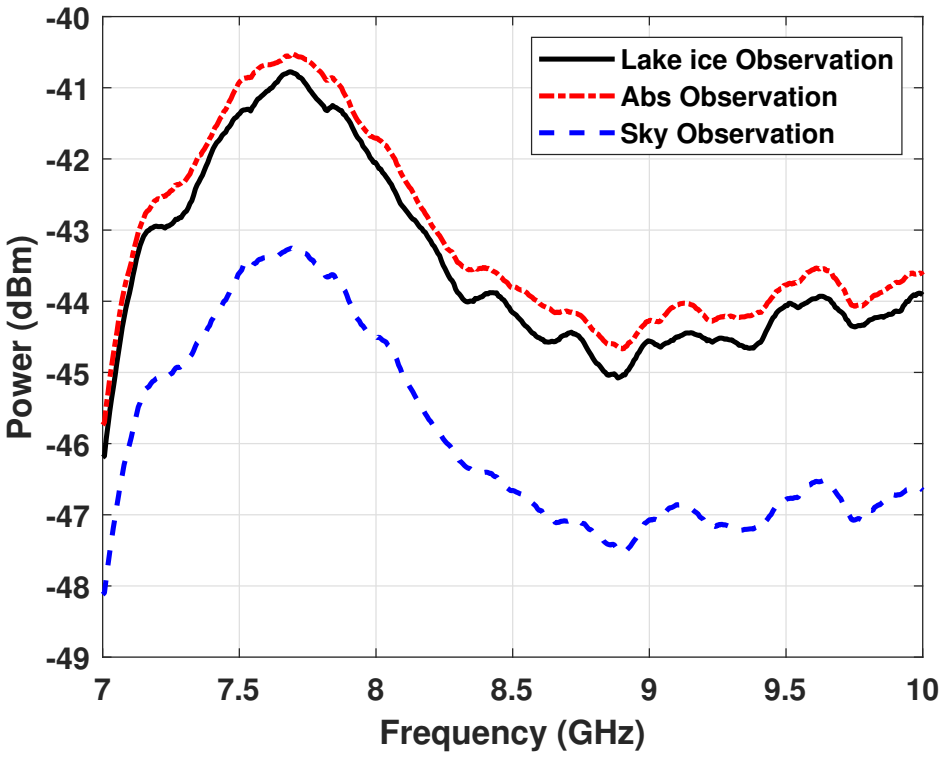

Figure 3.30: Sky, absorber, and lake icepack observation on Douglas Lake on March 02, 2016 ($\theta = 59.1°$, $d_{ice} = 35.5$ cm).

the results. The emissivity is obtained using the calibration procedure given by (3.3). The emissivity of the observation in Fig. 3.30 is shown in Fig. 3.31.

To find the time delay, the emissivity spectra were multiplied by a Hamming window, zero-padded to $N_f + N_z = 2^{14}$ to improve temporal precision, and inverse Fourier transformed to yield an autocorrelation function. The autocorrelation response of the measurement and the expected value of the autocorrelation response for a 35.5 cm icepack with its expected value is shown in Fig. 3.32. The first delay peak after the zero delay peak is at 3.84 ns. The incidence angle is 59.1°. There is about 9 dB difference in the first delay peak after zero between the model and measurement autocorrelation response. Gain variations due to temperature drift of electronics, as well as imperfections in the ice such as surface and volume scattering, can cause a decrease in the delayed autocorrelation peak, and these effects are not considered in

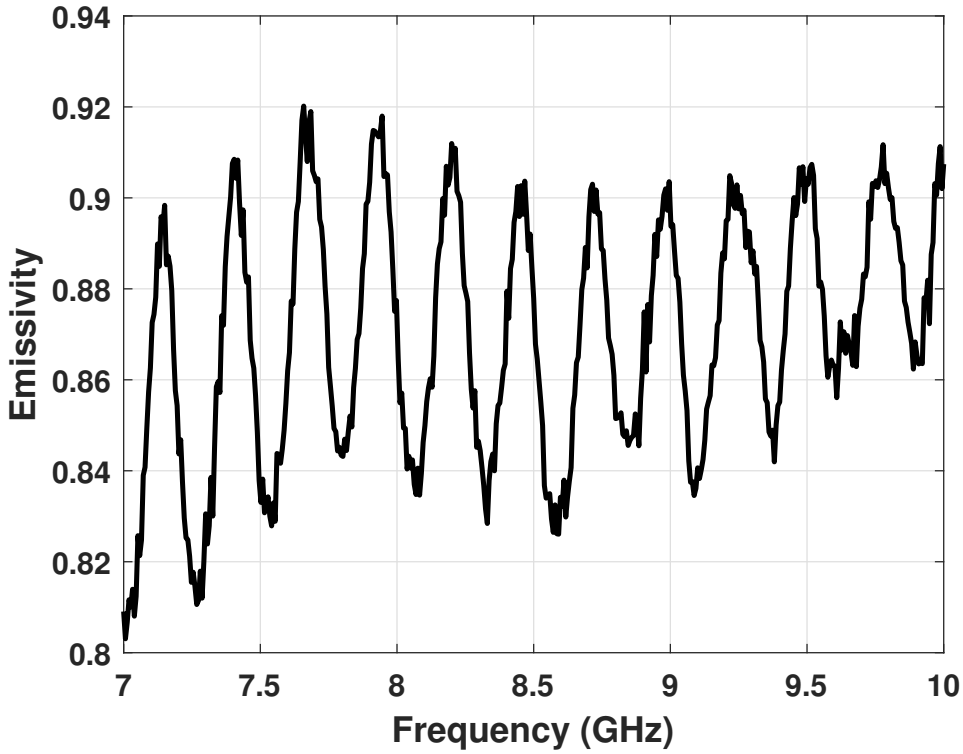

Figure 3.31: The spectral emissivity of the lake icepack measured on Douglas Lake on March 02, 2016 ($\theta = 59.1°$, $d_{ice} = 35.5$ cm).

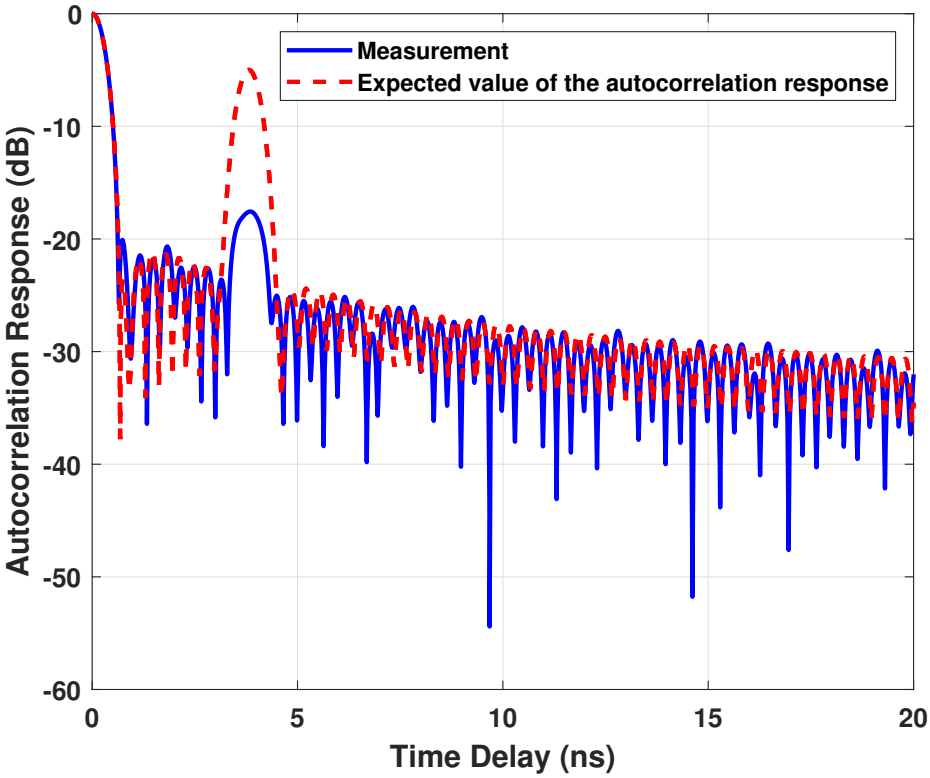

Figure 3.32: The autocorrelation function of the lake icepack measured on Douglas Lake on March 02, 2016 (blue solid line) with the expected value of the autocorrelation response of the lake icepack model. The Hamming window was used ($\theta = 59.1°$, $d_{ice} = 35.5$ cm).

the derivation of the expected value of the autocorrelation response. The magnitude of the delayed peak in all of our measurements of the lake ice can be seen in Fig. 3.16.

These measurements, as well as those for the sky and absorber, each took $N_{trace}T_s \approx$ 5 min, but the parameters for the measurements were set before the theory in the previous sections was developed. To demonstrate that τ_{delay} can be retrieved in significantly less time, Fig. 3.33 shows the inversion with N_f reduced from 461 to 47 equally spaced frequencies, yet still spanning $F_s = 3$ GHz. This reduces the maximum alias-free lag to 8 ns. The peak associated with the expected delay is still present, but the noise floor increases due to aliasing. By itself, this decimation in

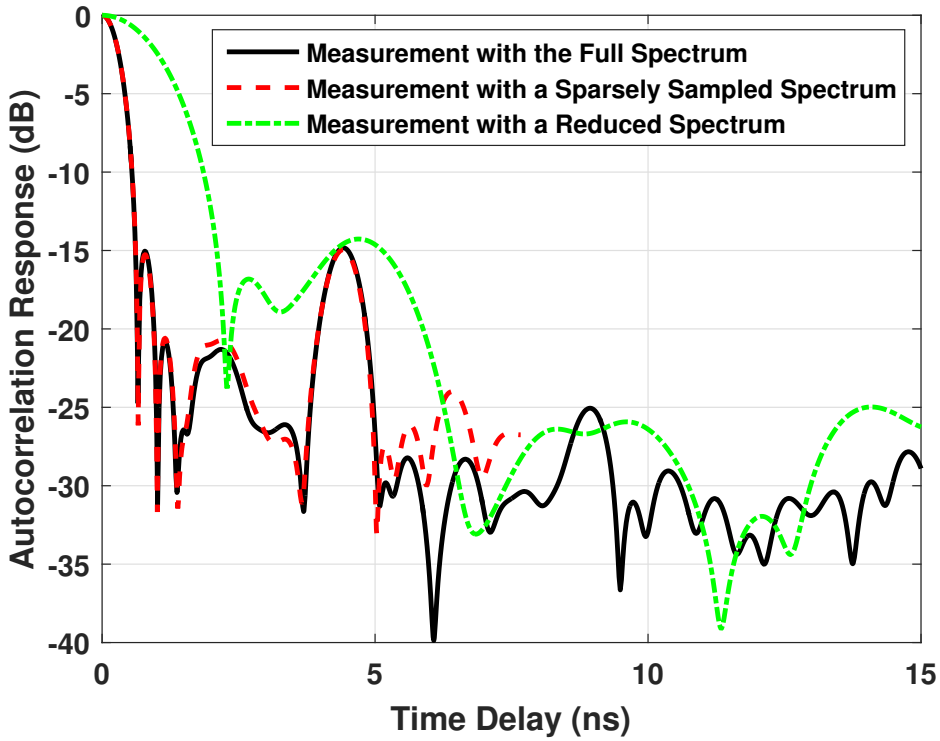

Figure 3.33: Measured autocorrelation function of the Douglas Lake icepack with the full spectrum analyzer spectrum ($N_f = 461$, $F_s = 3$ GHz), with a spectrum sparsely sampled ($N_f = 47$,$F_s = 3$ GHz), and with a reduced spectrum ($N_f = 47$, $F_s = 0.9$ GHz). The incidence angle is $\theta = 0.9°$. The Hann window was used.

frequency (if the spectrum analyzer allowed it) would reduce the measurement time to about 30 s. Further reductions in data acquisition time are possible by reducing N_{trace}. Figure 3.33 also demonstrates the effect of increasing τ_c by keeping N_f at 47 while decreasing the frequency span, F_s to 900 MHz. At this F_s, the peak is still present but is distorted due to the poorer temporal resolution.

The retrieved microwave propagation times for the icepack with respect to observation angle from 0.9° to 59.1° is plotted in Fig. 3.34. The expected values for the microwave propagation time through the icepack are obtained using (2.4) at incidence angles from 0° to 90° for three different thicknesses, $d_{ice} = 35.56, 36.83$ and 38.10 cm, and are also shown. We showed three different thicknesses with ±1.27 cm since our ground truth measurement tools were not very accurate. While we measured an ice

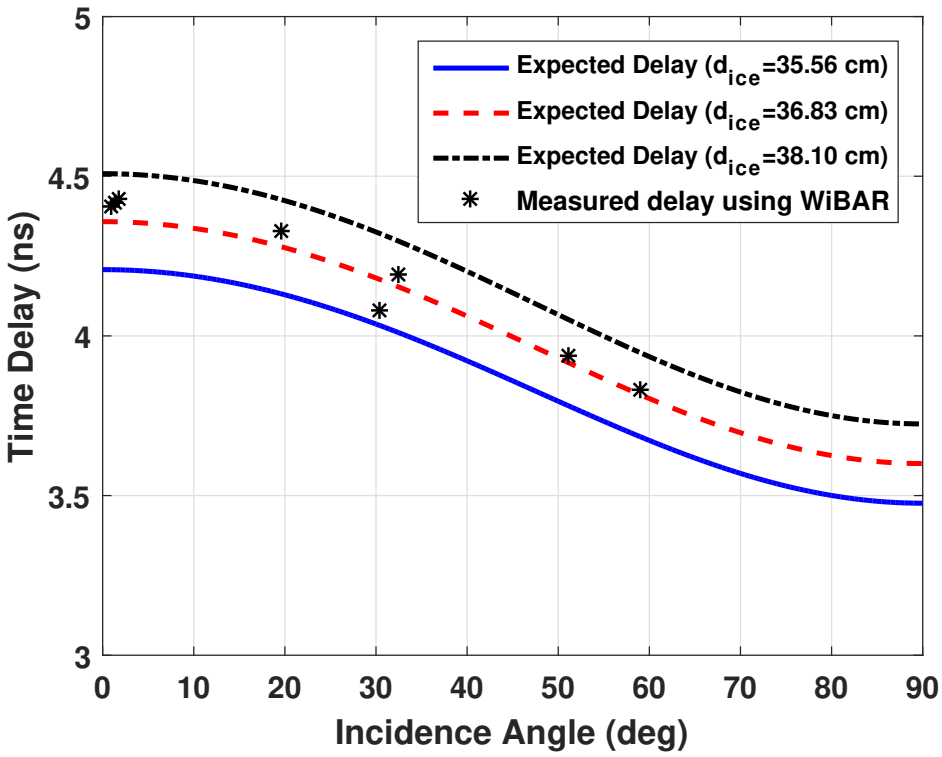

Figure 3.34: Measured and expected microwave propagation time using equation (2.4) through the icepack with respect to the incidence angle.

thickness of 35.6 cm, a slightly better fit to the measured delays is for a thickness of 36.8 cm. We suspect that the manual ice core tool caused chips of ice outside of the cored cylinder at the bottom of the ice pack to break away, and thus our tape measurement did not capture the full thickness of the ice. Nonetheless, it can be observed that there is a good fit between the measured and theoretical values of time delays as a function of incidence angle, and the time delay decreases with increasing incidence angle, as it is expected using (2.4).

Figure 3.34 also shows the value of zero-padding in post-processing. The ACF was created by zero-padding the spectrum up to $N_f + N_z = 2^{14}$, resulting in a temporal precision of 0.01 ns. In the absence of zero-padding, the data would have been rounded to the nearest $1/F_s = 0.33$ ns. At this coarse precision, the angular dependence of the delay would be barely visible.

The most obvious outlier in Fig. 3.34, at 31°, corresponds to the measurement with lowest delayed peak magnitude in Fig. 3.16, and so suffers from a low signal to noise ratio, and is thus affected by the sidelobes of the peak at $\tau = 0$. As the null to null width of a sidelobe is $\frac{1}{F_s}$, the largest deviation expected is $\frac{1}{2F_s} \approx 0.16$ ns, and this peaks differs from the best-fit curve by about 0.10 ns.

Finally, Fig. 3.34 supports the prediction of (2.4) for the angular dependence of the retrieved time delays of lake icepack using WiBAR. For this icepack, the WiBAR accuracy is within 2 cm of the manually measured pack thickness.

Other measurements were also done at single incident angles at Argo Pond and Barton Dam in Ann Arbor, MI, and South Sturgeon Lake in northern Minnesota. These measurements were conducted using the second version of X-band WiBAR, as explained in Section 3.2.1.2. All the measured time delays by WiBAR for a single layer of lake icepack and a lake icepack with dry snow cover at all incident angles are shown in Figures 3.35 and 3.36, respectively. The root mean squared error (RMSE) of the measured time delay by WiBAR is about 0.09 ns and 0.1 ns for bare ice and ice with dry snow cover, respectively. It can be observed that the presence of a dry snow cover can affect the ability of WiBAR in accurately measuring the ice thickness. The thinner the ice, the worse this effect would be, as discussed in Section 3.2.5.1.

3.5.2 Non-destructive Dielectric Measurement of a Single Layer of Ice

Using the results from the field measurement campaign explained in 3.5.1, the dielectric constant and thickness of the icepack can be directly found, as explained in Section 3.3. The ACF at two different incident angles $\theta_1 = 0.9°$ and $\theta_2 = 59.1°$, obtained from the measured spectra after calibration [57], using the Hamming window function is shown in Fig. 3.37. The measured time delays are $\tau_1 = 4.35$ ns and $\tau_2 = 3.83$ ns at $\theta_1 = 0.9°$ and $\theta_2 = 59.1°$, respectively. Using (3.48), the measured dielectric constant and thickness of the icepack are $\epsilon_p = 3.24$ and $d_p = 36.24$ cm,

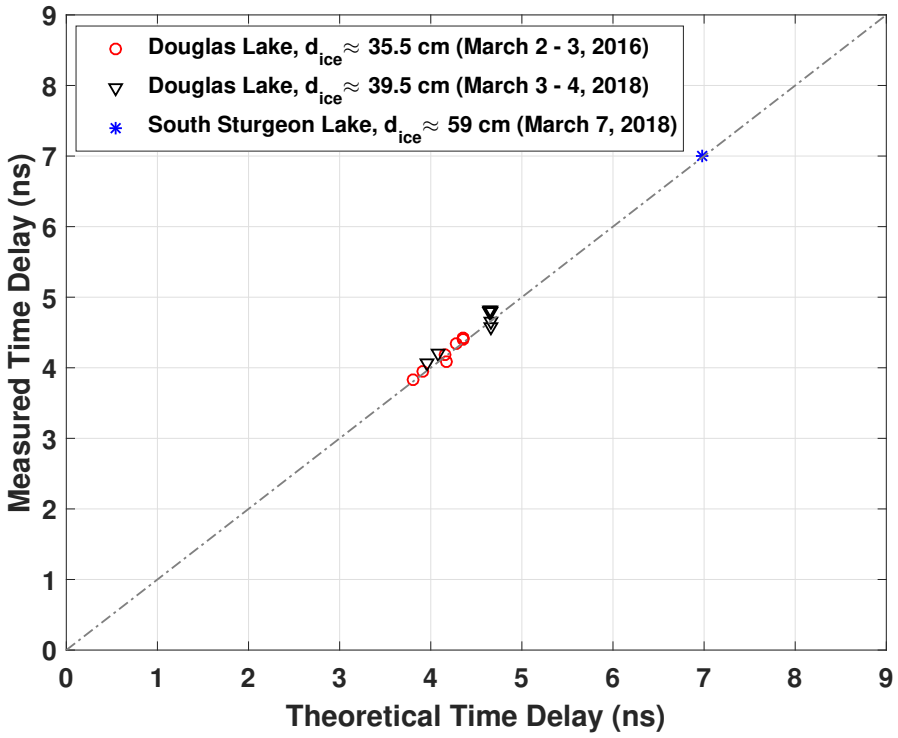

Figure 3.35: WiBAR measurement at all incident angles of bare lake icepacks at different lakes. The RMSE is about 0.09 ns.

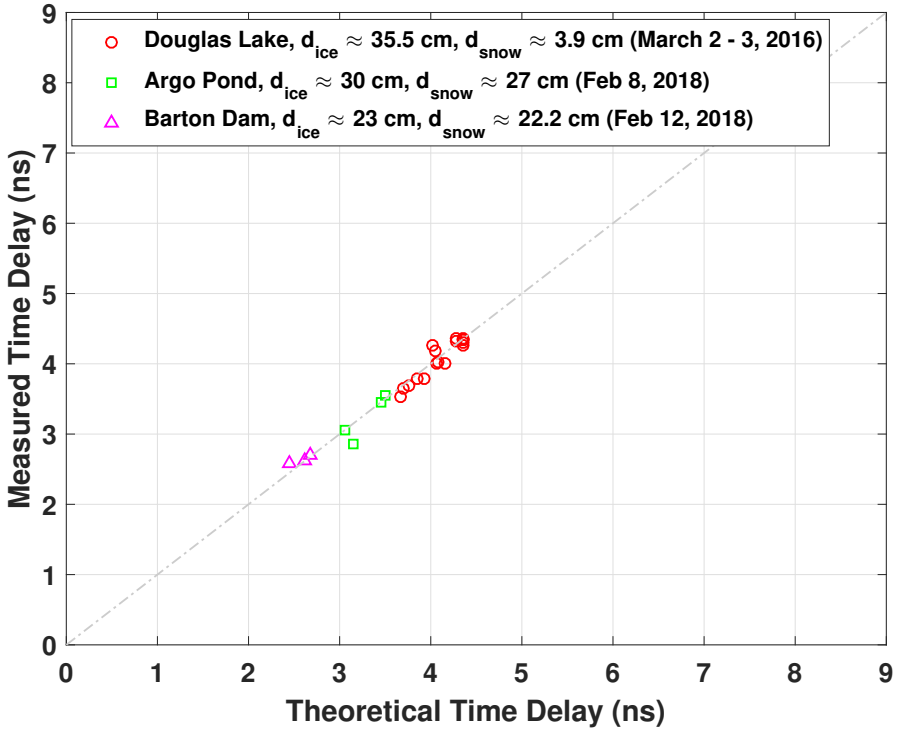

Figure 3.36: WiBAR measurement at all incident angles of lake icepacks with dry snow covers at different lakes. The RMSE is about 0.1 ns.

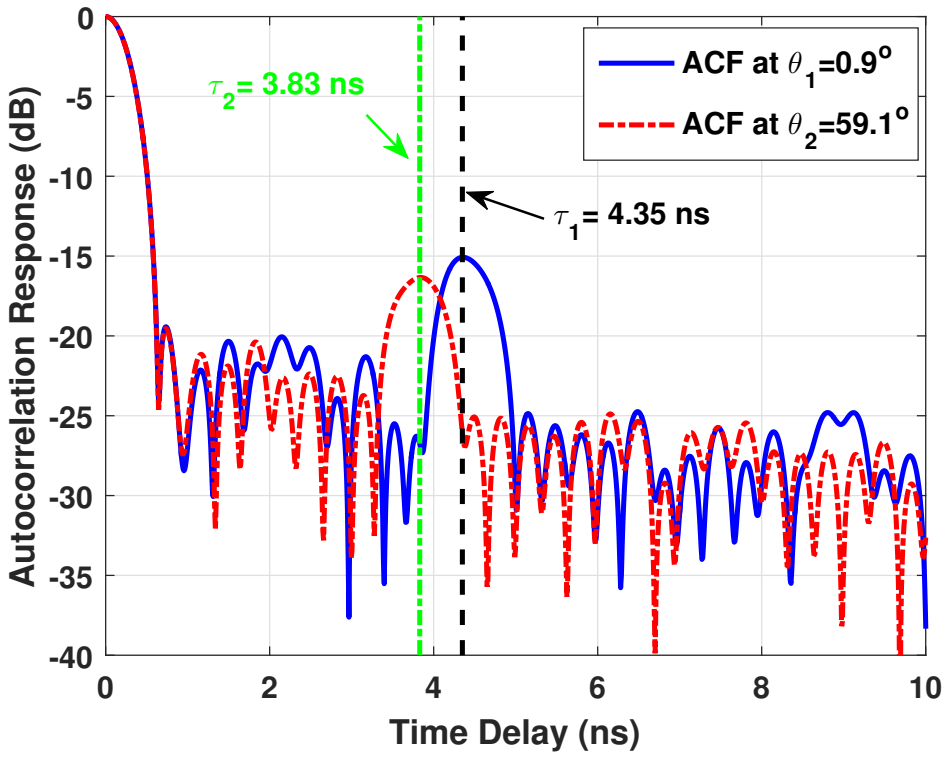

Figure 3.37: The autocorrelation function of the lake icepack measured at $\theta_1 = 0.9°$ (blue solid line) and $\theta_2 = 59.1°$ (red dashed line) on Douglas Lake on March 02, 2016. The Hamming window was used.

respectively. The measured thickness is less than 1 cm different from the ground truth value of the icepack thickness ($\frac{\delta d}{d} \approx 2\%$). In addition, the refractive index of the freshwater icepack found using this technique is about 0.09 higher than the reported value of 3.15 over microwave frequencies by Evans [17] and 0.06 higher than the reported value by Matzler and Wegmuller [51].

3.5.3 Two Layer Media of Ice with Snow Cover

A snow-covered lake icepack on Lake Douglas at the University of Michigan Biological Station (UMBS) was measured as part of the same campaign as reported in Section 3.5.1 and [57]. The H-pol measurements were made by a 7-10 GHz WiBAR instrument with $N_{ind} = 3 \times 10^5$ [57]. At these frequencies the ice and snow typically have negligible volume and surface scattering. The lake ice observations by WiBAR

were made from about 11:00 am until around 1:00 pm on March 03, 2016. The air temperature was about -6°C and -3°C at 11:00 am and 1:00 pm, respectively. The ground truth measurements of ice and snow thicknesses were done with a tape measure at the conclusion of the WiBAR measurements. The ground truth values of ice and snow thicknesses are 35.5 cm and 3.9 cm, respectively. The snow was dry, and its density was about $\rho_s = 210$ kg/m^3.

Among the measurements at different incidence angles, only the one at the largest incidence angle, 69.4°, showed distiction between the two layers in the ACF. The autocorrelation response obtained from the measured emissivity spectra after calibration [57] using both rectangular and Hamming window functions is shown in Fig. 3.38. The peaks in the ACF near 4 ns are considered detected because they rise at least two standard deviations above the expectation of the ACF in the absence of a slab. Figure 3.20 shows that the ice peak is only slightly stronger than the sum peak at this incidence angle. The two delay peaks related to the ice thickness at $\tau_{ice} = 3.56$ ns and the sum of the ice and the snow thicknesses at $\tau_{ice} + \tau_{snow} = 3.77$ ns are almost resolvable using the rectangular window (corresponding to $d_{ice} = 35.4$ cm, $d_{snow} = 4.3$ cm) while only one peak related to the ice thickness is resolved at $\tau_{ice} = 3.66$ ns using Hamming window (corresponding to $d_{ice} = 36.4$ cm). There is about 0.1 ns (1 cm) difference between the τ_{ice} (d_{ice}) detected using rectangular and Hamming window functions. This difference is due to bias of the position of the detected peak, as explained in Section 3.2.5.1.

The next terms of the Taylor expansion in (3.44) can also be observed. The delay peaks at $2\tau_{ice} = 7.24$ ns and $2(\tau_{ice} + \tau_{snow}) = 7.74$ ns are detected using the Hamming window function, and from these, the snow thickness is inferred to be about 5.1 cm. This value is about 0.8 cm larger than the snow thickness measured using rectangular window function. This difference is due to the leakage of the side lobes of the two close delay peaks since the ratio of the peak amplitude to sidelobe level is lower. In

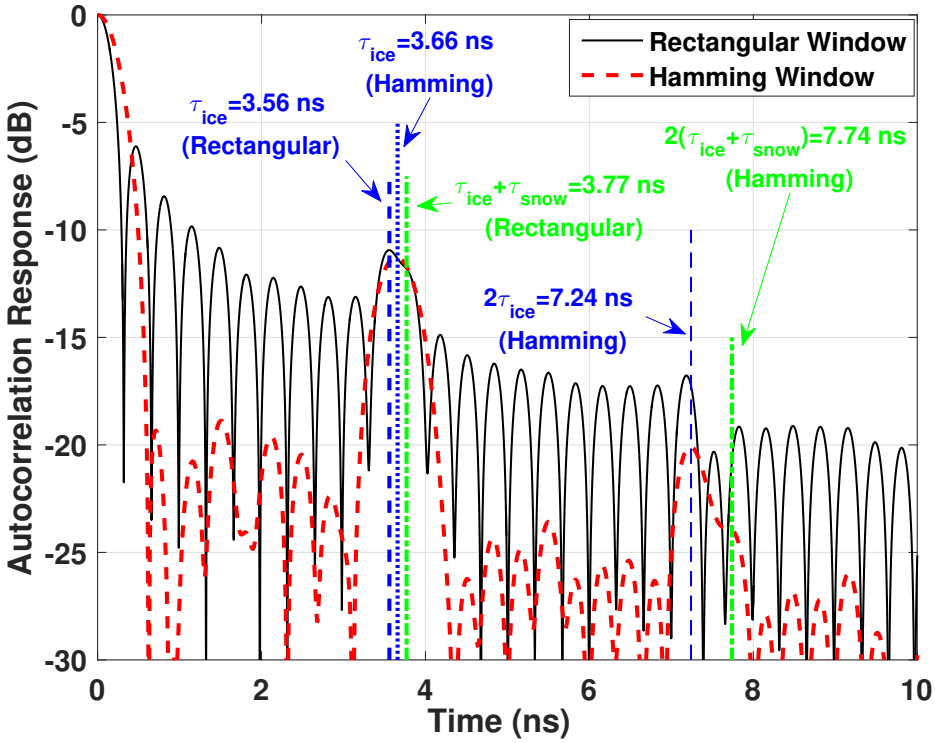

Figure 3.38: The autocorrelation function of the lake icepack with top dry snowpack measured on Douglas Lake on March 03, 2016 ($\theta = 69.4°$, $d_{ice} = 35.5$ cm, $d_{snow} = 3.9$ cm, $\rho_s = 210$ kg/m^3).

contrast, the rectangular window has such high sidelobes that these peaks cannot be detected.

3.5.4 Single Layer Media with Thickness Variation within a Footprint of the Radiometer's Antenna

Field measurements for lake icepack with thickness variation were conducted on Douglas Lake at the University of Michigan Biological Station (UMBS) on March 03 and 04, 2018. The surface of the lake ice was snow ice as the snow had melted in the warm weather the week before our measurements and refroze. There was no snow on the ice. The measurements were conducted in H-pol using the second version of the X-band WiBAR instrument, shown in Fig. 3.5. This instrument was explained in Section 3.2.1.2. For the ground truth measurement, a tape measure was used after

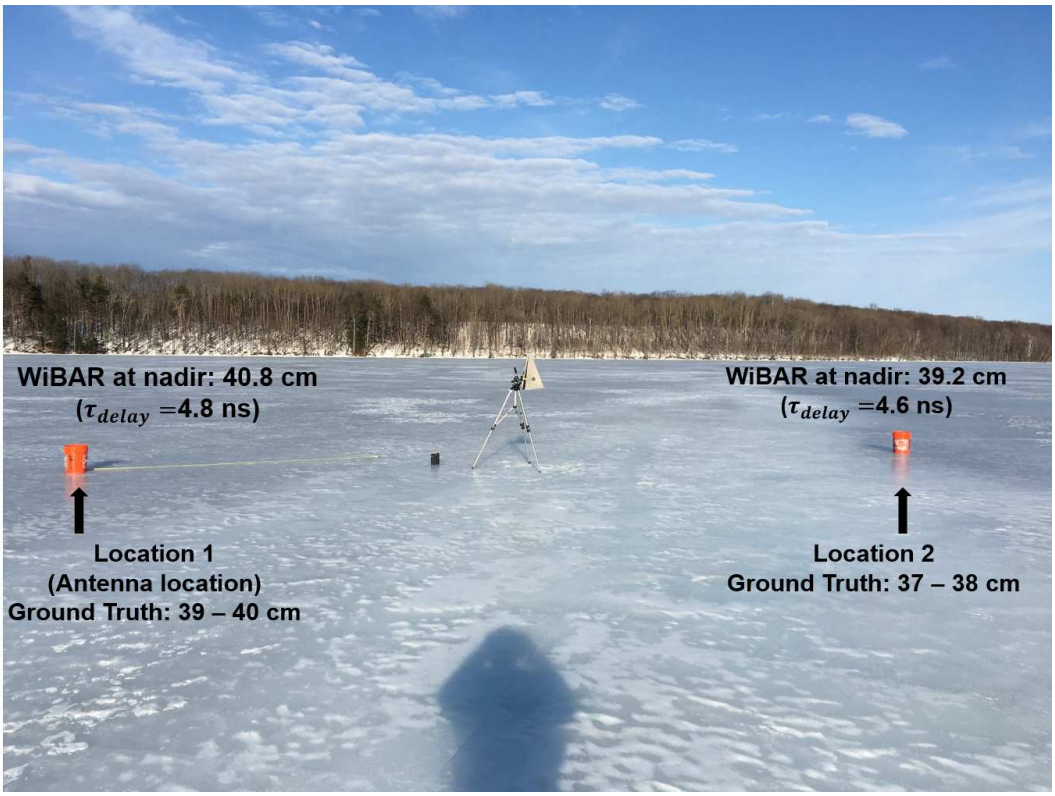

Figure 3.39: A side-view of the measurement location. The WiBAR was located at location 1 where we were able to measure the sub-pixel variability at $\theta_0 = 70°$. The center of the footprint is at the center of the photo.

hand-coring the ice at the conclusion of the WiBAR measurements. The ground truth value of the icepack thickness at the antenna's location (location 1 in Fig. 3.39) was about 39-40 cm, while it was about 37-38 cm at about 10 m away from the antenna (location 2). The antenna height was 135 cm at its pivot point, and the incident angle for the measurement exhibiting multiple thicknesses was 70°.

To calibrate, measurements of the sky (approximating $e = 0$) and a matched load ($e \sim 1$) were also conducted. These measurements were then used to extract the spectra of emissivity using the calibration method explained in [57] with one additional step: because the resolution bandwidth (RBW) on the spectrum analyzer is limited to a maximum of 250 kHz, we averaged adjacent spectral power points together to create an effective RBW of 27.5 MHz. The sky, matched load, and lake ice power spectra are shown in Fig. 3.40. The lake ice observation at incidence angle of

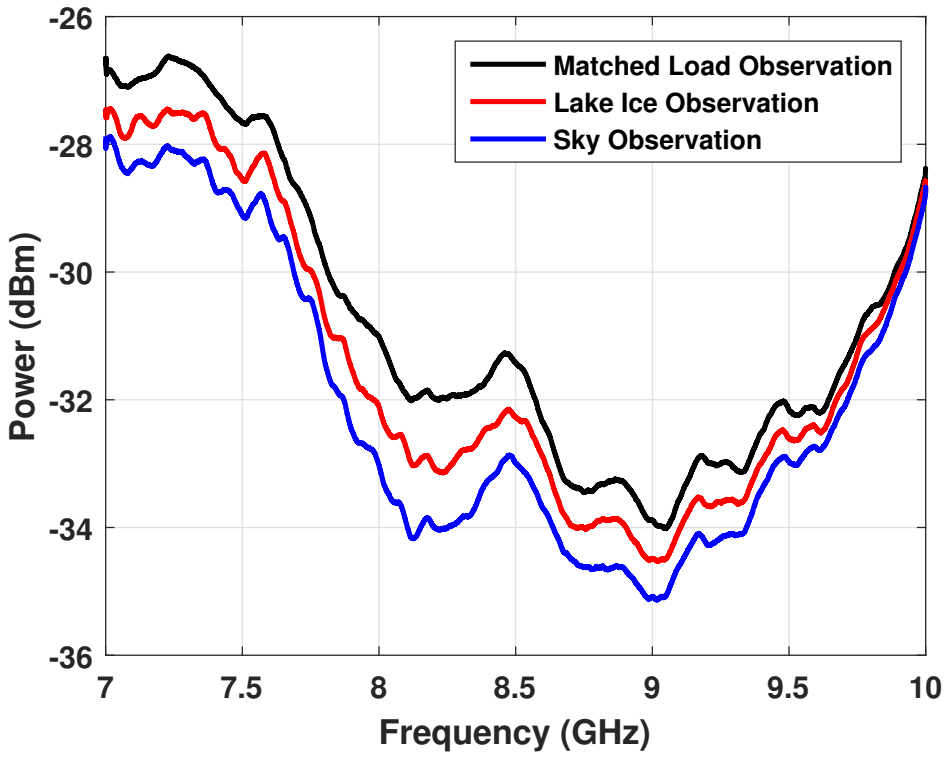

Figure 3.40: Matched load, lake ice, and sky observations on Douglas Lake on March 03, 2018 ($\theta_0 = 70°$, $d_{ice} \approx 40$ cm).

70° was made at about 10:00 am on March 03, 2018, and the sky measurements were made around noon. The physical temperature of the matched load was not monitored, but is assumed to be near the air temperature, which was about −7.0°C and −0.8°C at 9:28 am and 11:41 am, respectively. The extracted emissivity of the lake icepack observation in Fig. 3.40 is shown in Fig. 3.41. Despite the low responsivity of the instrument near 10 GHz, resulting in the non-physical values of the emissivity, we used the entire spectrum to preserve temporal resolution.

The ACF is obtained from the inverse Fourier transform of the emissivity spectra. Then the time delay is found from the local maxima of the ACF of the measured lake icepack. The autocorrelation response of the emissivity in Fig. 3.31 using both the rectangular and the Hamming windows are shown in Fig. 3.32. There are two peaks in the ACF using the rectangular window corresponding to 38.5 cm and 42.2 cm

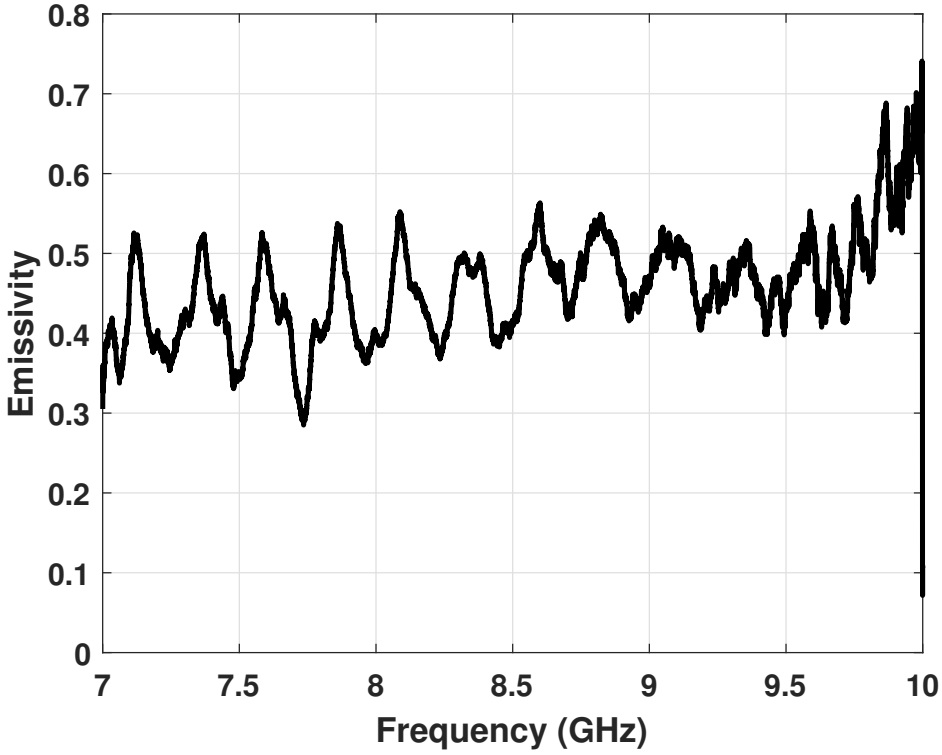

Figure 3.41: The spectral emissivity derived from the power spectra in the previous Figure.

icepack, while there is only one broad peak in the ACF using the Hamming window corresponding to about 40.5 cm due to the resolution limit of the Hamming window [54]. In the ACF using the Hamming window, the minimum WiBAR resolution is about $\frac{2}{F_s} \approx 0.6$ ns, and only one peak is resolved at the crossover point of the two peaks from the rectangular window. However, the position in time and amplitude of the delay peaks in the ACF using the rectangular window are biased due to the sidelobe leakage of zero delay and the adjacent peak [54], and, as a result, the measured thicknesses by the WiBAR are off by about 2 cm from the ground truth values. Even though the amplitude difference of the two delay peaks in Fig. 3.32 is not large ($|\Delta A| = 1.49$ dB), biases could be also due to the different a_{ij} values for each sub-pixel for which we do not have measurements. We also used our WiBAR instrument the next day on March 04, 2018 to measure the ice thickness at locations 1 and 2 at nadir in order to confirm the validity of the measured value by the WiBAR. The nadir measurements have much smaller footprints than that at 70°, so the likelihood of a uniform target is higher. These measured ice thicknesses at location 1 and 2 are 40.8 cm ($\tau_{delay} = 4.8$ ns) and 39.2 cm ($\tau_{delay} = 4.6$ ns), respectively, as shown in Fig. 3.39.

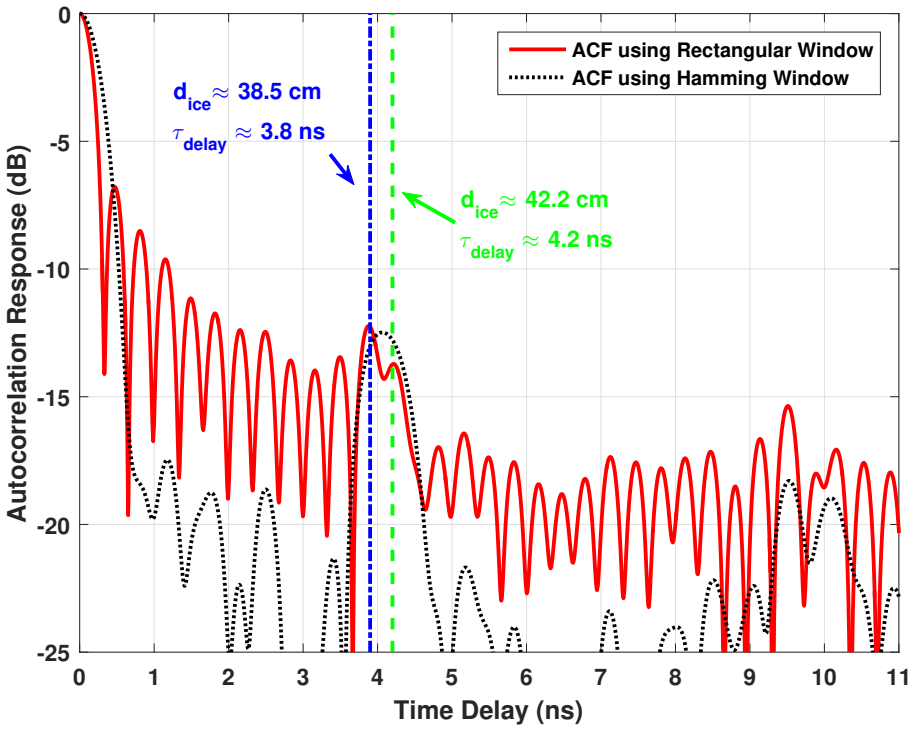

Figure 3.42: The autocorrelation function of the lake icepack measured on Douglas Lake on March 03, 2018 using the rectangular window (red solid line) and the Hamming window (black dotted line). The antenna was at location 1. Two peaks are detected at 38.5 cm and 42.2 cm in the ACF using the rectangular window, while only one peak is detected at about 40.0 cm using the Hamming window ($\theta_0 = 70°$).

CHAPTER IV

Error Analysis of the Measured Time Delay Using Wideband Autocorrelation Radiometry

4.1 Introduction

Detection and frequency (time) estimation of sinusoidal signals from a limited number of noisy discrete time measurements have application in many fields, such as moving target detection in radars [72]. A direct method for frequency (time) detection is the standard inverse discrete Fourier transform (IDFT). The error in the measured pack thickness by WiBAR stems from the error in the measured time delay using the IDFT. In this chapter, we want to investigate the root mean square time delay error (RMSTDE) using the IDFT approach.

The most useful approach in comparing the performance of any unbiased estimator is by placing a lower bound on the variance of the estimator. This approach will allow us to claim that an estimator is the minimum-variance unbiased (MVU) estimator. Even if the desired unbiased estimator does not reach the minimum variance bound, it provides a benchmark to analyze the performance of the unbiased estimator. There are many such variance bounds [52, 40, 78, 95], but the easiest one to determine is the Cramer-Rao lower bound (CRLB) [38]. Since the time delay estimation using IDFT is a nonlinear problem, it will only reach the CRLB for signal to noise ratios (SNRs)

higher than a threshold value. It is shown that the Hamming window works better compared to the rectangular window in terms of having the variance closer to the CRLB. It is also shown that the variance of the measured thickness is very high near the Brewster angle.

4.2 Error Analysis of the Measured Time Delay by WiBAR

4.2.1 Single Layer Media

We first start with the simple single layer media and used the approximated emissivity expression, as given by [57]

$$e(f) \approx \bar{e}\,(1 - 2A_e \cos(2\pi f \tau_{delay})) \tag{4.1}$$

where $\bar{e}$ is the mean emissivity over frequency, A_e is one half of the amplitude of the ripple in the emissivity as a function of frequency, τ_{delay} is the microwave propagation time difference of multipath microwave emission from a pack with the thickness of d [57]. We can rewrite (4.1) with the added white Gaussian noise (AWGN), $w[n]$, with zero mean and variance of σ_w^2, as given by

$$e[n] \approx \bar{e}\,(1 - 2A_e \cos[2\pi \mathrm{T}_{delay} n]) + w[n] \tag{4.2}$$

where $n = 0, 1, 2, \cdots, N-1$, and N is the number of frequency (data) points. For simplicity, it is assumed that T_{delay}, which is the normalized time delay bin number, varies between 0 and 0.5 such that $\mathrm{T}_{delay} = k_0/N$ where $k_0 \in \{0, 1, 2, \cdots, N/2 - 1\}$. Using equations (4.1) and (4.2), it can be observed that $f\tau_{delay} = \mathrm{T}_{delay} n$, where $f = (F_s/N)\, n$, $\tau_{delay} = k_0/F_s$, and F_s is the total bandwidth of operation. Throughout

this chapter, we used the upper case, T_{delay}, for the time delay bin number notation so that it can be distinguishable from the actual time delay τ_{delay} in seconds.

We now need to find a lower bound on the variance of the unbiased estimator using the IDFT approach. As discussed, the CRLB is the easiset to determine and is given by [38]

$$Var(\hat{\chi}_i) \geq \left[I^{-1}(\chi)\right]_{ii} \tag{4.3}$$

where χ is the vector of p unknowns such as τ_{delay}, $\bar{e}$, A_e, etc., and $I(\chi)$ is the $p \times p$ Fisher information matrix, as given by

$$[I(\chi)]_{ij} = -E\left[\frac{\partial^2 \ln \rho(e;\chi)}{\partial\chi_i \partial\chi_j}\right] \tag{4.4}$$

where $i = 1, 2, ..., p$, $j = 1, 2, ..., p$, $\rho(e;\chi)$ is the probability density function (PDF) of the measured data, E is the exepected value, and p is the number of unknowns. In the scalar case, $p = 1$, and the CRLB would be scalar. An unbiased estimator may be found that attains the CRLB if and only if [38]

$$\frac{\partial \ln \rho(e;\chi)}{\partial\chi} = I(\chi)\left(g(e) - \chi\right) \tag{4.5}$$

for some p-dimensional function g, and some $p \times p$ matrix I. That estimator, which is the minimum-variance unbiased estimator (MVU), is $\hat{\chi} = g(e)$, and its covariance matrix is $I^{-1}(\chi)$.

Since it is common to assume signals in white Gaussian noise (WGN), it is worthwhile to derive the CRLB for this case, as given by [38]

$$[I(\chi)]_{ij} = \frac{1}{\sigma_w^2} \sum_{n=0}^{N-1} \frac{\partial s[n;\chi]}{\partial \chi_i} \frac{\partial s[n;\chi]}{\partial \chi_j} \tag{4.6}$$

where $s[n;\chi] = \bar{e}\,(1 - 2A_e \cos[2\pi \mathrm{T}_{delay} n])$ is the signal only part of total received signal with the WGN.

It is first assumed that A_e, $\bar{e}$, and T_{delay} are the unknown parameters to be estimated, so we need to find the CRLB for each of the unknown parameters A_e, $\bar{e}$, and T_{delay}. In evaluating the CRLB, it is assumed that T_{delay} is not near 0 or 1/2, which allows us to make certain simplifications based on the following approximations [83, 38]

$$\frac{1}{N^{i+1}} \sum_{n=0}^{N-1} n^i \sin(4\pi \mathrm{T}_{delay} n) \approx 0 \tag{4.7a}$$

$$\frac{1}{N^{i+1}} \sum_{n=0}^{N-1} n^i \cos(4\pi \mathrm{T}_{delay} n) \approx 0 \tag{4.7b}$$

for $i = 0, 1, 2$. Using these approximations, we can find the Fisher information matrix for the single layer media with unknown matrix $\chi = [\bar{e}, A_e, \mathrm{T}_{delay}]$, as given by

$$I(\chi) = \begin{bmatrix} \frac{N\left(1+2A_e^2\right)}{\sigma_w^2} & \frac{2NA_e\bar{e}}{\sigma_w^2} & 0 \\ \frac{2NA_e\bar{e}}{\sigma_w^2} & \frac{2N\bar{e}^2}{\sigma_w^2} & 0 \\ 0 & 0 & \frac{(4\pi A_e\bar{e})^2}{2\sigma_w^2} \sum_{n=0}^{N-1} n^2 \end{bmatrix} \tag{4.8}$$

Using the geometric series formulas, as given by (4.9), the inverse of the Fisher matrix, $I^{-1}(\chi)$, is given by (4.10). Hence, the CRLB for each unknowns are given by (4.11).

$$\sum_{n=0}^{N-1} n = \frac{N(N-1)}{2} \tag{4.9a}$$

$$\sum_{n=0}^{N-1} n^2 = \frac{N(N-1)(2N-1)}{6} \tag{4.9b}$$

$$I^{-1}(\chi) = \begin{bmatrix} \frac{\sigma_w^2}{N} & -\frac{A_e\sigma_w^2}{N\bar{e}} & 0 \\ -\frac{A_e\sigma_w^2}{N\bar{e}} & \frac{(1+2A_e^2)\sigma_w^2}{2N\bar{e}^2} & 0 \\ 0 & 0 & \frac{3\sigma_w^2}{(2\pi A_e\bar{e})^2 N(N-1)(2N-1)} \end{bmatrix} \tag{4.10}$$

$$Var(\hat{\bar{e}}) \geq \frac{\sigma_w^2}{N} \tag{4.11a}$$

$$Var(\hat{A}_e) \geq \frac{(1+2A_e^2)\sigma_w^2}{2N\bar{e}^2} \tag{4.11b}$$

$$Var(\hat{\mathrm{T}}_{delay}) \geq \frac{3\sigma_w^2}{(2\pi A_e\bar{e})^2 N(N-1)(2N-1)} \tag{4.11c}$$

It is now assumed that the the mean of the emissivity, $\bar{e}$ is known, and A_e and T_{delay} are the only unknowns. In this case, the 2×2 Fisher information matrix and its inverse are given by (4.12) and (4.13), respectively. Hence, the CRLB for each of the unknowns are given by (4.14).

$$I(\chi) = \begin{bmatrix} \frac{2N\bar{e}^2}{\sigma_w^2} & 0 \\ 0 & \frac{(4\pi A_e\bar{e})^2}{2\sigma_w^2}\sum_{n=0}^{N-1} n^2 \end{bmatrix} \tag{4.12}$$

$$I^{-1}(\chi) = \begin{bmatrix} \frac{\sigma_w^2}{2N\bar{e}^2} & 0 \\ 0 & \frac{3\sigma_w^2}{(2\pi A_e \bar{e})^2 N(N-1)(2N-1)} \end{bmatrix} \tag{4.13}$$

$$Var(\hat{A}_e) \geq \frac{\sigma_w^2}{2N\bar{e}^2} \tag{4.14a}$$

$$Var(\hat{\mathrm{T}}_{delay}) \geq \frac{3\sigma_w^2}{(2\pi A_e \bar{e})^2 N(N-1)(2N-1)} \tag{4.14b}$$

If T_{delay} is the only unknown, $I(\chi)$ would be scalar and is given by (4.15). The CRLB for the unknown parameter, τ_{delay}, is given by (4.16).

$$I(\chi) = \frac{(4\pi A_e \bar{e})^2}{2\sigma_w^2} \sum_{n=0}^{N-1} n^2 \tag{4.15}$$

$$Var(\hat{\mathrm{T}}_{delay}) \geq \frac{3\sigma_w^2}{(2\pi A_e \bar{e})^2 N(N-1)(2N-1)} \tag{4.16}$$

So far, we have found the lower bound on the variance, CRLB, of an unbiased estimator. We have to examine whether a time delay estimator exists, which is unbiased and attains the CRLB. Such estimator is the minimum-variance unbiased (MVU) estimator and should satisfy (4.5). Using (4.2) with assumption of A_e and $\bar{e}$ being known for simplicity, the PDF of the data is given by

$$\rho(e;\chi) = \frac{1}{(2\pi\sigma_w^2)^{N/2}} \exp\left\{ -\frac{1}{2\sigma_w^2} \sum_{n=0}^{N-1} [e[n] - \bar{e} + 2A_e \bar{e} \cos(2\pi n \mathrm{T}_{delay})]^2 \right\} \tag{4.17}$$

The natural logarithm of (4.17) and the derivative of its natural logarithm are given by

$$\ln \rho(e;\chi) \quad = -\ln(2\pi\sigma_w^2)^{\frac{N}{2}} - \frac{1}{2\sigma_w^2}\sum_{n=0}^{N-1}\left[e[n] - \bar{e} + 2A_e\bar{e}\cos(2\pi n \mathrm{T}_{delay})\right]^2 \tag{4.18a}$$

$$\frac{\partial \ln \rho(e;\chi)}{\partial \mathrm{T}_{delay}} = \frac{4\pi A_e\bar{e}}{\sigma_w^2}\sum_{n=0}^{N-1} n\sin(2\pi n \mathrm{T}_{delay})\left[e[n] - \bar{e} + 2A_e\bar{e}\cos(2\pi n \mathrm{T}_{delay})\right] \tag{4.18b}$$

The direct method for time delay detection is the IDFT approach, as given by

$$\hat{\mathrm{T}}_{delay} = \arg\max\left\{S[k]\right\}, \quad \text{for} \quad N/2 > k > 0 \tag{4.19}$$

where $S[k]$ is the IDFT formula, as given by

$$S[k] = \frac{1}{N}\sum_{n=0}^{N-1} e[n]\exp\left(i\frac{2\pi}{N}kn\right) \tag{4.20}$$

It can be observed that the IDFT estimator does not satisfy (4.5), so it's not a MVU estimator.

Now, let's find the false alarm rate, P_{FA}, and the probability of detection, P_D, using the IDFT approach. Given the received data $e[n]$, a decision has to be made between the two following hypothesis

$$H_0 : e[n] = \bar{e}_0 + w[n], \qquad n = 0, 1, \ldots, N-1 \tag{4.21a}$$

$$H_1 : e[n] = (\bar{e} - 2A_e\bar{e}\cos(2\pi n \mathrm{T}_{delay})) + w[n] \tag{4.21b}$$

The first hypothesis H_0 assumes that $e[n]$ consists only of noise with a constant value of the emissivity, $\bar{e}_0$, while in H_1 the sinusoidal signal is persumed to be present. The goal is to find the $P_{FA} = P(D_1|H_0)$ and the $P_D = P(D_1|H_1)$, where D_1 is the decision

of hypothesis H_1. Denote the auto-correlation function (ACF) coefficients at $\mathrm{T} = \frac{k}{N}$ for the noise only case and the signal present case by $S_{e_0}(k)$ and $S_{e_1}(k)$, respectively. The value of $S_{e_1}(k_0)$ at the $\mathrm{T}_{delay} = \frac{k_0}{N}$ is computed as

$$S_{e_1}(k_0) = \sqrt{a^2 + b^2} \tag{4.22}$$

where

$$a \triangleq \frac{1}{N} \sum_{n=0}^{N-1} (\bar{e} - 2A_e \bar{e} \cos(2\pi n \mathrm{T}_{delay}) + w[n]) \cos\left(\frac{2\pi n k_0}{N}\right) \tag{4.23a}$$

$$b \triangleq \frac{1}{N} \sum_{n=0}^{N-1} (\bar{e} - 2A_e \bar{e} \cos(2\pi n \mathrm{T}_{delay}) + w[n]) \sin\left(\frac{2\pi n k_0}{N}\right) \tag{4.23b}$$

where a and b are Gaussian random variables. They are independent and of identical variances of $\sigma^2 = \frac{\sigma_w^2}{2}$, where σ_w^2 is the power of the noise $w[n]$. Using [69], the PDF of $S_{e_1}(k_0)$ can be found, as given by

$$\rho_s(u) = \frac{u}{\sigma^2} \exp\left(-\frac{s^2 + u^2}{2\sigma^2}\right) I_0\left(\frac{us}{\sigma^2}\right) \tag{4.24}$$

which is a Ricean-distributed random variable. The quantity s equals the square root of the sum of the mean square of a and b, that is, $s = \sqrt{2} A_e \bar{e}$, and I_0 is the modified Bessel function of the first kind of order zero.

Similarly, it can be shown that the remaining $S_{e_1}(k)$ and all the $S_{e_0}(k)$ are all of Rayleigh distribution, as given by

$$\rho_w(u) = \frac{u}{\sigma^2} \exp\left(-\frac{u^2}{2\sigma^2}\right) \tag{4.25}$$

The expressions similar to (4.24) and (4.25) can be found in [73, 80].

Assuming that the IDFT coefficients are independent which is valid when the

time-bandwidth product of the signal is sufficiently large, then P_{FA} is calculated as

$$\begin{aligned} P_{FA} &= 1 - \left[\int_0^{V_T} \rho_w(u) du \right]^{(\frac{N}{2})-1} \\ &= 1 - \left(1 - \exp\left(-\frac{V_T^2}{2\sigma^2} \right) \right)^{(\frac{N}{2})-1} \end{aligned} \tag{4.26}$$

where V_T is a threshold value of the ACF coefficient, which is set by the user. The probability of detection is also derived as

$$\begin{aligned} P_D &= 1 - \left[\int_0^{V_T} \rho_w(u) du \right]^{(\frac{N}{2})-2} \int_0^{V_T} \rho_s(u) du \\ &= 1 - \left(1 - \exp\left(-\frac{V_T^2}{2\sigma^2} \right) \right)^{(\frac{N}{2})-2} \left(1 - Q_1\left(\frac{s}{\sigma}, \frac{V_T}{\sigma} \right) \right) \end{aligned} \tag{4.27}$$

where Q is the Marcum Q-function [32], as given by

$$Q_M(\alpha, \beta) = \frac{1}{\alpha^{M-1}} \int_\beta^\infty x^M \exp\left(-\frac{x^2 + \alpha^2}{2} \right) I_{M-1}(\alpha x)\, dx \tag{4.28}$$

It also has the series form, as given by

$$Q_M(\alpha, \beta) = \exp\left(-\frac{\alpha^2 + \beta^2}{2} \right) \sum_{k=1-M}^{\infty} \left(\frac{\alpha}{\beta} \right)^k I_k(\alpha\beta) \tag{4.29}$$

where in our case, $M = 1$, $\alpha = \frac{s}{\sigma}$, and $\beta = \frac{V_T}{\sigma}$.

In the time delay estimation problem, when the hypothesis H_1 is chosen, we need to estimate the T_{delay}. The maximum likelihood time delay estimation of a pure sinusoid is given by the location of the peak of the ACF, and this estimator reaches the CRLB for this time delay, as given by (4.30), when $SNR = (\sqrt{2} A_e \bar{e})/\sigma_w$ is greater than some threshold value. We will show this threshold value for an example after

we derive the RMSTDE in the following.

$$Var_{\mathrm{T}_{delay}}(N) = \frac{3}{2\pi^2 N(N-1)(2N-1)SNR^2} \tag{4.30}$$

If $\mathrm{T}_{delay} = \frac{k_0}{N}$, the probability of occurrence of an anomaly in the IDFT is given by

$$\begin{aligned} q &= P\Big(S_{e_1}(k_0) \leq \text{at least one of the } S_{e_1}(1)S_{e_1}(2), \ldots, S_{e_1}(k_0-1), S_{e_1}(k_0+1), \\ &\qquad \ldots, S_{e_1}(N/2-1)\Big) \\ &= \int_0^\infty P\left(S_{e_1}(k_0) = u\right) \cdot \left[1 - \prod_{k=1, k\neq k_0}^{\left(\frac{N}{2}\right)-1} P\left(S_{e_1}(k) < u\right)\right] du \\ &= \int_0^\infty \rho_s(u) \left[1 - \prod_{k=1, k\neq k_0}^{\left(\frac{N}{2}\right)-1} \int_0^u \rho_w(\nu) d\nu\right] du \end{aligned} \tag{4.31}$$

which must be computed numerically. Assuming that the anomaly estimate is uniformly distributed between 0 and 0.5, the overall RMSTDE using the IDFT estimator is given by

$$\mathrm{RMSTDE} = \sqrt{(1-q)\, Var_{\mathrm{T}_{delay}}(N) + q \int_0^{0.5} 2\left(u - \mathrm{T}_{delay}\right)^2 du} \tag{4.32}$$

The RMSTDE for an icepack at nadir incidence angle and the CRLB as a function of SNR is shown in Fig. 4.1. The bandwidth is 3 GHz, $N = 461$, and $d_{ice} = 40$ cm. The measured time delay at nadir for an icepack with a constant refractive index of $n_{ice} = \sqrt{3.15}$ would be $\tau_{delay} = 4.73$ ns. It can be observed that at SNR$\geq$ 9 dB, the IDFT's RMSTDE meets the CRLB. The RMSTDE in IDFT using both the Hamming

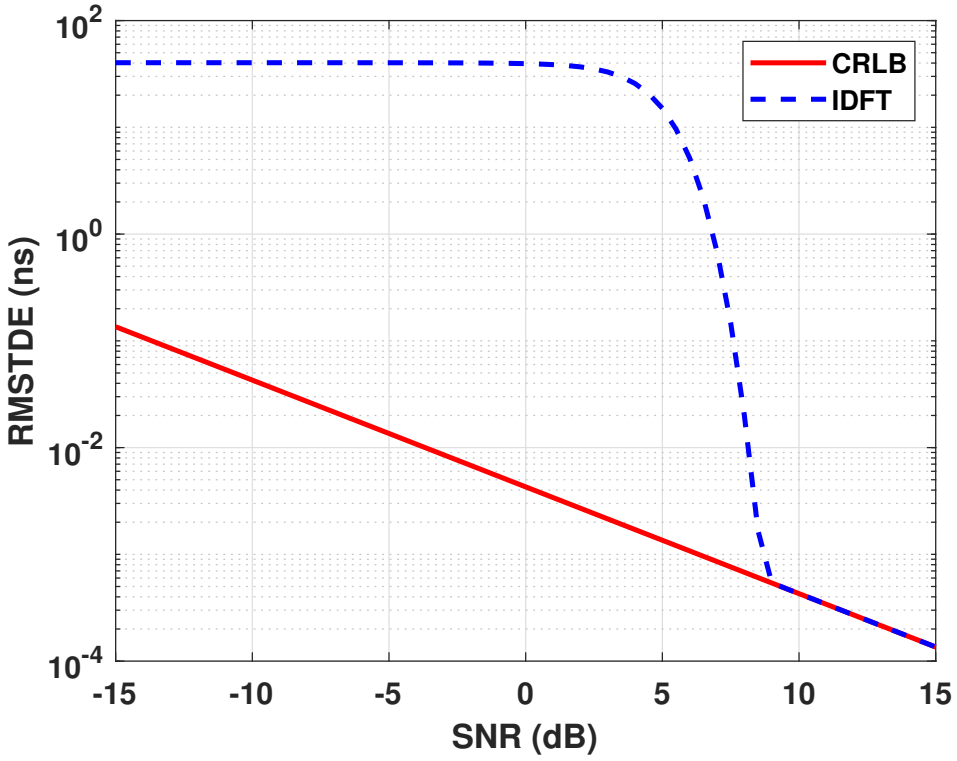

Figure 4.1: Theoretical root mean square time delay error (RMSTDE) of IDFT for a 40 cm icepack with respect to SNR of the delay peak. The CRLB is also shown in the figure for comparison. The bandwidth is 3 GHz with $N = 461$, and the incidence angle is $\theta = 0^\circ$ ($\tau_{delay} = 4.73$ ns).

and rectangular windows are shown in Figures 4.2(a) and 4.2(b), respectively. The RMSTDE meets the CRLB using Hamming window in H-pol for most of the incidence angles. In V-pol RMSTDE gets larger, mostly around the Brewster angles. On the other hand, RMSTDE does not meet the CRLB using the rectangular window. The SNR of the delay peak using the Hamming and rectangular windows are also shown Fig. 4.3.

So far, we have assumed the noise floor of the ACF is a constant value of the first side lobe level (FSLL). In reality, any window function has some roll-off for the side lobe levels. Assuming this, we can take into account the effect of the location of the delay peak with respect to the other peaks. It can be shown that the side lobe level

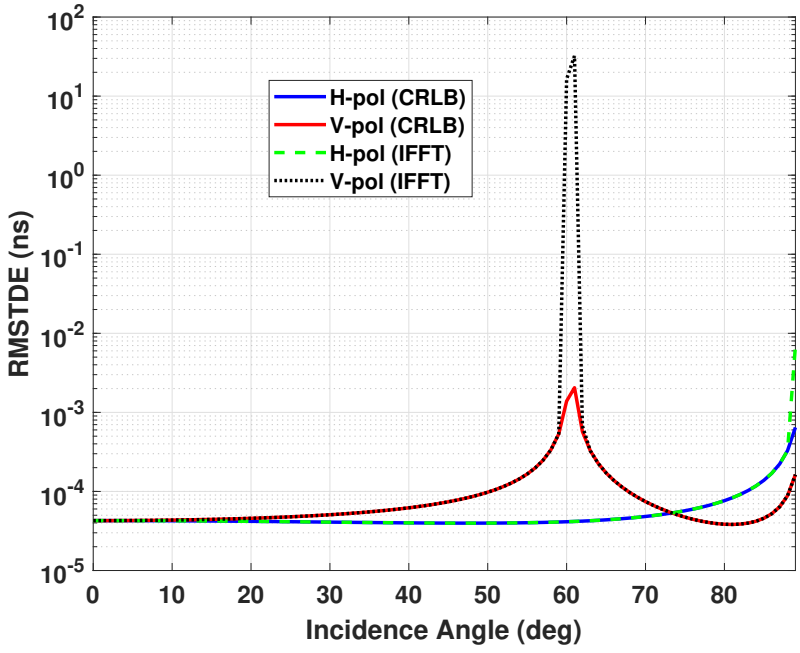

(a)

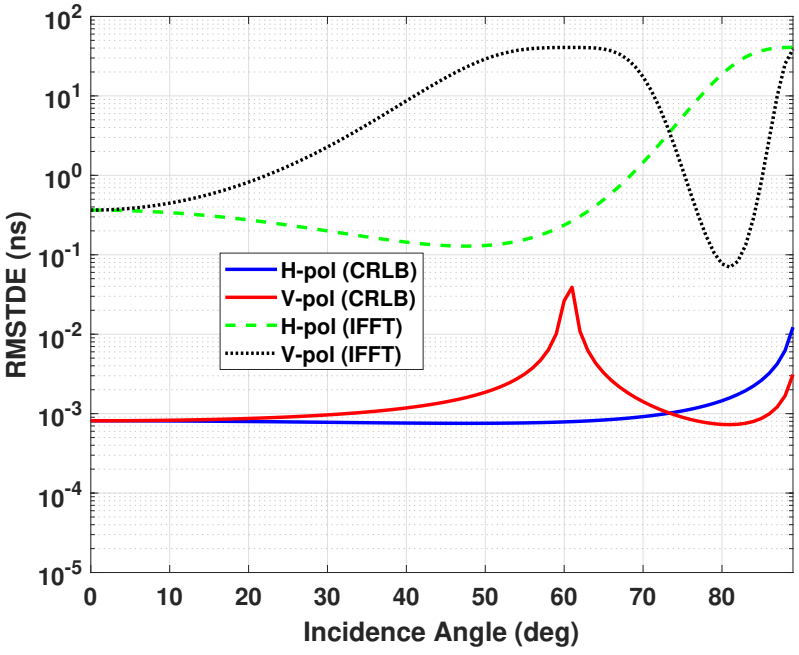

(b)

Figure 4.2: The root mean square time delay error (RMSTDE) of IDFT using both (a) the Hamming and (b) the rectangular window as a function of incidence. The bandwidth is 3 GHz with $N = 461$, and $d_{ice} = 40$ cm.

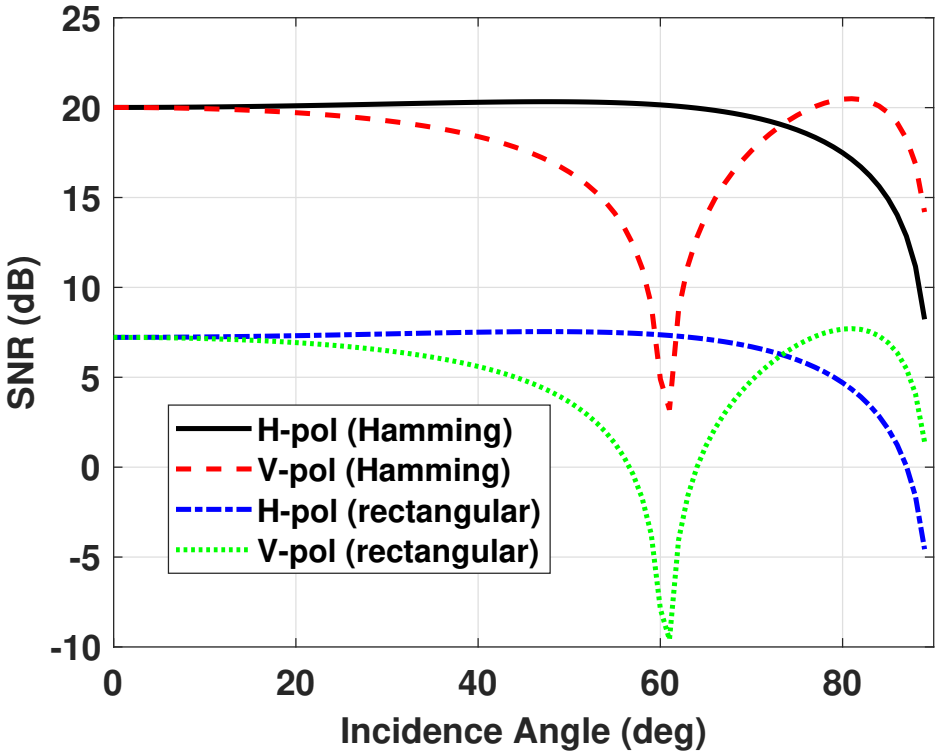

Figure 4.3: The SNR of the delay peak in ACF using both the Hamming and the rectangular window functions. The bandwidth is 3 GHz with $N = 461$, and $d_{ice} = 40$ cm.

at a distance $\Delta\tau$ from the zero delay peak is given by [54]

$$\mathrm{SLL}(\Delta\tau) = \mathrm{FSLL} + \mathrm{SLF} \times \log_2\left(\frac{\Delta\tau}{\tau_{\mathrm{FSLL}}}\right) \quad \text{(dB)} \tag{4.33}$$

where SLF (dB/Octave) is the side lobe fall-off of the window function, FSLL (dB) is the first side lobe level of the window function, and $\tau_{\mathrm{FSLL}} = \frac{1}{2}\left(\tau_{\text{main lobe}} + \tau_{\text{side lobe}}\right)$ is the location of the FSLL peak, where $\tau_{\text{main lobe}} = \frac{2\zeta_{\text{main lobe}}}{F_s}$ is the main lobe width between the first zero crossings, $\zeta_{\text{main lobe}}$ is a factor depending on the window function, F_s is the frequency bandwidth, and $\tau_{\text{side lobe}}$ is the width of the first side lobe. For instance, SLF = -3 dB/Octave, FSLL = -6.5 dB, and $\zeta_{\text{main lobe}} = 1$ for the rectangular window, while SLF = -3 dB/Octave, FSLL = -21.5 dB, and $\zeta_{\text{main lobe}} = 2$ for the Hamming window. The width of the first side lobe in both the Hamming and the rectangular window is the same and equal to $\frac{1}{F_s}$. It can be observed from (4.33), that the SLL value would be smaller for larger time delays (thicker loss-less pack); hence the SNR would be higher, and the RMSTDE would be lower. For example, the RMSTDE at different time delays at nadir using both the Hamming and the rectangular window functions are shown in Figures 4.4(a) and 4.4(a), respectively. It can be observed that the RMSTDE and CRLB meets at longer time delays (thicker packs). The SNR of the delay peak as a function of time delay using both the Hamming and rectangular window functions are also shown in Fig. 4.5. It should be noted that the time delay varied from 1 ns, which is just after the τ_{FSLL} of the both window functions.

So far, it was assumed that the we have a sufficient number frequency points, N, over the frequency span, F_s, such that the precision of the ACF in the time domain is high enough that the RMSTDE in (4.32) dictates the error in the measured time delay. If this was not the case, an independent source of error due to the number of time bins would be added to the radicand in (4.32). This correction is called

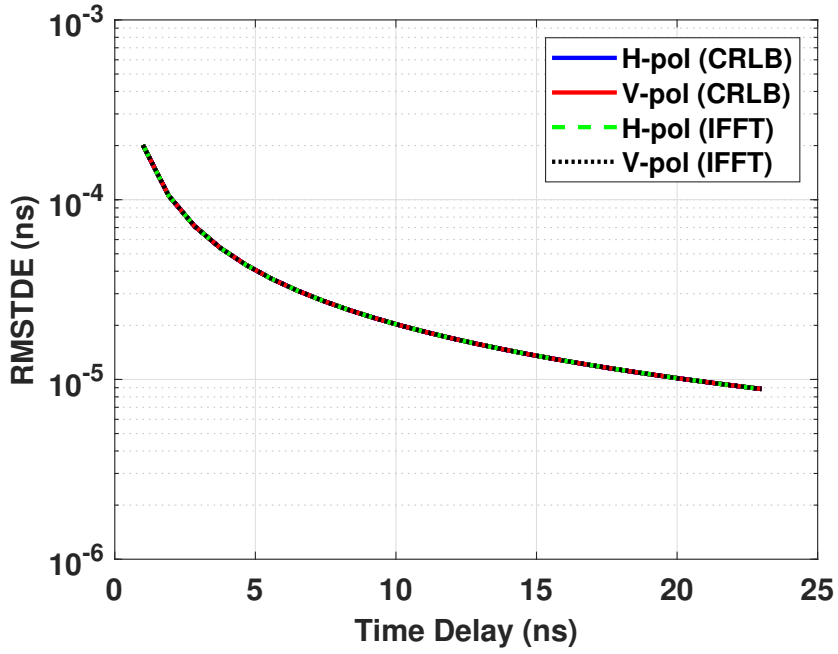

(a)

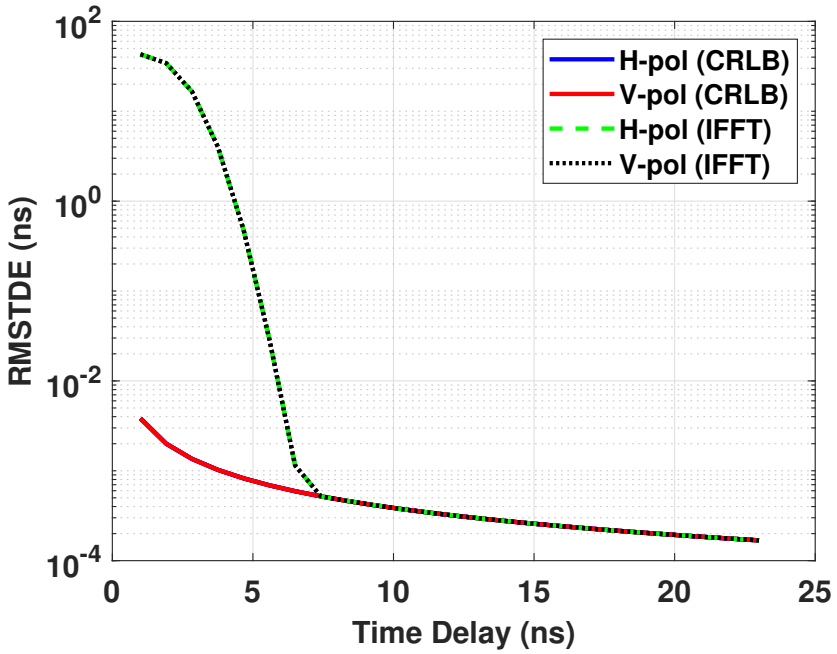

(b)

Figure 4.4: The root mean square time delay error (RMSTDE) of IDFT using both (a) the Hamming and (b) the rectangular window as a function of the microwave propagation time through the pack. The bandwidth is 3 GHz with $N = 461$, and $\theta = 0°$.

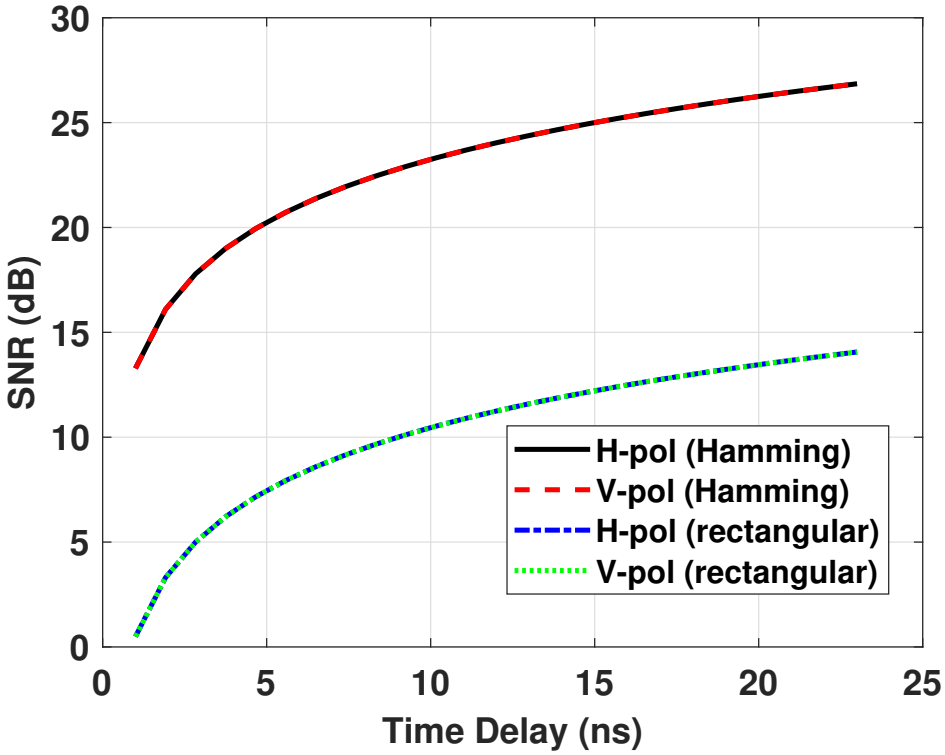

Figure 4.5: The SNR of the delay peak in ACF using both the Hamming and the rectangular window functions as a function of time delay. The bandwidth is 3 GHz with $N = 461$, and $\theta = 0°$.

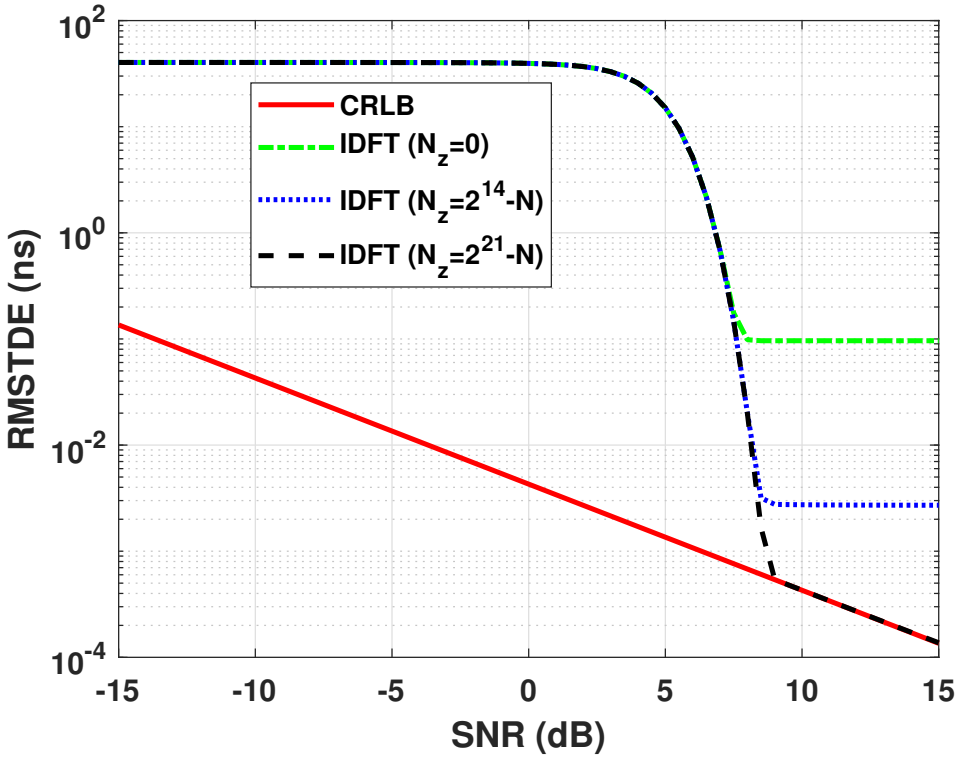

Figure 4.6: The measured root mean square time delay error (RMSTDE) of IDFT for a 40 cm icepack with respect to SNR of the delay peak with different number of zeros in the zero-padding prior to the inverse Fourier transform. The CRLB is also shown in the figure for comparison. The bandwidth is 3 GHz with $N = 461$, and the incidence angle is $\theta = 0°$ ($\tau_{delay} = 4.73$ ns).

Sheppard's correction [84], and it is $\frac{h^2}{12}$ for the second moment about the mean, where $h = N/F_s(N + N_z)$ is the class interval, and N_z is the number of zeros added to the spectrum prior to its inverse Fourier transform. This effect is shown in Fig. 4.6. The bandwidth is 3 GHz, $N = 461$, and $d_{ice} = 40$ cm ($\theta = 0°$, $\tau_{delay} = 4.73$ ns). It can be observed by adding sufficient number of zeros, N_z, the measured RMSTDE gets closer to the true RMSTDE in (4.32). It can be observed that with $N_z = 0$ and $N_z = 2^{14} - N$, the RMSTDE can only get to a minimum of about 0.1 ns and 0.003 ns, receptively, while it can reach reaches the CRLB with $N_z = 2^{21} - N$ for SNR$\geq$ 9 dB.

4.2.2 Multi Layer Media

So far, we have discussed the error in the measured timed for single layer media. For a two-layer medium, we start with the approximated emissivity formula, as given by [54]

$$e(f) \approx \overline{e}\Bigg(1 - 2\Big[A_i \cos(2\pi n \mathrm{T}_{ice}) + A_s \cos(2\pi n \mathrm{T}_{snow}) + A_\Sigma \cos\Big(2\pi n\big(\mathrm{T}_{snow} + \mathrm{T}_{ice}\big)\Big) + A_\Delta \cos\Big(2\pi n\big(\mathrm{T}_{snow} - \mathrm{T}_{ice}\big)\Big)\Big]\Bigg) + w[n] \tag{4.34}$$

where $\bar{e}$ is the mean emissivity over frequency, A_i, A_s, A_Σ, and A_Δ are one half of the amplitudes of the ripple due to icepack time delay, snowpack time delay, sum of the time delays, and difference of the time delays, respectively, in the emissivity as a function of frequency [54]. For simplicity, we use $\mathrm{T}_\Sigma = \mathrm{T}_{ice} + \mathrm{T}_{snow}$ and $\mathrm{T}_\Delta = |\mathrm{T}_{snow} - \mathrm{T}_{ice}|$. Let's first assume that we want to estimate T_{ice} and T_{snow}, and the standard deviation (SD) of T_Σ and T_Δ can be easily found. Hence, the Fisher information matrix and it inverse are given by (4.35) and (4.36), respectively.

$$I(\chi) = \frac{(4\pi\bar{e})^2 \sum_{n=0}^{N-1} n^2}{2\sigma_w^2} \begin{bmatrix} A_i^2 + A_\Sigma^2 + A_\Delta^2 & A_\Sigma^2 - A_\Delta^2 \\ A_\Sigma^2 - A_\Delta^2 & A_s^2 + A_\Sigma^2 + A_\Delta^2 \end{bmatrix} \tag{4.35}$$

$$I^{-1}(\chi) = \frac{2\sigma_w^2}{(4\pi\bar{e})^2 D \sum_{n=0}^{N-1} n^2} \begin{bmatrix} A_s^2 + A_\Sigma^2 + A_\Delta^2 & A_\Delta^2 - A_\Sigma^2 \\ A_\Delta^2 - A_\Sigma^2 & A_i^2 + A_\Sigma^2 + A_\Delta^2 \end{bmatrix} \tag{4.36}$$

where $D = A_s^2\left(A_i^2 + A_\Sigma^2 + A_\Delta^2\right) + A_i^2\left(A_\Sigma^2 + A_\Delta^2\right) + 4A_\Sigma^2 A_\Delta^2$ is the determinant of $I(\chi)$. Hence, we have the CRLB for T_{ice} and T_{snow}, as given by

$$Var(\mathrm{T}_{ice}) \geq \frac{3\sigma_w^2\left(A_s^2 + A_\Sigma^2 + A_\Delta^2\right)}{\left(2\pi\bar{e}\right)^2 DN(N-1)(2N-1)} \tag{4.37a}$$

$$Var(\mathrm{T}_{snow}) \geq \frac{3\sigma_w^2\left(A_i^2 + A_\Sigma^2 + A_\Delta^2\right)}{\left(2\pi\bar{e}\right)^2 DN(N-1)(2N-1)} \tag{4.37b}$$

Since the variables T_{ice} and T_{snow} are not independent (their co-variance is not zero), $Var(|\mathrm{T}_{snow} \pm \mathrm{T}_{ice}|) = Var(\mathrm{T}_{ice}) + Var(\mathrm{T}_{snow}) \pm 2Cov(\mathrm{T}_{ice}, \mathrm{T}_{snow})$. Hence, the CRLB for $\mathrm{T}_{snow} + \mathrm{T}_{ice}$ and $|\mathrm{T}_{snow} - \mathrm{T}_{ice}|$ are given by

$$Var(\mathrm{T}_{ice} + \mathrm{T}_{snow}) \geq \frac{3\sigma_w^2\left(A_s^2 + A_i^2 + 4A_\Delta^2\right)}{\left(2\pi\bar{e}\right)^2 DN(N-1)(2N-1)} \tag{4.38a}$$

$$Var(|\mathrm{T}_{snow} - \mathrm{T}_{ice}|) \geq \frac{3\sigma_w^2\left(A_s^2 + A_i^2 + 4A_\Sigma^2\right)}{\left(2\pi\bar{e}\right)^2 DN(N-1)(2N-1)} \tag{4.38b}$$

Similar to the single layer medium, we will use IDFT to find the delay peaks in ACF, as given by (4.20). We will also have similar hypothesis, as given by

$$H_0 : e[n] = \bar{e}_0 + w[n], \qquad n = 0, 1, \ldots, N-1 \tag{4.39a}$$

$$H_1 : e[n] = \overline{e}\Bigg(1 - 2\Big[A_i\cos(2\pi n\mathrm{T}_{ice}) + A_s\cos(2\pi n\mathrm{T}_{snow}) + A_\Sigma\cos\Big(2\pi n\big(\mathrm{T}_{snow} + \mathrm{T}_{ice}\big)\Big) + A_\Delta\cos\Big(2\pi n\big(\,|\mathrm{T}_{snow} - \mathrm{T}_{ice}|\,\big)\Big)\Big]\Bigg) + w[n] \tag{4.39b}$$

The first hypothesis H_0 assumes that $e[n]$ consists only of noise with a constant value of emissivity, $\bar{e}_0$, while in H_1 the sinusoidal signal is persumed to be present. The goal is to find the $P_{FA} = P(D_1|H_0)$ and the $P_D = P(D_1|H_1)$ for each delay peak, where D_1 is the decision of hypothesis H_1. Denote the auto-correlation function (ACF) coefficients at $\mathrm{T} = \frac{k}{N}$ for the noise only case and the signal present case by

$S_{e_0}(k)$ and $S_{e_1}(k)$, respectively. The value of $S_{e_1}(k_\ell)$ at the $\mathrm{T}_\ell = \frac{k_\ell}{N}$, where $\ell = i, s, \Sigma, \Delta$, is computed as

$$S_{e_1}(k_\ell) = \sqrt{a_\ell^2 + b_\ell^2} \tag{4.40}$$

where

$$a_\ell \triangleq \frac{1}{N}\sum_{n=0}^{N-1}\Bigg\{\overline{e}\Bigg(1 - 2\Bigg[A_i\cos(2\pi n\mathrm{T}_{ice}) + A_s\cos(2\pi n\mathrm{T}_{snow}) + A_\Sigma\cos\Big(2\pi n\big(\mathrm{T}_{snow} + \mathrm{T}_{ice}\big)\Big) + A_\Delta\cos\Big(2\pi n\big(\,|\mathrm{T}_{snow} - \mathrm{T}_{ice}|\,\big)\Big)\Bigg]\Bigg)\Bigg\}\cos\left(\frac{2\pi n k_\ell}{N}\right) \tag{4.41a}$$

$$b_\ell \triangleq \frac{1}{N}\sum_{n=0}^{N-1}\Bigg\{\overline{e}\Bigg(1 - 2\Bigg[A_i\cos(2\pi n\mathrm{T}_{ice}) + A_s\cos(2\pi n\mathrm{T}_{snow}) + A_\Sigma\cos\Big(2\pi n\big(\mathrm{T}_{snow} + \mathrm{T}_{ice}\big)\Big) + A_\Delta\cos\Big(2\pi n\big(\,|\mathrm{T}_{snow} - \mathrm{T}_{ice}|\,\big)\Big)\Bigg]\Bigg)\Bigg\}\sin\left(\frac{2\pi n k_\ell}{N}\right) \tag{4.41b}$$

where a_ℓ and b_ℓ are Gaussian random variables. They are independent and of identical variances of $\sigma^2 = \frac{\sigma_w^2}{2}$, where σ_w^2 is the power of the noise $w[n]$.

Similarly, the PDF of $S_{e_1}(k_\ell)$ is a Ricean distribution, as given by

$$\rho_{s_\ell}(u) = \frac{u}{\sigma^2}\exp\left(-\frac{s_\ell^2 + u^2}{2\sigma^2}\right) I_0\left(\frac{us_\ell}{\sigma^2}\right) \tag{4.42}$$

where the quantity s_ℓ equals the square root of the sum of the mean square of a_ℓ and b_ℓ, that is, $s_\ell = \sqrt{2}A_\ell\bar{e}$. Similarly, the remaining $S_{e_1}(k)$, except for those that correspond to one of the other three paths, and all the $S_{e_0}(k)$ are of Rayleigh distribution, as given by

$$\rho_w(u) = \frac{u}{\sigma^2}\exp\left(-\frac{u^2}{2\sigma^2}\right) \tag{4.43}$$

Similarly, assuming that the IDFT coefficients are independent, P_{FA} is the same as (4.26), as given by

$$P_{FA} = 1 - \left(1 - \exp\left(-\frac{V_{T_\ell}^2}{2\sigma^2}\right)\right)^{(\frac{N}{2})-1} \tag{4.44}$$

where V_{T_ℓ} is a threshold value of the ACF coefficient at each delay peak. The probability of detection for each peak is also similar to (4.27), as given by

$$P_{D_\ell} = 1 - \left(1 - \exp\left(-\frac{V_{T_\ell}^2}{2\sigma^2}\right)\right)^{(\frac{N}{2})-5} \left(1 - Q_1\left(\frac{s_\ell}{\sigma}, \frac{V_{T_\ell}}{\sigma}\right)\right) \tag{4.45}$$

Similar to the single layer medium case, the RMSTDE$_\ell$ for each delay peak,T$_\ell$ = $\frac{k_\ell}{N}$, can be found by first calculating the probability of occurrence of an anomaly in the IDFT, as given by

$$\begin{aligned} q_\ell &= P\Big(S_{e_1}(k_\ell) \leq \text{at least one of the } S_{e_1}(1)S_{e_1}(2), \ldots, S_{e_1}(k_\ell - 1), S_{e_1}(k_\ell + 1), \\ &\qquad \ldots, S_{e_1}(N/2 - 1)\Big) \\ &= \int_0^\infty P\left(S_{e_1}(k_\ell) = u\right) \cdot \left[1 - \prod_{k=1, k\neq k_i, k_s, k_\Sigma, k_\Delta}^{(\frac{N}{2})-1} P\left(S_{e_1}(k) < u\right)\right] du \\ &= \int_0^\infty \rho_{s_\ell}(u) \left[1 - \prod_{k=1, k\neq k_i, k_s, k_\Sigma, k_\Delta}^{(\frac{N}{2})-1} \int_0^u \rho_w(\nu) d\nu\right] du \end{aligned} \tag{4.46}$$

which must be again computed numerically. It is noted in (4.46) that all the other values of ℓ are excluded. Assuming that the anomaly estimate is uniformly distributed between 0 and 0.5, the overall RMSTDE$_\ell$ using the IDFT estimator is given by

$$\text{RMSTDE}_\ell = \sqrt{\left(1 - q_\ell\right) Var_{\text{T}_\ell}(N) + q_\ell \int_0^{0.5} 2\left(u - \text{T}_\ell\right)^2 du} \tag{4.47}$$

RMSTDE$_\ell$ for each delay peak in a two layer medium of an icepack with a dry snow cover at nadir incidence angle and the CRLB as a function of SNR$_\ell = (\sqrt{2}A_\ell \bar{e})/\sigma_w$ are shown in Fig. 4.7. The bandwidth is 3 GHz, $N = 461$, $d_{ice} = 40$ cm, and $d_{snow} = 15$ cm. The measured time delay at nadir for an icepack ($n_{ice} = \sqrt{3.15}$) and a dry snowpack ($\rho_s = 210$ kg/m^3, $n_{snow} = 1.18$) are $\tau_{ice} = 4.73$ ns and $\tau_{snow} = 1.18$ ns, respectively. It can be observed that for SNR$_{ice} \geq 7.5$ dB, SNR$_{snow} \geq 7.5$ dB, SNR$_\Sigma \geq 7.5$ dB, and SNR$_\Delta \geq 3.5$ dB, the IDFT's RMSTDE meets the CRLB for each delay peak. The effect of the number of zeros, N_z, for zero padding on the RMSTDE$_\ell$ for each delay peak would be similar to the single layer scenario as shown in Fig. 4.6.

The RMSTDE in IDFT for τ_{ice}, τ_{snow}, τ_Σ, and τ_Δ delay peaks using both the Hamming and rectangular windows are shown in Figures 4.8, 4.9, 4.10, and 4.11, respectively. The RMSTDE at τ_{ice} and τ_Σ meets the CRLB using Hamming window in H-pol, while at τ_{snow} and τ_Δ, it only meets the CRLB at grazing incidence angles ($\theta \geqslant 70°$) using Hamming window in H-pol. In V-pol the RMSTDE gets larger, mostly around the Brewster angles. On the other hand, the RMSTDE does not the CRLB using the rectangular window. The SNR of the τ_{ice}, τ_{snow}, τ_Σ, and τ_Δ delay peaks using the Hamming and rectangular windows are also shown Figures 4.12, 4.13, 4.14, and 4.15, respectively.

4.3 Field Measurements

Due to the freedom of access to single traces in the new X-band WiBAR instrument, we were only able to extract the measured RMSTDE from the Winter 2018 measurement campaign as reported in [56]. The incidence angles ranged from 9.2° to 70.2°. The frequency range was 7-10 GHz. At these frequencies, the ice and snow may typically have negligible volume and surface scattering. The ice observations by WiBAR were made from about 10:00 AM untill around 1:00 PM on March 03,

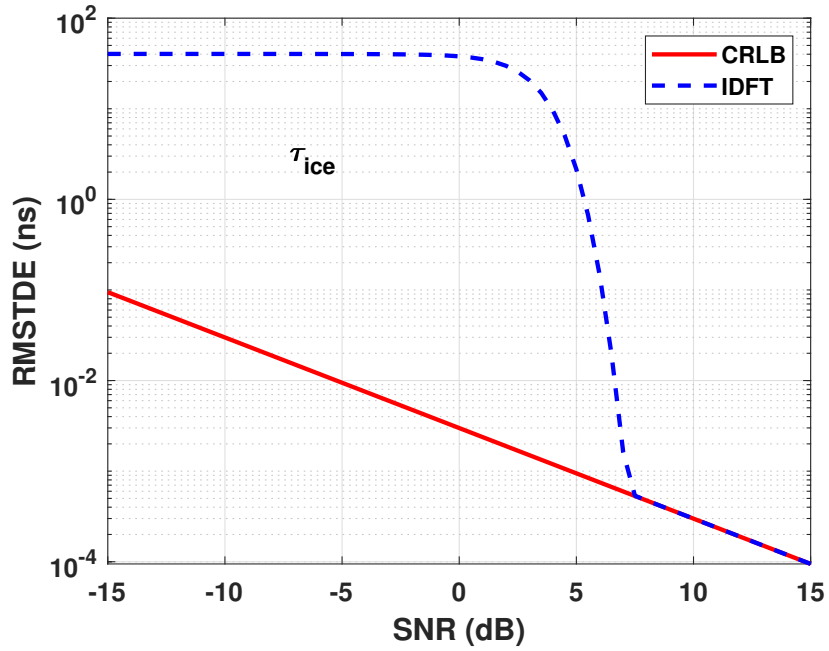
CRLB
IDFT
τ_{ice}
RMSTDE (ns)
SNR (dB)
10^{2}
10^{0}
10^{-2}
10^{-4}
-15
-10
-5
0
5
10
15

(a)

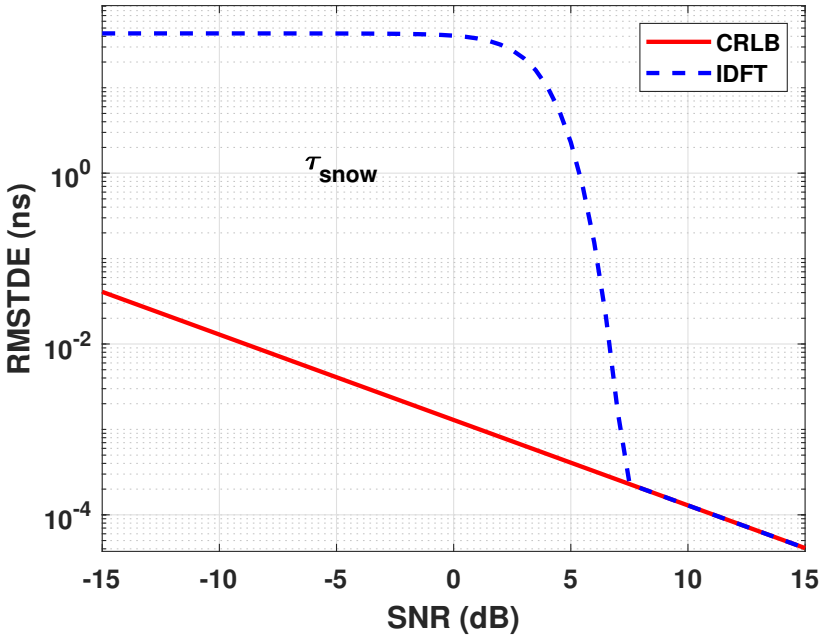
CRLB
IDFT
τ_{snow}
RMSTDE (ns)
SNR (dB)
10^{0}
10^{-2}
10^{-4}
-15
-10
-5
0
5
10
15

(b)

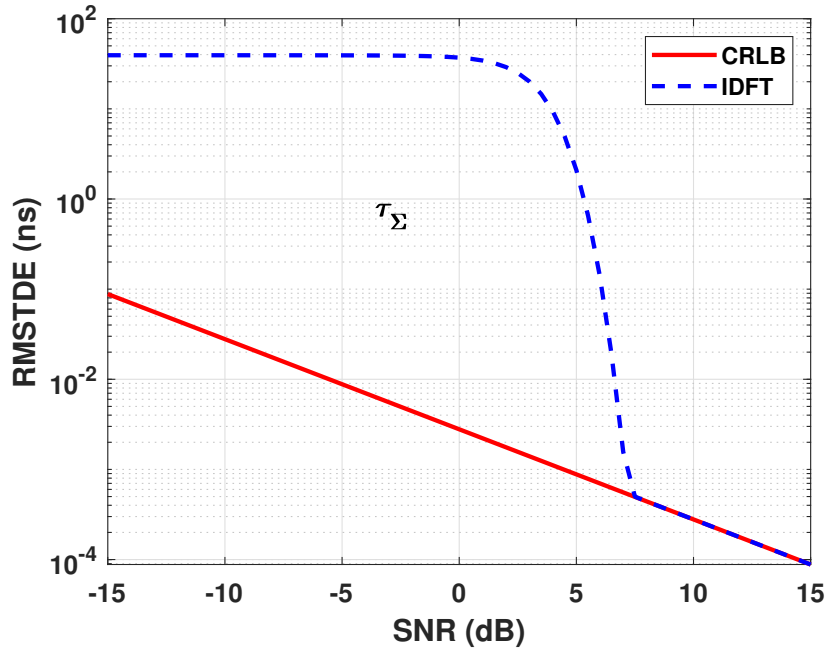

(c)

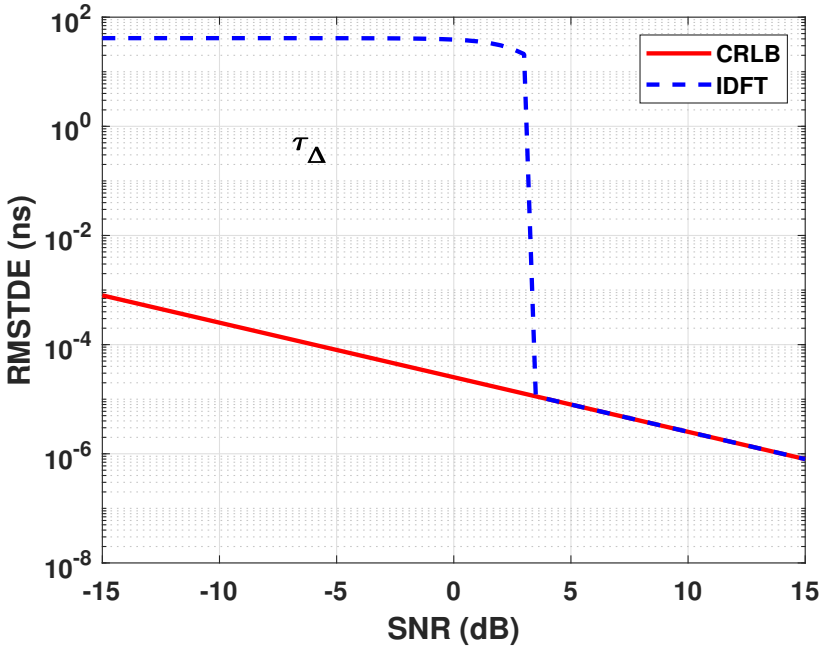

(d)

Figure 4.7: Theoretical RMSTDE of IDFT for (a) τ_{ice}, (b) τ_{snow}, (c) τ_Σ, and (d) τ_Δ in the case of a lake icepack with dry snow cover with respect to SNR of the delay peaks. The CRLB is also shown in the figures for comparison. The bandwidth is 3 GHz with $N = 461$, $d_{ice} = 40$ cm, $d_{snow} = 15$ cm ($\rho_s = 210$ kg/m^3, $n_{snow} = 1.18$) and the incidence angle is $\theta = 0°$ ($\tau_{ice} = 4.73$ ns, $\tau_{snow} = 1.18$ ns).

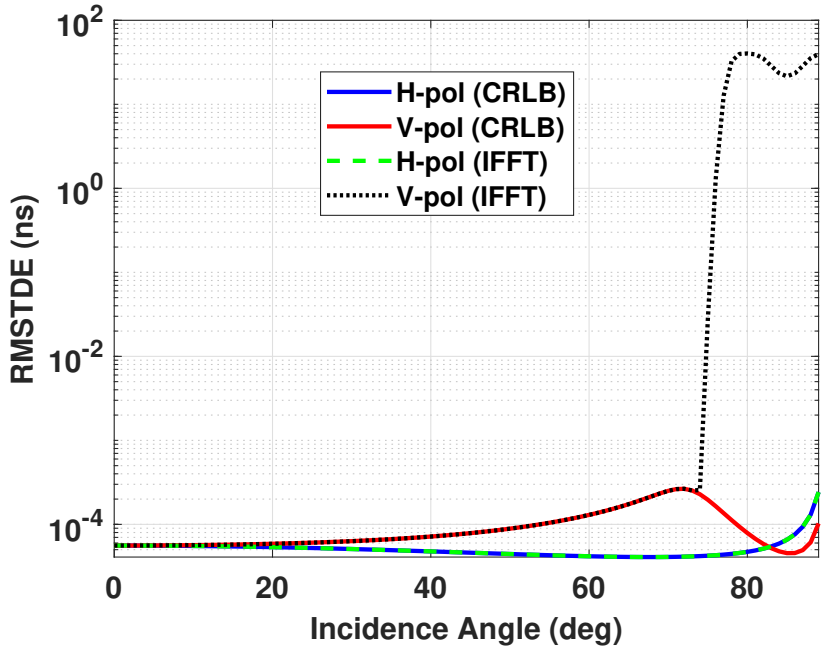

(a)

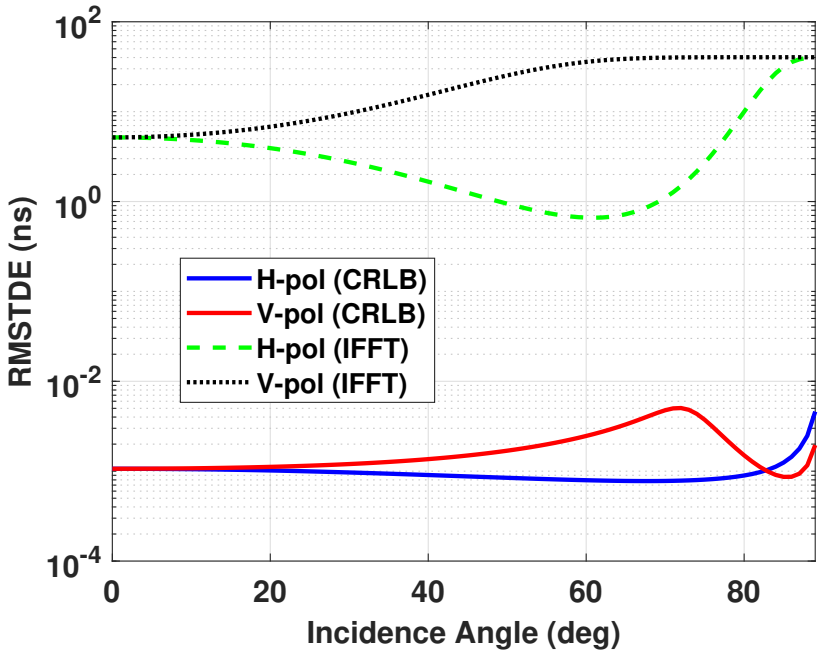

(b)

Figure 4.8: The mean square time delay error (MSTDE) of IDFT at τ_{ice} delay peak using both (a) the Hamming and (b) the rectangular window as a function of incidence. The bandwidth is 3 GHz with $N = 461$, $d_{ice} = 40$ cm, and $d_{snow} = 15$ cm ($\rho_s = 210$ kg/m^3, $n_{snow} = 1.18$).

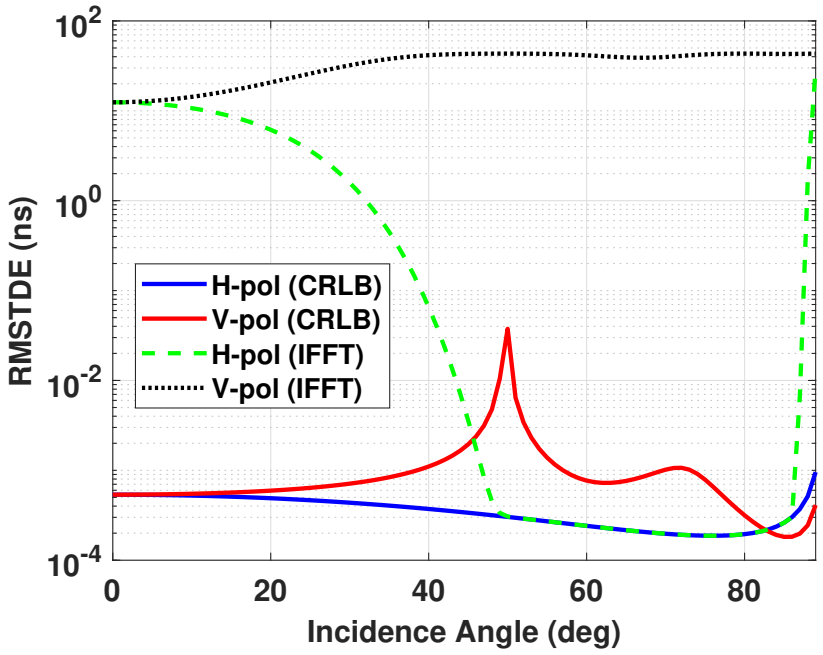

(a)

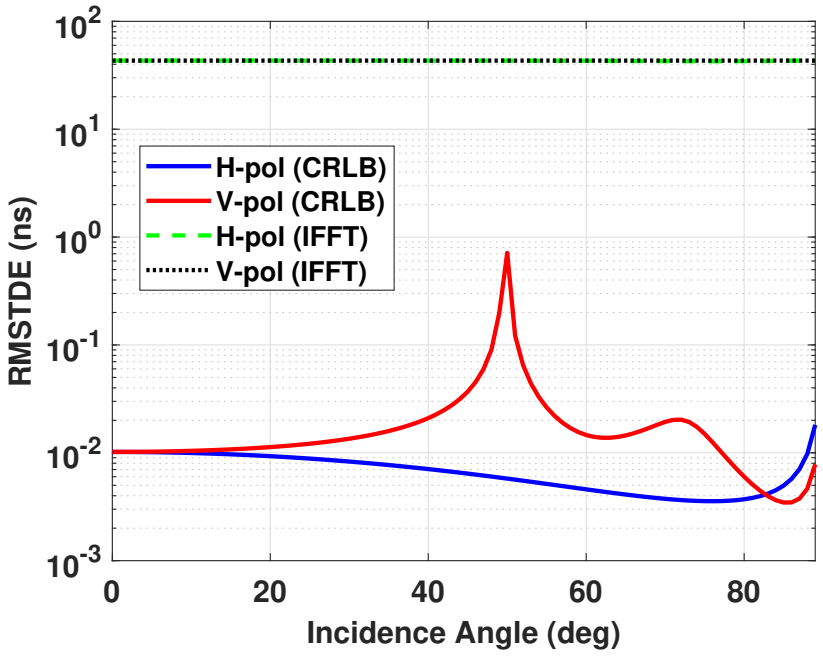

(b)

Figure 4.9: The root mean square time delay error (RMSTDE) of IDFT at τ_{snow} delay peak using both (a) the Hamming and (b) the rectangular window as a function of incidence. The bandwidth is 3 GHz with $N = 461$, $d_{ice} = 40$ cm, and $d_{snow} = 15$ cm ($\rho_s = 210$ kg/m^3, $n_{snow} = 1.18$).

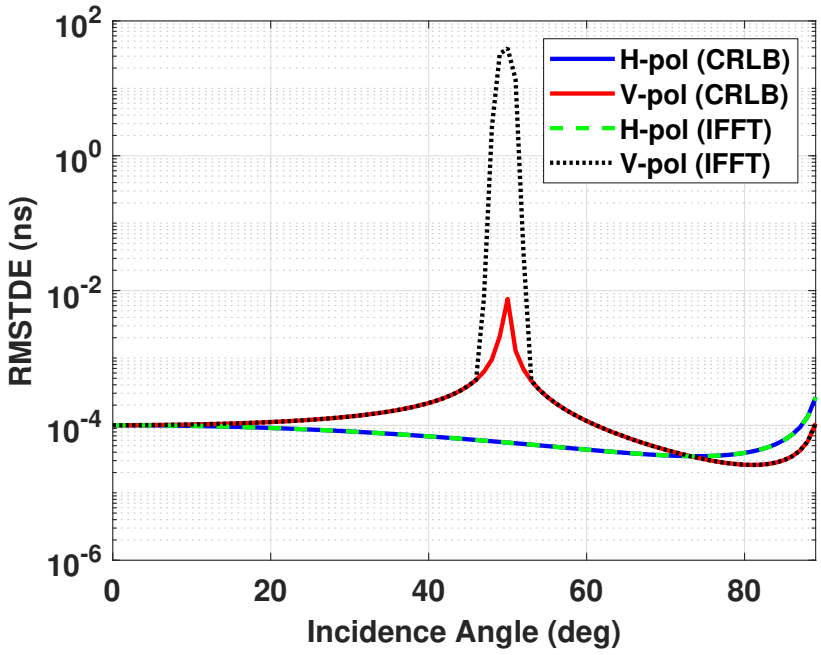

(a)

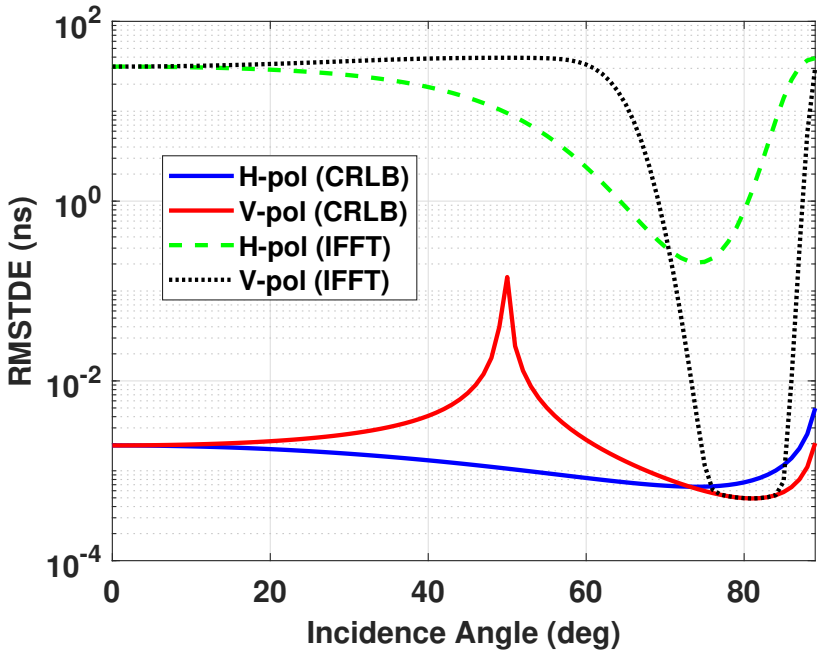

(b)

Figure 4.10: The root mean square time delay error (RMSTDE) of IDFT at τ_Σ delay peak using both (a) the Hamming and (b) the rectangular window as a function of incidence. The bandwidth is 3 GHz with $N = 461$, $d_{ice} = 40$ cm, and $d_{snow} = 15$ cm ($\rho_s = 210$ kg/m^3, $n_{snow} = 1.18$)

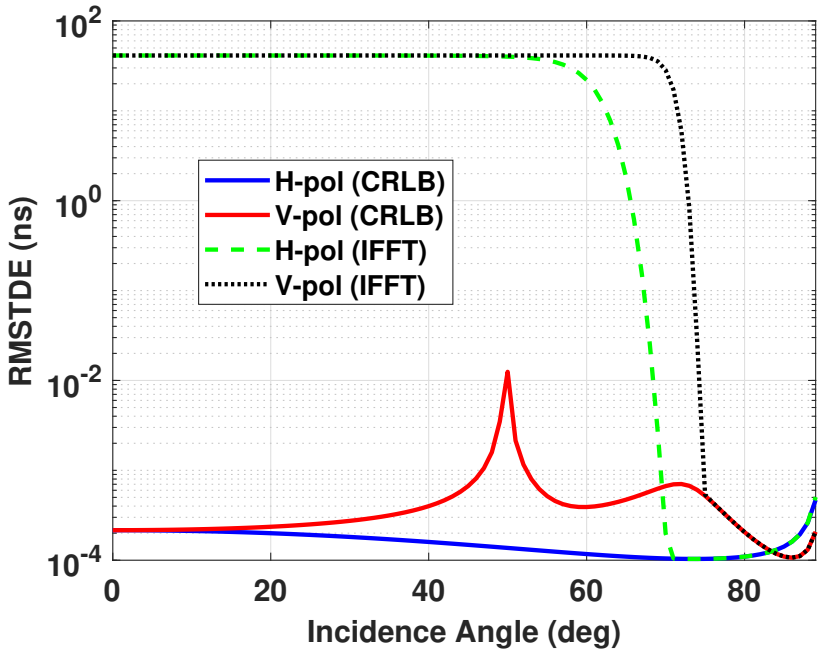

(a)

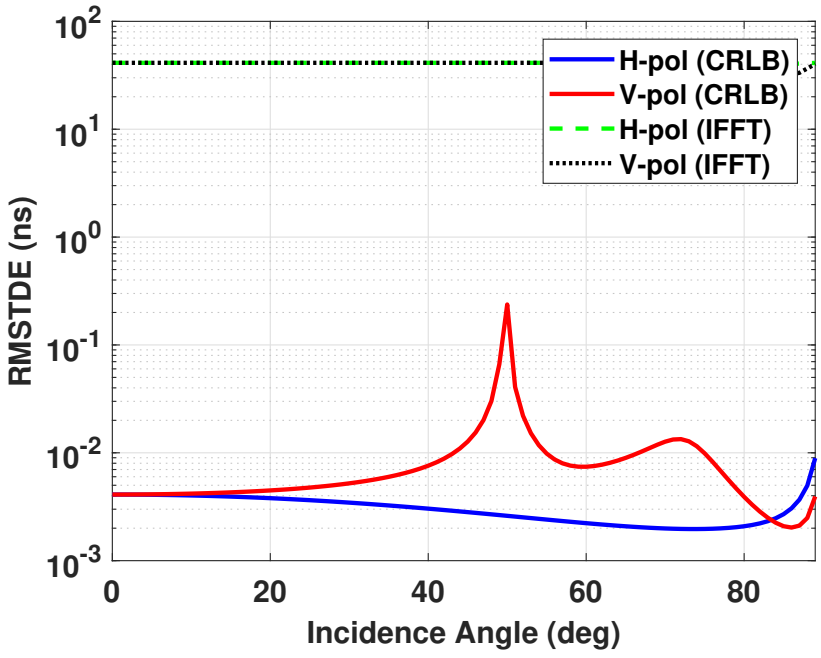

(b)

Figure 4.11: The root mean square time delay error (RMSTDE) of IDFT at τ_Δ delay peak using both (a) the Hamming and (b) the rectangular window as a function of incidence. The bandwidth is 3 GHz with $N = 461$, $d_{ice} = 40$ cm, and $d_{snow} = 15$ cm ($\rho_s = 210$ kg/m^3, $n_{snow} = 1.18$).

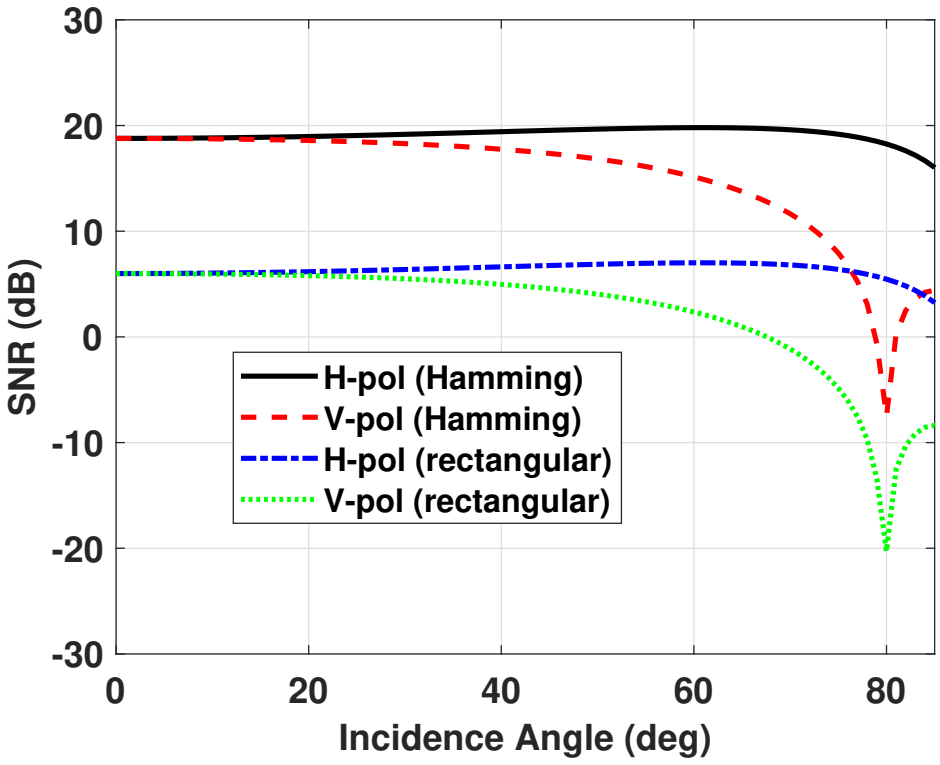

Figure 4.12: The SNR of the τ_{ice} delay peak in ACF using both the Hamming and the rectangular window functions. The bandwidth is 3 GHz with $N = 461$, $d_{ice} = 40$ cm, and $d_{snow} = 15$ cm ($\rho_s = 210$ kg/m^3, $n_{snow} = 1.18$).

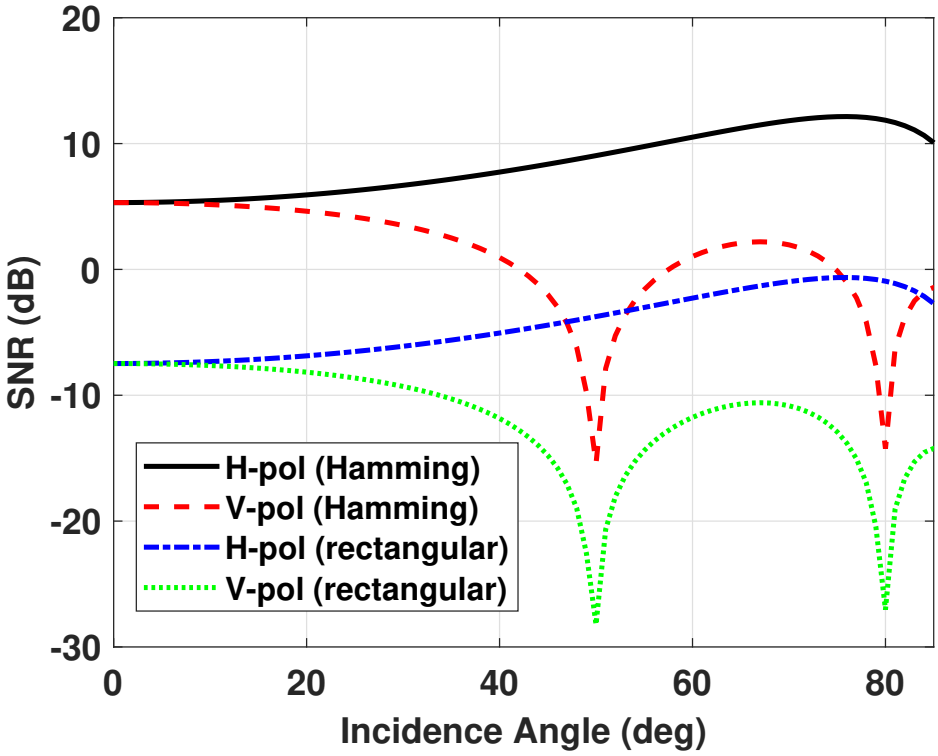

Figure 4.13: The SNR of the τ_{snow} delay peak in ACF using both the Hamming and the rectangular window functions. The bandwidth is 3 GHz with $N = 461$, $d_{ice} = 40$ cm, and $d_{snow} = 15$ cm ($\rho_s = 210$ kg/m^3, $n_{snow} = 1.18$).

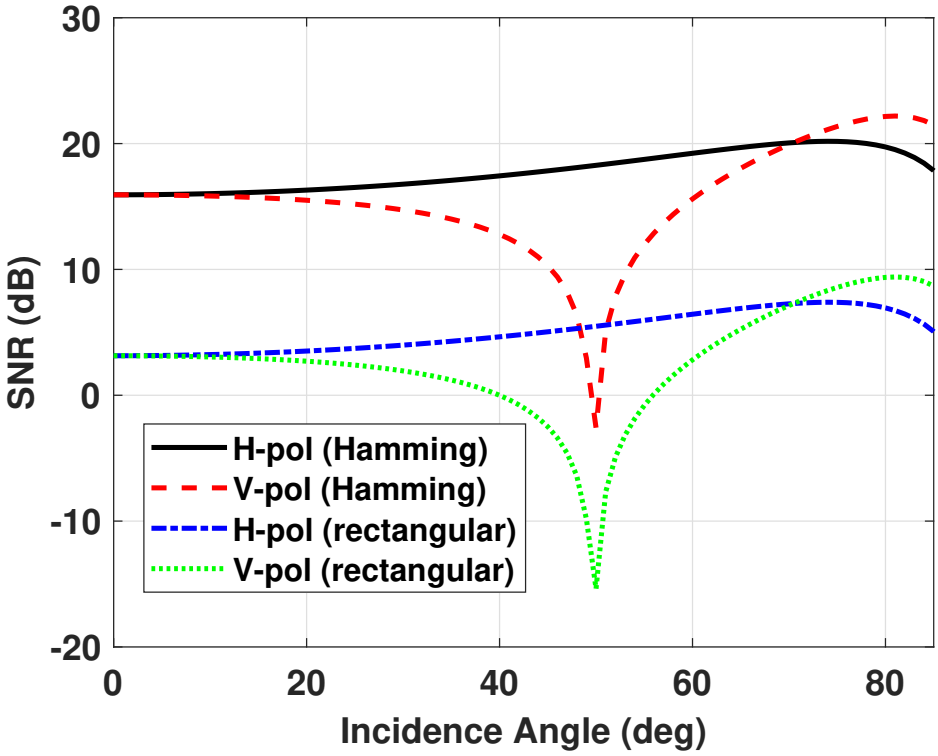

Figure 4.14: The SNR of the τ_Σ delay peak in ACF using both the Hamming and the rectangular window functions. The bandwidth is 3 GHz with $N = 461$, $d_{ice} = 40$ cm, and $d_{snow} = 15$ cm ($\rho_s = 210$ kg/m^3, $n_{snow} = 1.18$).

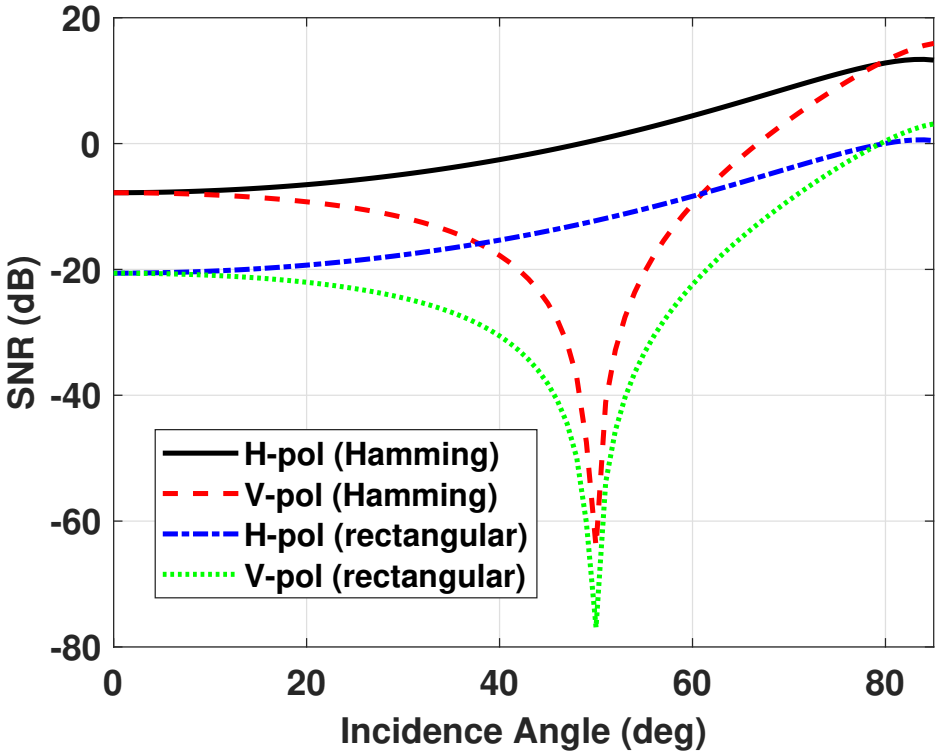

Figure 4.15: The SNR of the τ_Δ delay peak in ACF using both the Hamming and the rectangular window functions. The bandwidth is 3 GHz with $N = 461$, $d_{ice} = 40$ cm, and $d_{snow} = 15$ cm ($\rho_s = 210$ kg/m^3, $n_{snow} = 1.18$).

2018 on Lake Douglas at the University of Michigan Biological Station (UMBS). The air temperature was about -7.0 °C and -0.8 °C at around 10:00 AM and noon. The ground truth measurements of ice thickness were done with a tape measure at the conclusion of the WiBAR measurements. The ground truth value of ice thickness was about 39-40 cm.

As an illustrative example, the RMSTDE and the SNR of the the successful measured delay peak in the ACF as a function of the number of traces (N_{trace}) used in the delay peak's retrieval process are shown in Figs. 4.16(a) and 4.16(b), respectively. The total number of acquired traces are 50. The number of frequency points used in these figures are $N = 14999$ and $N = 3000$, and the number of zeros added for zero padding prior to the inverse Fourier transform are $N_z = 2^{21} - N$. The incident angle is $\theta = 9.2°$, and the Hamming window was used. It can be observed that the RMSTDE is inversely proportional to both number of frequency points and number of traces used in the post processing. The SNR is also directly proportional to the number of frequency points and is independent of N_{trace}, as N_{trace} does not change the power of the ACF noise floor. The SNR is about 9.4 dB and 8.2 dB for $N = 14999$ and $N = 3000$, respectively.

The RMSTDE and the SNR of the measured delay peak at nadir ($\theta = 9.2°$) as a function of number of added zeros, N_z, are shown in Figs. 4.17(a) and 4.17(b), respectively. The number of traces used for each data point is $N_{trace} = 5$. The Hamming window was used. It can be observed that the RMSTDE is inversely proportional to the number of zeros, while the SNR is independent of N_z. The SNR is about 9.4 dB and 8.2 dB for $N = 14999$ and $N = 3000$, respectively.

To compare the measured and theoretical curves for RMSTDE, they are both illustrated on a same plot as shown in Fig. 4.18. It can be observed that the measured RMSTDE values are about 0.011 ns and 0.003 ns with $N = 3000$ and $N = 14999$ frequency points, respectively, and they are close to their corresponding theoretical

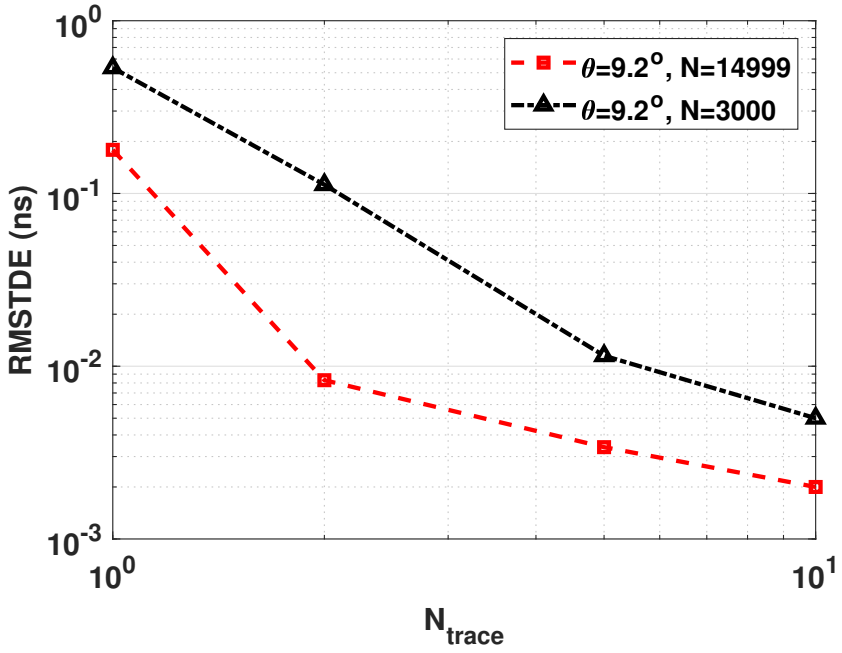

(a)

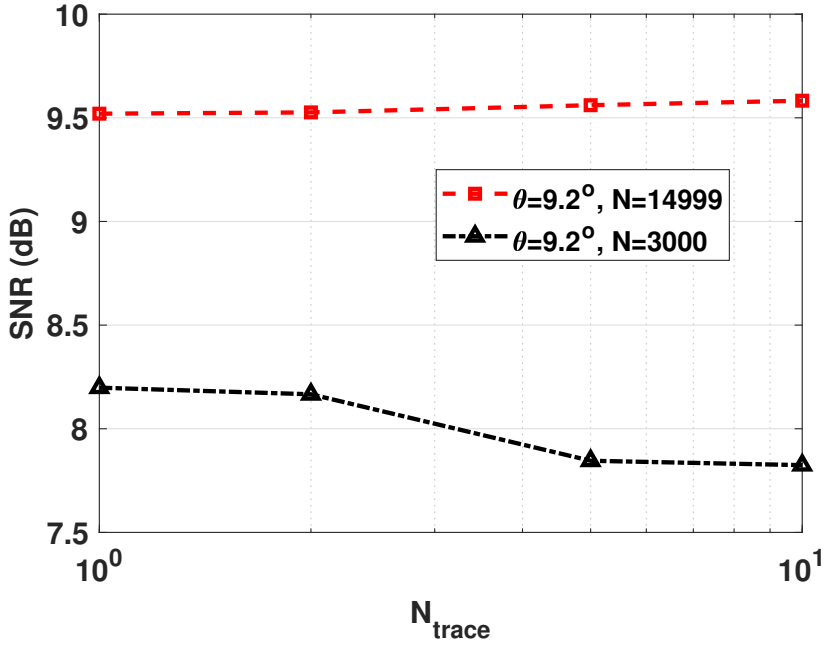

(b)

Figure 4.16: (a) The root mean square time delay error (RMSTDE) and (b) the SNR of the measured delay peak as a function of the number of traces N_{trace}. The number of added zeros for zero padding prior to the inverse Fourier transform is $N_z = 2^{21} - N$. The bandwidth was 3 GHz, and the Hamming window was used. The measurements were performed on Douglas Lake on March 03, 2018 ($\theta = 9.2°$, $d_{ice} = 39 - 40$ cm).

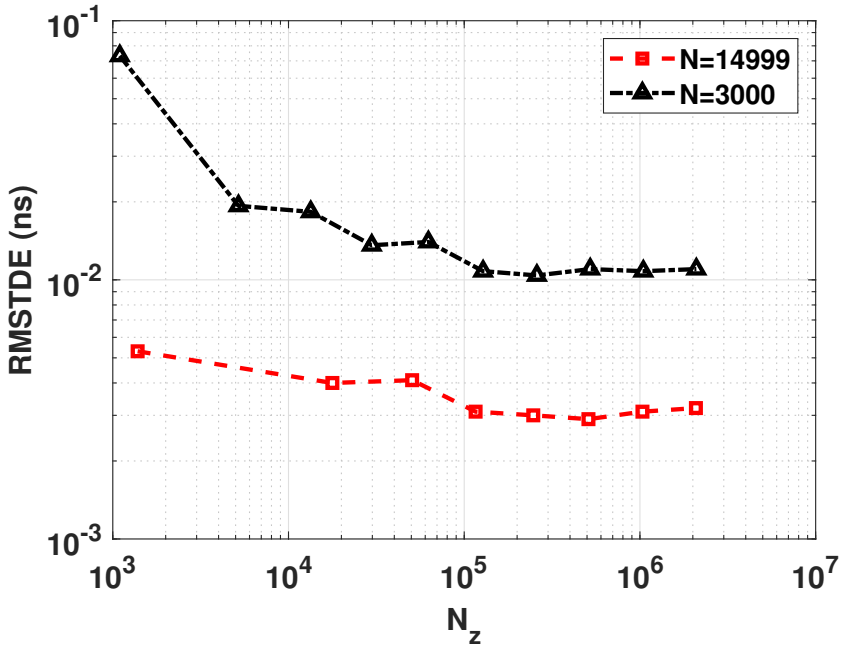

(a)

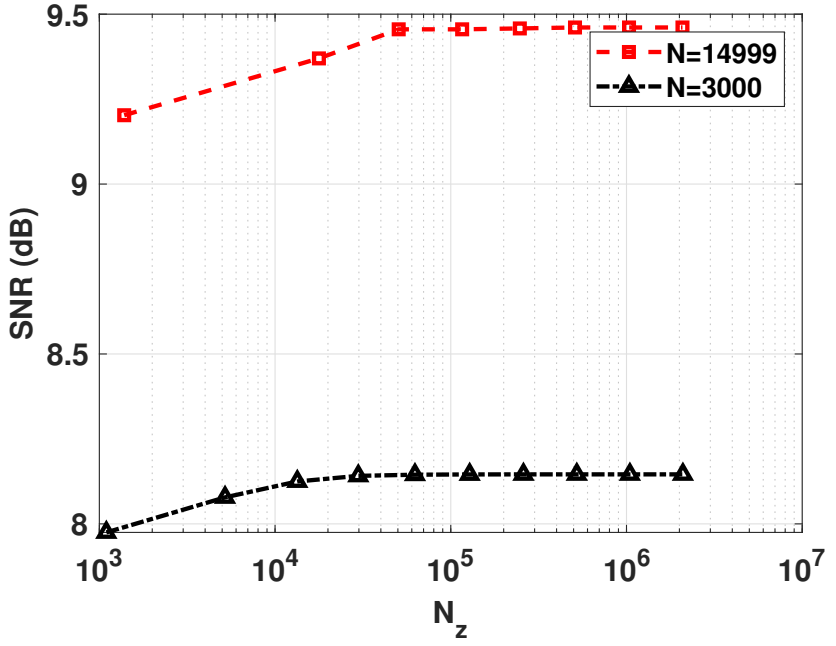

(b)

Figure 4.17: (a) The root mean square time delay error (RMSTDE) and (b) the SNR of the measured delay peak as a function of the number of added zeros (N_z). The number of traces used for each data point is $N_{trace} = 5$. The bandwidth was 3 GHz, and the Hamming window was used. The measurements were performed on Douglas Lake on March 03, 2018 ($\theta = 9.2°$, $d_{ice} = 39 - 40$ cm).

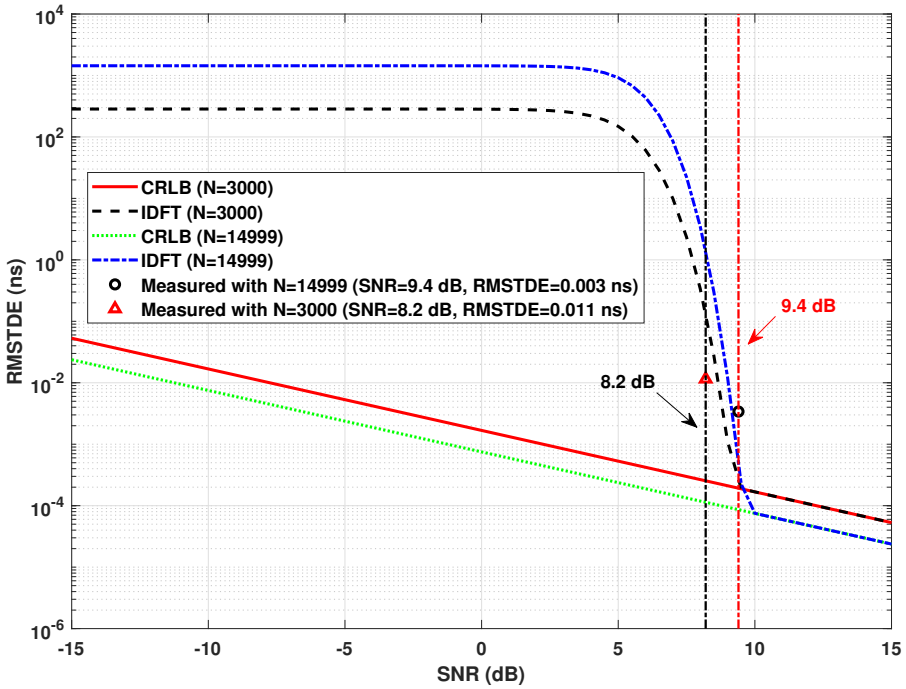

Figure 4.18: The theoretical and the measured RMSTDE of the delay peak of a 40 cm icepack as a function of the SNR of the delay peak. The number of traces used for each measurement is $N_{trace} = 5$. The bandwidth was 3 GHz, and the Hamming window was used ($\theta = 9.2°$).

curves. The measured SNR values are also 8.2 dB and 9.4 dB with $N = 3000$ and $N = 14999$ frequency points, respectively. Based on the 2017-2027 decadal survey for Earth Science and Applications from Space (ESAS) [62], the required snow depth accuracy is 2-20 cm, which is equal to the time delay accuracy of 0.15-1.57 ns for a snow with $\rho_s = 210\text{kg/m}^3$; thus, a WiBAR instrument would be able to satisfy this requirement with the right selection of parameters.

The errors in the measured dielectric constant and thickness of the pack using the two distinct incident angles are related to the error in the measured time delay by WiBAR, as discussed in Section 3.3. Since these measurements were done during the Winter 2016 campaign, we do not have access to single traces of the WiBAR measurements. However, as it can be observed from Fig. 3.37 in Section 3.5.2, the average of the SNRs of these two delay peaks is about 8 dB, and using Fig. 4.1 for a

single layer of ice with $N = 461$, the RSMTDE would be around $\delta\tau = 0.01$ ns. Hence, using this estimate value of the RMSTDE and (3.50), the errors in the measured dielectric constant and thickness of the pack using this approach are $\delta\epsilon_p \approx 0.1$ and $\delta d_p \approx 1.7$ cm, respectively, which are close to the reported values of $\delta\epsilon_p \approx 0.09$ and $\delta d_p \approx 1$ cm in Section 3.5.2.

CHAPTER V

Conclusions and Future Directions

5.1 A Brief Overview

Wideband autocorrelation radiometry is a passive remote sensing method of measuring the round trip propagation time, τ_{delay}, of microwaves through a low-loss dielectric slab, such as a freshwater lake icepack or terrestrial snowpack. This work describes a method of achieving the measurement by measuring the emissivity of the slab as a function of frequency. The coherent interference of rays traversing the slab different numbers of times gives rise to an emissivity spectra that oscillates around a mean value, with local maxima at wavelengths of constructive interference, and minima at wavelengths of destructive interference. This spectrum is inverse Fourier transformed to obtain an autocorrelation function, in which the mean propagation time manifests itself as a local maximum at a time lag greater than zero.

The minimum instrument requirements to retrieve τ_{delay} are derived, given an ideal slab, ie. smooth interfaces with no absorption or volume scattering. The bandwidth required is inversely related to the desired minimum measurable propagation time, but above this minimum, the temporal precision of the measurement can be made arbitrarily fine. While the superiority of H-polarized observations over V-pol can be easily seen from the fact that the reflection coefficients that cause the coherent interference are stronger at H-pol, the impact of polarization is quantified by the

number of samples needed to observe the propagation time for a given probability of detection and false alarm rate. The expected value of τ_{delay} depends on the incidence angle, θ. As such, an observation of a uniform target is adversely affected by an antenna's finite beamwidth, in proportion to the beamwidth and the slab thickness. This effect is a function of the incidence angle, with a maximum at 45° and minima at both nadir and grazing.

To demonstrate the technique, measurements of lake ice 36 cm thick were made with a simple instrument made from a standard gain horn, a portable spectrum analyzer, and a few RF components in between. The measurements were performed at incidence angles from nadir to 59°, and these measurements conformed to the elevation angular dependence expected from theory. The retrieved propagation times correspond to values of ice thickness within 2 cm of the ground truth. Thus, Wideband Autocorrelation Radiometry is a passive remote sensing method measuring freshwater lake ice thickness directly.

5.2 Contributions

Our contributions in this thesis are listed below:

- We demonstrated the potential of wideband autocorrelation radiometry (WiBAR) as a passive remote sensing method of measuring the thickness of a low-loss dielectric slab, such as freshwater lake icepack or terrestrial dry snowpack.
- We fully discussed the forward modeling of snow and ice layer.
- We derived the minimum instrument requirements to measure the pack thickness, given an ideal slab, i.e., smooth interfaces with no absorption or volume scattering.
- We fully discussed the effect of the presence of a snow layer on the lake ice

thickness measurement using WiBAR.

- We investigated the effect of the presence of variable layer thickness in a footprint of the radiometer's antenna.

- We demonstrated the ability of WiBAR in non-destructively measuring the dielectric constant and thickness of a low-loss dielectric layer. It is shown that the dielectric constant and the thickness of the pack can be directly measured using the measured time delays by WiBAR at two distinct incident angles.

- We modeled and designed three different versions of WiBAR instrument to measure the lake icepack and snowpack thickness. The WiBAR instrument is fabricated from commercial-off-the-shelf (COTS) components.

- We conducted field measurements for lake icepack on Douglas Lake at the University of Michigan Biological Station (UMBS), Argo Pond and Barton Dam in Ann Arbor, MI, and South Sturgeon Lake in Minnesota.

- We demonstrated elevation angular dependence of the measured thickness by the WiBAR as it was expected from theory.

5.3 Future Directions

We have fully discussed the physics of operation and system requirements of WiBAR. However, for any scientific work, there would be several directions that can be continued to further develop the concept. As such, below are some immediate and primary paths to further continue this work.

5.3.1 Time Domain Wideband Autocorrelation Radiometer (TD-WiBAR)

The instruments so far have all been operating in frequency domain using a field-portable spectrum analyzer as the radiometer receiver back-end. While this method

can be rapidly implemented, it suffers from high data acquisition time if this method is to move beyond plot-scale measurement to airborne or spaceborne platforms. In fact, the instantaneous bandwidth being observed by this instrument is determined by the 3 MHz resolution bandwidth (RBW) of the spectrum analyzer. As such, the time required to observe a 3 GHz frequency span is at least 1000 times that strictly needed: each lake icepack observation takes about 5 minutes, or one would need to implement a reciever with N receivers, each looking at a distinct resolution bandwidth.

An alternative back-end architecture is a digital oscilloscope. In this architecture, the autocorrelation function (ACF), $\Phi(\tau)$, is acquired directly in time-domain, by collecting a time-series of predetected voltages, $V(t)$, and correlating them at different time lags, τ, as given by

$$\Phi(\tau) = \frac{1}{N} \sum_{t=1}^{N} V(t)V(t+\tau) \tag{5.1}$$

where N is the total number of measurements. As the time lag is varied, the real part of the complex ACF is built up. The imaginary part is reconstructed by applying a Hilbert transform to the real part (mirrored about the zero lag), and the ACF is complete. This approach drastically speeds up the observation of τ_{delay}. Part of the speed-up is due to the fact that the entire frequency band is being observed at once. Another part is that the data does not need to be collected to calculate the ACF for all possible time delays, only those where a time delay would be expected.

5.3.2 Detail Analysis of a Lossy Layer of Snow or Ice

Microwave signals are very sensitive to the presence of any liquid water, which is always present during the snow melt period. As a result, microwave remote sensing instruments become blind during this period. One suggested approach is to use the radiative transfer method, which is based on the law of conservation of energy. This

method would be similar to the analysis of atmosphere, in which several horizontal layers with different refractive index and loss in each layer. This technique can be used to include the inter-layer emission in the autocorrelation response of the system. This future work will allow us to monitor the wetness in the snow, which is important in flood and avalanche prediction as one of the main reasons of avalanche formation is due to the very fast melting rate of snowpacks in sloped mountain regions. On the other hand, it will also give us the ability to monitor the lossy sea ice thickness, which can be used to see if the ice is thin enough to navigate ships.

5.3.3 Dual-Polarized Wideband Autocorrelation Radiometry (WiBAR)

When multi-layer structures exist, such as a snowpack over a lake icepack, multiple paths exists, which may confound the interpretation of the autocorrelation function (ACF). Dual-polarized WiBAR measurements can be used to resolve the amplitudes. Due to its significantly higher reflection coefficients, H-pol often has observable delays regardless of incidence angle (nadir to at least 85 degrees), while V-pol often has no observable delays. However, near grazing, the V-pol reflection coefficients become sufficiently large for some of the interfaces in a snow over ice scene, while H-pol reflection coefficients remain sufficiently large for most interfaces. As a result, the two polarizations provide complimentary information about the scene, and the snow depth, which could be difficult to observe in the single polarization WiBAR, can be retrieved from dual polarization observations. On the other extreme, for example, this idea will allow the dual-pol WiBAR to be adapted into a product to put on automobiles to detect the presence of an ice patch and alert the driver well ahead of time since it works much better at higher incidence angles and can detect the ice much further away from the vehicle.

5.3.4 Imaging with Wideband Autocorrelation Radiometry

The objective is to develop and demonstrate the mapping/imaging of the thickness of a cryospheric slab with spatially varying thickness using a Wideband Autocorrelation Radiometer at a spatial resolution better than the footprint of that WiBAR instrument. The technology proposed in this project is designed to enable a future Cold Lands observing mission using WiBAR with adaptive RFI Mitigation for snowpack and freshwater ice sensing from airborne or space borne platforms. The instrument architecture, including hardware and software, particularly the software for disaggregation of the WiBAR images, will be designed to readily scale to an airborne and space borne, conically scanning instrument.

One possible approach is to use the Backus-Gilbert algorithm [3]. The Backus-Gilbert re-sampling scheme for traditional microwave radiometry is an appropriately weighted sum of brightness temperature observations in region local (i.e. within a footprint or so) of the desired location. Since one representation of the WiBAR data is as a spectrum of brightness temperatures, this algorithm will work for WiBAR data, although the weight for a particular desired location given a nearby observation will not be a single number, but a slowly varying function of frequency, due to the fact that wideband antenna pattern typically gets narrower as the frequency increases.

BIBLIOGRAPHY

BIBLIOGRAPHY

[1] Agilent Technologies. *Spectrum Analysis Basics*, August 2006. Application Note 150.

[2] J. J. Apinis and W. H. Peake. *Passive microwave mapping of ice thickness*. Ohio State Univ. ElectroScience Lab. Rep. 3892-2, August 1976.

[3] George Backus and Freeman Gilbert. Uniqueness in the inversion of inaccurate gross earth data. *Philosophical Transactions of the Royal Society of London. Series A, Mathematical and Physical Sciences*, 266(1173):123–192, 1970.

[4] J. Baker-Jarvis, E. J. Vanzura, and W. A. Kissick. Improved technique for determining complex permittivity with the transmission/reflection method. *IEEE Transactions on Microwave Theory and Techniques*, 38(8):1096–1103, Aug 1990.

[5] Tim P Barnett, Jennifer C Adam, and Dennis P Lettenmaier. Potential impacts of a warming climate on water availability in snow-dominated regions. *Nature*, 438(7066):303, 2005.

[6] M. Bertocco and A. Sona. On the measurement of power via a superheterodyne spectrum analyzer. *IEEE Transactions on Instrumentation and Measurement*, 55(5):1494–1501, Oct 2006.

[7] Philip R. Bevington and D. Keith Robinson. *Data Reduction and Error Analysis for the Physical Sciences*. McGraw-Hill, New York, second edition, 1992.

[8] A. T. Chang, J. L. Foster, D. K. Hall, A. Rango, and B. K. Hartline. Snow water equivalent estimation by microwave radiometry. *Cold Regions Science and Technology*, 5(3):259–267, 1982.

[9] R. D. De Roo, S. Misra, and C. S. Ruf. Sensitivity of the kurtosis statistic as a detector of pulsed sinusoidal RFI. *IEEE Transactions on Geoscience and Remote Sensing*, 45(7):1938–1946, July 2007.

[10] C. Derksen, A. Walker, E. LeDrew, and B. Goodison. Combining SMMR and SSM/I data for time series analysis of central North American snow water equivalent. *Journal of Hydrometeorology*, 4(2):304–316, 2003.

[11] M. C. Dobson, F. T. Ulaby, M. T. Hallikainen, and M. A. El-Rayes. Microwave Dielectric Behavior of Wet Soil-Part II: Dielectric Mixing Models. *IEEE Transactions on Geoscience and Remote Sensing*, GE-23(1):35–46, Jan 1985.

[12] M. Durand, E. J. Kim, and S. A. Margulis. Quantifying uncertainty in modeling snow microwave radiance for a mountain snowpack at the point-scale, including stratigraphic effects. *IEEE Transactions on Geoscience and Remote Sensing*, 46(6):1753–1767, June 2008.

[13] A. W. England. Thermal microwave emission from a scattering layer. *Journal of Geophysical Research*, 80(32):4484–4496, 1975.

[14] A. W. England. Thermal microwave emission from a halfspace containing scatterers . *Radio Sci.*, 9(4):447–454, Apr. 1974.

[15] A. W. England. Wideband autocorrelation radiometric sensing of microwave travel time in snowpacks and planetary ice layers. *IEEE Trans. Geosci. Remote Sens.*, 51:2316–2326, Apr. 2013.

[16] Anthony W. England and G. R. Johnson. Microwave brightness spectra of layered media. *Geophysics*, 42(3):514–521, April 1977.

[17] S. Evans. Dielectric properties of ice and snow–A review. *Journal of Glaciology*, 5(42):773–792, 1965.

[18] J. F. Galantowicz and A. W. England. Seasonal snowpack radiobrightness interpretation using a SVAT–linked emission model. *Journal of Geophysical Research: Atmospheres*, 102(D18):21933–21946, 1997.

[19] R.J. Galley, M. Trachtenberg, A. Langlois, D.G. Barber, and L. Shafai. Observations of geophysical and dielectric properties and ground penetrating radar signatures for discrimination of snow, sea ice and freshwater ice thickness. *Cold Regions Science and Technology*, 57(1):29 – 38, 2009.

[20] Gleick, P. H. and Pacific Institute for Studies in Development, Environment, and Security and Stockholm Environment Institute. *Water in Crisis: A Guide to the World's Fresh Water Resources*. Oxford University Press, 1993.

[21] B. E. Goodison and A. E. Walker. Use of snow cover derived from satellite passive microwave data as an indicator of climate change. *Annals of Glaciology*, 17:137–142, 1993.

[22] Tore Guneriussen, Kjell Arild Hogda, Harold Johnsen, and Inge Lauknes. InSAR for estimation of changes in snow water equivalent of dry snow. *IEEE Transactions on Geoscience and Remote Sensing*, 39(10):2101–2108, October 2001.

[23] Jianjun Guo, Leung Tsang, E. Josberger, and Jenq-Neng Hwang. Mapping the spatial distribution and time evolution of snow water equivalent with passive microwave measurements. In *IEEE International Geoscience and Remote Sensing Symposium*, volume 1, pages 454–456 vol.1, 2002.

[24] D. K. Hall, J. L. Foster, A. Rango, and A. T. C. Chang. *Passive microwave studies of frozen lakes*. NASA TM-79613, January 1978.

[25] M. Hallikainen, F. T. Ulaby, M. C. Dobson, and M. El-Rayes. Dielectric measurements of soils in the 3- to 37-GHz band between -50°C and 23°C. In *IEEE International Geoscience and Remote Sensing Symposium (IGARSS)*, pages 163–168, August 1984.

[26] M. T. Hallikainen and P. A. Jolma. Retrieval of the water equivalent of snow cover in Finland by satellite microwave radiometry. *IEEE Transactions on Geoscience and Remote Sensing*, GE-24(6):855–862, Nov 1986.

[27] M. T. Hallikainen and P. A. Jolma. Comparison of algorithms for retrieval of snow water equivalent from Nimbus-7 SMMR data in Finland. *IEEE Transactions on Geoscience and Remote Sensing*, 30(1):124–131, Jan 1992.

[28] M. T. Hallikainen, F. T. Ulaby, M. C. Dobson, M. A. El-Rayes, and L. K. Wu. Microwave dielectric behavior of wet soil-part 1: Empirical models and experimental observations. *IEEE Transactions on Geoscience and Remote Sensing*, GE-23(1):25–34, Jan 1985.

[29] R. F. Harrington. *The development of a stepped frequency microwave radiometer and its application to remote sensing of the Earth.* NASA TM-81847, June 1980.

[30] F. J. Harris. On the use of windows for harmonic analysis with the discrete Fourier transform. *Proceedings of the IEEE*, 66(1):51–83, Jan 1978.

[31] J.B. Hasted. *Aqueous dielectrics.* Studies in chemical physics. Chapman and Hall [Distributed in the U.S.A. by Halsted Press, a division of J. Wiley & Sons, New York], 1973.

[32] C. W. Helstrom. Computing the generalized Marcum Q-function. *IEEE Transactions on Information Theory*, 38(4):1422–1428, July 1992.

[33] T. J. Jackson, T. J. Schmugge, P. E. O'Neill, and M. B. Parlange. Soil water infiltration observation with microwave radiometers. *IEEE Transactions on Geoscience and Remote Sensing*, 36(5):1376–1383, Sep 1998.

[34] M. V. Jacob, J. Mazierska, K. Leong, and J. Krupka. Microwave properties of low-loss polymers at cryogenic temperatures. *IEEE Transactions on Microwave Theory and Techniques*, 50(2):474–480, Feb 2002.

[35] Mohan V. Jacob, Janina Mazierska, and Jerzy Krupka. Dielectric properties of yttrium vanadate crystals from 15 K to 295 K. *Journal of Electroceramics*, 15(3):237–241, Dec 2005.

[36] Michael D Janezic and Dylan F Williams. Permittivity characterization from transmission-line measurement. In *Microwave Symposium Digest, 1997., IEEE MTT-S International*, volume 3, pages 1343–1346. IEEE, 1997.

[37] J. T. Johnson, Hyunjun Kim, D. R. Wiggins, and Yonghun Cheon. Subsurface object sensing with a multifrequency microwave radiometer. *IEEE Transactions on Geoscience and Remote Sensing*, 40(12):2719–2726, Dec 2002.

[38] Steven M. Kay. *Fundamentals of Statistical Signal Processing: Estimation Theory*. Prentice-Hall, Inc., Upper Saddle River, NJ, USA, 1993.

[39] R. E. Kelly, A. T. Chang, Leung Tsang, and J. L. Foster. A prototype AMSR-E global snow area and snow depth algorithm. *IEEE Transactions on Geoscience and Remote Sensing*, 41(2):230–242, Feb 2003.

[40] M. Kendall and A. Stuart. *The advanced theory of statistics. Vol.2: Inference and relationship*. Griffin, London, 1979.

[41] L. Klein and C. Swift. An improved model for the dielectric constant of sea water at microwave frequencies. *IEEE Journal of Oceanic Engineering*, 2(1):104–111, January 1977.

[42] T. Koike and T. Suhama. Passive-microwave remote sensing of snow. *Ann. Glaciol*, 18:305–308, 1993.

[43] J. A. Lane and J. A. Saxton. Dielectric dispersion in pure polar liquids at very high radio frequencies. iii. the effect of electrolytes in solution. *Proceedings of the Royal Society of London. Series A, Mathematical and Physical Sciences*, 214(1119):531–545, 1952.

[44] J. Lemmetyinen, C. Derksen, J. Pulliainen, W. Strapp, P. Toose, A. Walker, S. Tauriainen, J. Pihlflyckt, J. P. Karna, and M. T. Hallikainen. A comparison of airborne microwave brightness temperatures and snowpack properties across the boreal forests of Finland and western Canada. *IEEE Transactions on Geoscience and Remote Sensing*, 47(3):965–978, March 2009.

[45] Shusun Li and Matthew Sturm. Patterns of wind-drifted snow on the Alaskan arctic slope, detected with ERS-1 interferometric SAR. *Journal of Glaciology*, 48(163):495–504, 2002.

[46] J. I. López-Moreno, S. Goyette, and M. Beniston. Impact of climate change on snowpack in the Pyrenees: Horizontal spatial variability and vertical gradients. *Journal of Hydrology*, 374(3):384 – 396, 2009.

[47] J. F. Manwell, C.N. Elkinton, A.L. Rogers, and J.G. McGowan. Review of design conditions applicable to offshore wind energy systems in the United States. *Renewable and Sustainable Energy Reviews*, 11(2):210 – 234, 2007.

[48] T. Markus, D. C. Powell, and J. R. Wang. Sensitivity of passive microwave snow depth retrievals to weather effects and snow evolution. *IEEE Transactions on Geoscience and Remote Sensing*, 44(1):68–77, Jan 2006.

[49] Hans-Peter Marshall, Gary Koh, and Richard R. Forster. Ground-based frequency modulated contiuous wave radar measurements in wet and dry snowpacks, Colorado, USA: An analysis and summary of the 2002-03 NASA CLPX data. *Hydrological Processes*, 18(18):3609–3622, December 2004.

[50] C. Mätzler, Institution of Engineering, and Technology. *Thermal Microwave Radiation: Applications for Remote Sensing*. IET electromagnetic waves series. Institution of Engineering and Technology, 2006.

[51] C Matzler and U Wegmuller. Dielectric properties of freshwater ice at microwave frequencies. *Journal of Physics D: Applied Physics*, 20(12):1623, 1987.

[52] R. McAulay and E. Hofstetter. Barankin bounds on parameter estimation. *IEEE Transactions on Information Theory*, 17(6):669–676, November 1971.

[53] P. C. D. Milly, J. Beancourt, M. Falkenmark, R. M. Hirsch, W. Kundzewiez, D. P. Lettenmaier, and R. J. Stouffer. Stationary is dead: Whither water management? *Science*, 319(5863):573–574, Feb. 2008.

[54] S. Mousavi, R. De Roo, K. Sarabandi, and A. W. England. Wideband autocorrelation radiometry for lake icepack thickness measurement with dry snow cover. *IEEE Geoscience and Remote Sensing Letters*, 16(10):1526–1530, Oct 2019.

[55] S. Mousavi, R. D. De Roo, K. Sarabandi, and A. W. England. Non-destructive dielectric constant measurement of low-loss dielectric slabs using wideband autocorrelation radiometry. In *2019 IEEE International Symposium on Antennas and Propagation and USNC-URSI Radio Science Meeting*, pages 157–158, July 2019.

[56] S. Mousavi, R. D. De Roo, K. Sarabandi, and A. W. England. Retrieval of snow or ice pack thickness variation within a footprint of correlation radiometers. *IEEE Geoscience and Remote Sensing Letters*, 2019.

[57] S. Mousavi, R. D. De Roo, K. Sarabandi, A. W. England, S. Y. E. Wong, and H. Nejati. Lake icepack and dry snowpack thickness measurement using wideband autocorrelation radiometry. *IEEE Transactions on Geoscience and Remote Sensing*, 56(3):1637–1651, March 2018.

[58] S. Mousavi, R. De Roo, K. Sarabandi, and A. England. Sampling requirements for wideband autocorrelation radiometric (WiBAR) remote sensing of dry snowpack and lake icepack. In *2017 IEEE International Geoscience and Remote Sensing Symposium (IGARSS)*, pages 1004–1007, July 2017.

[59] S. Mousavi, R. De Roo, K. Sarabandi, A. England, and H. Nejati. Dry snowpack and freshwater icepack remote sensing using wideband autocorrelation radiometry. In *2016 IEEE International Geoscience and Remote Sensing Symposium (IGARSS)*, pages 5288–5291, July 2016.

[60] S. Mousavi, R. De Roo, K. Sarabandi, A. England, and H. Nejati. Remote sensing using coherent multipath interference of wideband Planck radiation. In *2016 IEEE International Symposium on Antennas and Propagation (APSURSI)*, pages 2051–2052, June 2016.

[61] S. Mousavi, R. De Roo, K. Sarabandi, and A. W. England. Effect of a thin dry snow layer on the lake ice thickness measurement using wideband autocorrelation radiometry. In *IGARSS 2018 - 2018 IEEE International Geoscience and Remote Sensing Symposium*, pages 7109–7112, July 2018.

[62] National Academies of Sciences, Engineering, and Medicine. *Thriving on Our Changing Planet: A Decadal Strategy for Earth Observation from Space*. The National Academies Press, Washington, DC, 2018.

[63] H. Nejati. Passive remote sensing of lake ice and snow using wideband autocorrelation radiometer (WiBAR). 2014.

[64] R. Okorn, G. Brunnhofer, T. Platzer, A. Heilig, L. Schmid, C. Mitterer, J. Schweizer, and O. Eisen. Upward-looking L-band FMCW radar for snow cover monitoring. *Cold Regions Science and Technology*, 103:31–40, July 2014.

[65] Sheila M. Olmstead. Climate change adaptation and water resource management: A review of the literature. *Energy Economics*, 46:500–509, Nov 2014.

[66] Thomas H. Painter, Daniel F. Berisford, Joseph W. Boardman, Kathryn J. Bormann, Jeffrey S. Deems, Frank Gehrke, Andrew Hedrick, Michael Joyce, Ross Laidlaw, Danny Marks, Chris Mattmann, Bruce McGurk, Paul Ramirez, Megan Richardson, S. McKenzie Skiles, Felix C. Seidel, and Adam Winstral. The Airborne Snow Observatory: Fusion of scanning lidar, imaging spectrometer, and physically-based modeling for mapping snow water equivalent and snow albedo. *Remote Sensing of Environment*, 184:139 – 152, 2016.

[67] A. Papoulis. *Probability, Random Variables, and Stochastic Processes*. McGraw-Hill Series in Electrical Engineering. McGraw-Hill, 1984.

[68] N. R. Peplinski, F. T. Ulaby, and M. C. Dobson. Dielectric properties of soils in the 0.3-1.3 GHz range. *IEEE Transactions on Geoscience and Remote Sensing*, 33(3):803–807, May 1995.

[69] J.G. Proakis. *Digital Communications*. McGraw-Hill series in electrical and computer engineering : communications and signal processing. McGraw-Hill, 2001.

[70] J. T. Pulliainen, J. Grandell, and M. T. Hallikainen. HUT snow emission model and its applicability to snow water equivalent retrieval. *IEEE Transactions on Geoscience and Remote Sensing*, 37(3):1378–1390, May 1999.

[71] Jouni Pulliainen and Martti Hallikainen. Retrieval of regional snow water equivalent from space-borne passive microwave observations. *Remote Sensing of Environment*, 75(1):76 – 85, 2001.

[72] R. K. Raney. Synthetic aperture imaging radar and moving targets. *IEEE Transactions on Aerospace and Electronic Systems*, AES-7(3):499–505, May 1971.

[73] D. Rife and R. Boorstyn. Single tone parameter estimation from discrete-time observations. *IEEE Transactions on Information Theory*, 20(5):591–598, Sep. 1974.

[74] Kurt Roth, Rainer Schulin, Hannes Flühler, and Werner Attinger. Calibration of time domain reflectometry for water content measurement using a composite dielectric approach. *Water Resources Research*, 26(10):2267–2273.

[75] S. M. Rytov, Y. A. Kravtsov, and V. I. Tatarskii. *Principles of Statistical Radiophysics 2: Correlation theory of random processes*. Springer, 1988.

[76] S. M. Rytov, Y. A. Kravtsov, and V. I. Tatarskii. *Principles of Statistical Radiophysics 3: Elements of Random Fields*. Springer, 2011.

[77] Jürg Schweizer, Kalle Kronholm, J. Bruce Jamieson, and Karl W. Birkeland. Review of spatial variability of snowpack properties and its importance for avalanche formation. *Cold Regions Science and Technology*, 51(2):253 – 272, 2008. International Snow Science Workshop (ISSW) 2006.

[78] L. P. Seidman. Performance limitations and error calculations for parameter estimation. *Proceedings of the IEEE*, 58(5):644–652, May 1970.

[79] M. C. Serreze, J. E. Walsh, F. S. Chapin, T. Osterkamp, M. Dyurgerov, V. Romanovsky, W. C. Oechel, J. Morison, T. Zhang, and R. G. Barry. Observational Evidence of Recent Change in the Northern High-Latitude Environment. *Climatic Change*, 46(1):159–207, Jul 2000.

[80] H. C. So, Y. T. Chan, Q. Ma, and P. C. Ching. Comparison of various periodograms for sinusoid detection and frequency estimation. *IEEE Transactions on Aerospace and Electronic Systems*, 35(3):945–952, July 1999.

[81] B. B. Stankov, D. W. Cline, B. L. Weber, A. J. Gasiewski, and G. A. Wick. High-resolution airborne polarimetric microwave imaging of snow cover during the NASA Cold Land Processes Experiment. *IEEE Transactions on Geoscience and Remote Sensing*, 46(11):3672–3693, Nov 2008.

[82] A. Stogryn. Equations for calculating the dielectric constant of saline water (correspondence). *IEEE Transactions on Microwave Theory and Techniques*, 19(8):733–736, Aug 1971.

[83] P. Stoica, R. L. Moses, B. Friedlander, and T. Soderstrom. Maximum likelihood estimation of the parameters of multiple sinusoids from noisy measurements. *IEEE Transactions on Acoustics, Speech, and Signal Processing*, 37(3):378–392, March 1989.

[84] A. Stuart and K. Ord. *Kendall's Advanced Theory of Statistics, Distribution Theory*. Kendall's Advanced Theory of Statistics. Wiley, 2010.

[85] C. T. Swift, D. C. Dehority, A. B. Tanner, and R. E. Mcintosh. Passive microwave spectral emission from saline ice at C-band during the growth phase. *IEEE Transactions on Geoscience and Remote Sensing*, GE-24(6):840–848, Nov 1986.

[86] C. T. Swift, W. L. Jones, R. F. Harrington, J. C. Fedors, R. H. Couch, and B. L. Jackson. Microwave radar and radiometric remote sensing measurements of lake ice. *Geophysical Research Letters*, 7(4):243–246, 1980.

[87] L. Tsang, J. A. Kong, and R. T. Shin. *Theory of Microwave Remote Sensing*. John Wiley and Sons, New York, 1985.

[88] L. Tsang, J.A. Kong, and K.H. Ding. *Scattering of electromagnetic waves: Theories and applications*. Wiley series in remote sensing. J. Wiley, 2000.

[89] F. T. Ulaby, D.G. Long, W.J. Blackwell, C. Elachi, and K. Sarabandi. *Microwave Radar and Radiometric Remote Sensing*. University of Michigan Press, 2014.

[90] F. T. Ulaby, R. K. Moore, and A. K. Fung. *Microwave Remote Sensing: Active and Passive*, volume I. Artech House, Norwood, MA, 1981.

[91] F. T. Ulaby, R. K. Moore, and A. K. Fung. *Microwave Remote Sensing: Active and Passive*, volume III. Artech House, Norwood, MA, 1986.

[92] R. B. Waitt, Ted C. Pierson, Norman MacLeod, Richard Janda, Benjamin Voight, and Roland Holcomb. Eruption-triggered avalanche, flood, and lahar at Mount St. Helens–effects of winter snowpack. *Science*, 221 4618:1394–7, 1983.

[93] J. R. Wang and B. J. Choudhury. Remote sensing of soil moisture content, over bare field at 1.4 GHz frequency. *Journal of Geophysical Research: Oceans*, 86(C6):5277–5282, 1981.

[94] L. L. Wilson, Leung Tsang, Jenq-Neng Hwang, and Chi-Te Chen. Mapping snow water equivalent by combining a spatially distributed snow hydrology model with passive microwave remote-sensing data. *IEEE Transactions on Geoscience and Remote Sensing*, 37(2):690–704, Mar 1999.

[95] J. Ziv and M. Zakai. Some lower bounds on signal parameter estimation. *IEEE Transactions on Information Theory*, 15(3):386–391, May 1969.